NASA CR 179522

SwRI-7576/45

NASA

CONSTITUTIVE MODELING FOR ISOTROPIC MATERIALS (HOST)

(Third Annual Status Report)

By

K. S. Chan
U. S. Lindholm
S. R. Bodner
J. T. Hill
R. M. Weber
T. G. Meyer

Southwest Research Institute
P. O. Drawer 28510
San Antonio, TX 78284

Prepared For

NATIONAL AERONAUTICS AND SPACE ADMINISTRATION
NASA-Lewis Research Center
Contract NAS3-23925

SOUTHWEST RESEARCH INSTITUTE
SAN ANTONIO HOUSTON

1. Report No.	2. Government Accession No.	3. Recipient's Catalog No.
NASA CR 179522		

4. Title and Subtitle	5. Report Date
Constitutive Modeling for Isotropic Materials (HOST)	August 1986
	6. Performing Organization Code

7. Author(s)	8. Performing Organization Report No.
K. S. Chan, U. S. Lindholm, S. R. Bodner, J. T. Hill, R. M. Weber, and T. G. Meyer	SwRI Project No. 06-7576
	10. Work Unit No.

9. Performing Organization Name and Address	11. Contract or Grant No.
Southwest Research Institute Department of Materials Sciences P. O. Drawer 28510 San Antonio, TX 78284	NAS3-23925
	13. Type of Report and Period Covered
12. Sponsoring Agency Name and Address	Third Annual Status Report
National Aeronautics & Space Administration Washington, DC 20546	14. Sponsoring Agency Code
	RTOP 533-04-1A

15. Supplementary Notes

Project Manager, A. Kaufman
NASA Lewis Research Center (MS 49-7)
21000 Brookpark Road
Cleveland, OH 44135

16. Abstract

This report presents the results of the third year of work on a program which is part of the NASA HOST program. The goals of this program are: (1) the development of unified constitutive models for rate dependent isotropic materials, and (2) the demonstration of the use of unified models in structural analyses of hot section components of gas turbine engines. The unified models selected for development and evaluation are those of Bodner-Partom and of Walker.

In the past year, a test procedure was developed for assisting the generation of a data base for the Bodner-Partom model using a relatively small number of specimens. This test procedure involved performing a single tensile test at a temperature of interest that involves a succession of strain-rate changes. The results for B1900+Hf in the temperature range of 23 - 1093°C indicate that material constants related to hardening and thermal recovery can be obtained on the basis of such a procedure. Strain aging, thermal recovery, and unexpected material variations, however, precluded an accurate determination of the strain-rate sensitivity parameter in this exercise. The effects of casting grain size on the constitutive behavior of B1900+Hf was studied and no particular grain size effect was observed. It was, therefore, concluded that the variation in material properties observed in B1900+Hf was not due to grain size differences. A systematic procedure was also developed for determining the material constants in the Bodner-Partom model. Both the new test procedure and the method for determining material constants were applied to the alternate material, Mar-M247. Test data including tensile, creep, cyclic and nonproportional biaxial (tension/torsion) loading were collected. Good correlations were obtained between the Bodner-Partom model and experiments indicating both representational and predictive capability.

A literature survey was conducted to assess the effects of thermal history on the constitutive behavior of metals. Thermal history effects are expected to be present at temperature regimes where strain aging and change of microstructure are important. Possible modifications to the Bodner-Partom model to account for these effects are outlined.

The use of a unified constitutive model for hot section component analyses was demonstrated by applying the Walker model and the MARC finite-element code to a B1900+Hf airfoil problem with a complex, realistic flight cycle. The efficiency of several numerical integrating schemes was also evaluated. Comparison of currently available numerical results for both the Walker and the Bodner-Partom models obtained at NASA Lewis Research Center indicates that there is no inherent difference in the numerical efficiency between those models.

17. Key Words (Suggested by Author(s))	18. Distribution Statement
Hot Section Technology, Nonlinear Structural Analysis, Unified Constitutive Model	Unclassified Unlimited

19. Security Classif. (of this report)	20. Security Classif. (of this page)	21. No. of pages	22. Price*
Unclassified	Unclassified	118	

*For sale by the National Technical Information Service, Springfield, Virginia 22161

PREFACE

The Third Annual Status Report covers the effort of the third year of the NASA HOST program entitled "Constitutive Modeling for Isotropic Materials" conducted under Contract NAS3-23925. The NASA program manager for this project is Mr. Albert Kaufman. The program manager at Southwest Research Institute is Dr. Ulric Lindholm. Contributors to this report are Dr. Kwai Chan and Mr. Andrew Nagy of SwRI, Messrs. J. T. Hill, R. M. Weber and T. G. Meyer of Pratt and Whitney Aircraft, and Prof. Sol R. Bodner as a consultant.

TABLE OF CONTENTS

TABLE OF CONTENTS (CONTINUED)

LIST OF FIGURES

LIST OF FIGURES (CONTINUED)

LIST OF FIGURES (CONTINUED)

LIST OF FIGURES (CONTINUED)

LIST OF FIGURES (CONTINUED)

LIST OF TABLES

1.0 INTRODUCTION

The objective of the present program is to develop a unified constitutive model for finite-element structural analysis of turbine engine hot section components. This effort constitutes a different approach for non-linear finite-element computer codes which have heretofore been based on classical inelastic methods. The unified constitutive theory to be developed will avoid the simplifying assumptions of classical theory and should more accurately represent the behavior of superalloy materials under cyclic loading conditions and high temperature environments. This class of constitutive theory is characterized by the use of kinetic equations and internal variables with appropriate evolution equations for treating all aspects of inelastic deformation including plasticity, creep and stress relaxation. Model development is directed toward isotropic, cast nickel-base alloys used for air-cooled turbine blades and vanes. Recent studies have shown that this approach is particularly suited for determining the cyclic behavior of superalloy type blade and vane materials and is entirely compatible with three dimensional inelastic finite-element formulations. More efficient and accurate inelastic analysis of hot section components--turbine blades, turbine vanes, combustor liners and seals--fabricated from "age hardenable" isotropic superalloy materials will be realized as the result of these developments.

The program is being conducted in two phases: a basic program (Tasks A through I) and an optional follow-on program (Tasks J through M). In the basic program which was completed last year [1,2], two unified constitutive models, i.e. the Bodner-Partom [3,4] and the Walker [5], models were further developed for the prediction of the structural response of isotropic materials for temperatures and strain range characteristics of cooled turbine vanes in

advanced gas turbine engines (Task A). A data base of uniaxial and multiaxial material response characteristics required for the constitutive model development was obtained for the base material, B1900+Hf (Tasks C and E). The constitutive models were then incorporated into the MARC finite-element computer code (Task D). The capability of the analytical method to predict the structural response was evaluated for multiaxial stress states (Task E) and nonisothermal conditions by conducting thermomechanical loading and benchmark notch verification experiments and analysis (Task F). As a final evaluation of the analytical model, a structural analysis was performed for a hot section component fabricated from the base material for simulated engine operating conditions (Task G).

At the present time, the first year of the optional program (third year of the total program) has been completed. In the optional program, material property test procedures are to be further developed to minimize the required testing, and the possibility of estimating material model constants from conventional property data is to be examined (Task J). Further development of the model will be undertaken to consider thermal history effects and to correct any deficiencies indicated in the model or the computational algorithms in the code (Task K). In addition, the constitutive model development will be verified for an alternate material (Task L).

The work under this program is being conducted as a joint effort between Pratt & Whitney Aircraft (PWA) and Southwest Research Institute (SwRI) with technical assistance from Prof. Sol R. Bodner and Dr. Kevin Walker in the area of constitutive model development. The work and data base generated is

being coordinated closely with another NASA funded HOST program at PWA (NAS3-23288) to develop advanced life prediction techniques for isotropic superalloy vane and blade materials.

This report documents the results and progress of the optional program. In addition, this report also presents the results of an inelastic analysis of a turbine blade under simulated engine operating conditions. The inelastic blade analysis was performed by Pratt & Whitney Aircraft as part of Task G in the base program.

2.0 DEVELOPMENT OF MATERIAL TEST PROCEDURES (TASK J)

2.1 Background

In the previous tasks of the basic program, extensive isothermal monotonic tensile, creep, and cyclic tests of the base material B1900+Hf were performed to develop a data base for evaluating two unified constitutive models. Testing of each cyclic strain controlled specimen involved only one strain ratio and temperature with the strain range and strain rate considered to be variables. Supplemental isothermal constant strain dwell tests were conducted to probe for the equilibrium stress and establish the material constants defining the evolution of this quantity. Nonproportional tension-torsion tests at constant temperature, and constant strain biaxial dwell tests were performed to define the material constants describing the multiaxial response of the material.

As part of Task J of the optional program, material property test procedures were further developed to minimize the amount of testing required, and to improve the procedures for determining the material constants of the Bodner-Partom model from conventional property data. Since the requirement for material testing is directly related to the method for determining model constants, a brief review of the procedures which were developed in the base program for obtaining the Bodner-Partom model constants will be given in the next section. In addition, calculations have been performed to examine the assumptions inherent in the procedure for the determination of the model constants. A consequence of this exercise is a small modification of the analytical basis of the procedure for determining the Bodner-Partom model

constants. The following review therefore also serves to update the method for determination of the material constants.

2.1.1 Review of the Method for Estimating Model Constants

Excluding the elastic constants, the Bodner-Partom model, summarized in Table 2.1, indicates a total of 13 material constants. In most all cases, including nonproportional loading paths, ten model constants are needed, one of which can be generally set so that nine constants are required from test data. Most of the constants, tabulated in Table 2.2, can be evaluated from monotonic tensile data. Creep data would also be required if slow strain rate tensile data are not available.

The procedure developed in the base program for determining the Bodner-Partom model constants relies primarily on the tensile data with occasional use of the creep data. However, the parameter which describes the nonproportional hardening effect, α_1, cannot be determined from uniaxial tensile data and, at present, must be evaluated from biaxial test data obtained under nonproportional loading.

The method for evaluating the Bodner-Partom model constants based on tensile and creep data is shown in Fig. 2.1. The first step [Step (1)] of the procedures is to develop a set of work hardening rate data from the experimental stress-strain results. Using the monotonic tensile stress-strain data and the elastic modulus as inputs, the plastic strain component is calculated by subtracting the elastic strain component from the total strain. The stress is then expressed as a polynominal function of the plastic strain.

$$\sigma = a_o + a_1\varepsilon^p + a_2(\varepsilon^p)^2 + \ldots\ldots + a_m(\varepsilon^p)^m \qquad (2.1)$$

TABLE 2.1

A SUMMARY OF BODNER-PARTOM MODEL

1. Flow Law:

$$\dot{\varepsilon}_{ij} = \dot{\varepsilon}_{ij}^{e} + \dot{\varepsilon}_{ij}^{p}$$

$$\dot{\varepsilon}_{ij}^{p} = \lambda S_{ij} \; ; \; \dot{\varepsilon}_{kk}^{p} = 0$$

with $S_{ij} = \sigma_{ij} - \frac{1}{3}\delta_{ij}\sigma_{kk}$

2. Kinetic Equation:

$$D_2^{p} = D_o^{2} \exp\left\{-\left[\frac{Z^2}{3J_2}\right]^{n}\right\}$$

with $Z = Z^{I} + Z^{D}$

$$D_2^{p} = \frac{1}{2}\dot{\varepsilon}_{ij}^{p}\dot{\varepsilon}_{ij}^{p}$$

$$J_2 = \frac{1}{2}S_{ij}S_{ij}$$

$$\lambda^2 = D_2^{p}/J_2$$

3. Evolution Equations of Internal Variables:

a. Isotropic Hardening

$$\dot{Z}^{I} = m_1\left[Z_1 + \alpha Z_3 - Z^{I}\right]\dot{W}_p - A_1 Z_1\left[\frac{Z^{I} - Z_2}{Z_1}\right]^{r_1}$$

where $\dot{\alpha} = m_2(\alpha_1 \sin\theta - \alpha)\dot{W}_p$

$$\theta = \cos^{-1}(V_{ij}\bar{V}_{ij}) \quad \text{or} \quad \theta = \cos^{-1}(u_{ij}\,\bar{u}_{ij})$$

$$V_{ij} = \beta_{ij}/(\beta_{kl}\beta_{kl})^{1/2}, \; \bar{V}_{ij} = \dot{\beta}_{ij}/(\dot{\beta}_{kl}\dot{\beta}_{kl})^{1/2}$$

$$u_{ij} = \sigma_{ij}/(\sigma_{kl}\sigma_{kl})^{1/2}, \; \bar{u}_{ij} = \dot{\sigma}_{ij}/(\dot{\sigma}_{kl}\dot{\sigma}_{kl})^{1/2}$$

with $Z^{I}(o) = Z_o$; $\dot{W}_p = \sigma_{ij}\dot{\varepsilon}_{ij}^{p}$; $\dot{W}_p(o) = 0$; $\alpha(0) = 0$

b. Directional Hardening

$$\dot{\beta}_{ij} = m_2(Z_3 u_{ij} - \beta_{ij})\dot{W}_p - A_2 Z_1\left[\frac{(\beta_{kl}\beta_{kl})^{1/2}}{Z_1}\right]^{r_2} V_{ij}$$

with $Z^{D} = \beta_{ij}u_{ij}$; $Z^{D}(o) = 0$, $\beta_{ij}(o) = 0$

Material Constants: D_o, Z_o, Z_1, Z_2, Z_3, m_1, m_2, α_1
A_1, A_2, r_1, r_2, n, and elastic constants

In most cases can set: $r_1 = r_2$, $A_1 = A_2$, $Z_o = Z_2$

TABLE 2.2

MATERIAL CONSTANTS IN BODNER-PARTOM CONSTITUTIVE MODEL

Constants	Descriptions
D_o	Limiting shear strain rate, sec^{-1}
Z_o	Initial value of the isotropic hardening variable, MPa
Z_1	Limiting (maximum) value of Z^I, MPa
Z_2	Fully recovered (minimum) value of Z^I, MPa
Z_3	Limiting (maximum) value of Z^D, MPa
m_1	Hardening rate coefficient of Z^I, MPa^{-1}
m_2	Hardening rate coefficient of Z^D, MPa^{-1}
n	Kinetic parameter
A_1	Recovery coefficient for Z^I, sec^{-1}
A_2	Recovery coefficient for Z^D, sec^{-1}
r_1	Recovery exponent for Z^I
r_2	Recovery exponent for Z^D
α_1	Limiting coefficient for non-proportional hardening effect

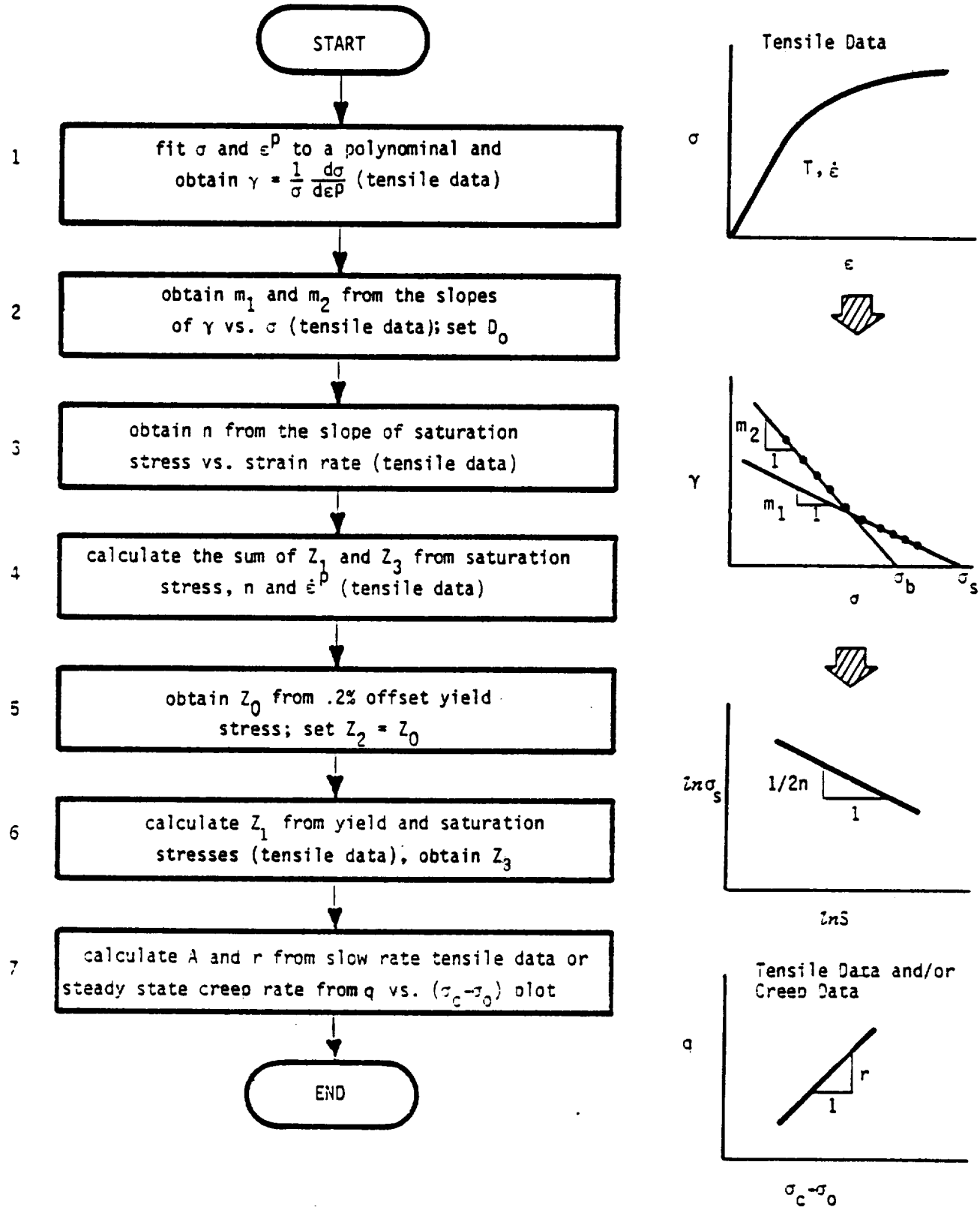

FIGURE 2.1 A FLOW CHART SHOWING A SYSTEMATIC PROCEDURE FOR EVALUATING THE MATERIAL CONSTANTS IN THE BODNER-PARTOM THEORY.

The coefficients a_o, a_1, a_2, ... a_m are computed using the least-square method. The work hardening rate, $\gamma = d\sigma/dW_p = (1/\sigma)(d\sigma/d\epsilon^p)$, can then be calculated as:

$$\gamma = \frac{1}{\sigma} = a_1 + 2a_2\epsilon^p + \ldots + ma_m(\epsilon^p)^{m-1} \tag{2.2}$$

where σ is obtained from Equation 2.1. The number of terms required in Equation 2.1 can be obtained by some experience.

Step (2) is to evaluate the constants m_1 and m_2 from the plot of γ versus σ (Figure 2.1). The Bodner-Partom model can be written for the uniaxial stress case as:

$$\sigma = L_1 \, Z \, (W_p) \tag{2.3}$$

with

$$L_1 = [2 \ (2D_o/\sqrt{3} \ \dot{\epsilon}^p)]^{-1/2n}$$

$$Z = Z^I + Z^D$$

where Z^I and Z^D are the isotropic and the directional hardening variables.

In the absence of thermal recovery and on the observation that directional hardening saturates much more rapidly than isotropic hardening for most materials, i.e., $m_2 > m_1$, the following approximations to Equation (2.3) can be made in the region of small plastic strains.

$$Z^I \approx Z_o$$

$$Z^D = (\sigma/L_1) - Z^I \approx (\sigma/L_1) - Z_o$$

where Z_o is defined in Table 2.2. In the previous analysis [2], Z^I was assumed to take the form: $Z^I \approx \sigma/L_1 - Z_3$, which was found to be overly restrictive. These approximations are then substituted in the general expression for $\gamma = d\sigma/dW_p$ obtained from Equation (2.3) and the evolution equations for Z^I and Z^D, namely

$$\dot{Z}_I = m_1 (Z_1 - Z^I) \dot{W}_p,$$

and

$$\dot{Z}_D = m_2 (Z_3 - Z^D) \dot{W}_p,$$

leading to

$$\gamma = L_1 \left[m_1 (Z_1 - Z^I) + m_2 (Z_3 - Z^D) \right] \tag{2.4}$$

With the above approximations, the expression for γ becomes

$$\gamma = L_1 [m_1 (Z_1 - Z_o) + m_2 (Z_o + Z_3)] - m_2 \sigma \tag{2.5}$$

The reference constitutive equations therefore indicate that a plot of γ against σ should be linear with slope m_2 in the range of small plastic strains.

At the larger strains, Z^D fully saturates to the limiting value Z_3 so that setting $Z^D = Z_3$ in Equations 2.3 and 2.4 gives

$$\gamma = L_1 m_1 (Z_1 + Z_3) - m_1 \sigma \tag{2.6}$$

which is a linear relation with slope m_1. These relations indicate that the γ-σ function corresponding to the model should be essentially linear at both the low and high plastic strain regions. In the high stress region, the intercept at the σ axis for $\gamma = 0$ is the saturation stress, σ_s, which is given by:

$$\sigma_s = L_1 (Z_1 + Z_3) \tag{2.7}$$

Step (3) is to evaluate the constants n and D_o in the kinetic equation. D_o corresponds to a limiting inelastic strain rate in shear and is usually taken to be $1x10^4$ sec^{-1} unless high strain rates are being considered. The constant n is evaluated from the stress dependence on strain rate at a constant value of Z. Equations 2.3 and 2.4 are rearranged to give the following expressions:

$$ln\sigma = -\frac{1}{2n} lnS + lnZ \tag{2.8}$$

and

$$\frac{1}{n} = -\frac{2d(ln\sigma)}{d(lnS)}; \; Z = \text{constant}; \; W_p = \text{constant} \tag{2.9}$$

where

$$S = 2ln \; (2D_o/\sqrt{3}\,\dot{\epsilon}^p) = L_1^{-2n} \tag{2.10}$$

Thus, n can be evaluated either from the slope of a plot of $ln\sigma$ versus lnS at a constant value of Z (W_p) [Equation (2.9)]. When static thermal recovery is not important, the stress values for evaluating the parameter n could be: (1) the saturation stress σ_s at different strain rates where σ_s corresponds to the limiting value of Z or $(Z_1 + Z_3)$ obtainable by extrapolating the γ-σ curve to the stress at which γ is equal to zero (Figure 2.1); (2) the peak stress of saturated cyclic hysteresis loops at different strain rates and at a constant value of large strain amplitude for which both Z^I and Z^D saturate; (3) the flow stress at different strain rates and at constant values of plastic work.

It is important to note that stress values under steady state conditions during creep or tensile straining do not always correspond to the same value of Z due to the recovery effect. Consequently, stress values under steady state conditions involving thermal recovery should not be used in conjunction with Equations 2.8 and 2.9 for evaluating n. The n value should be obtained at a temperature and strain rate at which static thermal recovery

is insignificant and the corresponding constants Z_1 and Z_3 can then be computed (see Step 4). Since both Z_1 and Z_3 are generally considered to be temperature-independent, the n value at a higher temperature can be obtained by fitting a single stress-strain curve at a sufficiently high strain rate (i.e. one not influenced by recovery effects), e.g. 10^{-3} sec^{-1}, or by using σ_s if known for that stress-strain curve.

Step (4) is to calculate the sum of Z_1 and Z_3. Using the saturation stress obtained in Step (2) and the L_1 value obtained in Step (3), the sum of Z_1 and Z_3 is calculated using Equations (2.7).

Step (5) is to evaluate Z_o from the yield stress at a small plastic strain offset, σ_o, by using the relation:

$$\sigma_o = L_1 Z_o(T) \tag{2.11}$$

where σ_o is taken initially to be the 0.2% offset yield stress. It has also been found in some that cases that using the proportional limit for σ_o gives a more accurate value for Z_o. In any event, it is often necessary to refine Z_o by fitting the model calculation to the tensile stress-strain curve after Z_1 and Z_3 are obtained. The fully recovered value of Z^I is Z_2 and it can generally be set equal to Z_o.

Step (6) is to evaluate particular values of Z_1 and Z_3, the limiting values of the isotropic, and directional hardening variables. From Equation 4.6 and Figure 2.2, it can be shown that σ_b is given by:

$$\sigma_b = \frac{L_1[m_1(Z_1 - Z_o) + m_2(Z_o + Z_3)]}{m_1} \tag{2.12}$$

With Eq. 2.7, Eq. 2.12 can be rearranged to give

$$Z_1 = Z_o + \frac{m_2(\sigma_s - \sigma_b)}{L_1(m_2 - m_1)} \tag{2.13}$$

and $$Z_3 = \frac{\sigma_s}{L_1} - Z_1 \tag{2.14}$$

from which Z_1 and Z_3 can be obtained.

The effect of static thermal recovery on the work hardening rate can be considered in a similar manner. Assuming $A_1 = A_2 = A$ and $r_1 = r_2 = r$, the expression for γ including the recovery term can be shown to have the form [6]

$$\gamma = L_1[m_1(Z_1-Z_o) + m_2(Z_o+Z_3)] - m_2\sigma - \frac{A(L_1Z_1)^{1-r}}{\sigma\dot{\epsilon}^p}[\sigma-\sigma_o]^r \tag{2.15}$$

Equation 2.15 is reduced to Equation 2.6 when A is zero; this occurs when static thermal recovery is unimportant.

The final step (Step 7) is to evaluate the recovery constants. For B1900+Hf, the above assumption on A and r is taken for the following reasons: (1) there is a need to reduce the number of constants and to simplify the procedures for evaluating these constants, (2) the γ-σ curves for B1900+Hf suggest that they need not be different and might be difficult to distinguish if they were, and (3) no physical mechanisms suggest that they should be different. The recovery constants can be evaluated from either the steady state stress (σ_c) and associated strain rate ($\dot{\epsilon}_c$) of a slow rate tensile test or the steady state creep rate ($\dot{\epsilon}_c$) and corresponding stress (σ_c) of a creep test. In both cases, the stress and associated plastic strain rate do not change with time or deformation. Under these conditions, the work hardening parameter, γ, is zero and Equation 2.15 can be rewritten as:

$$q - A(L_1Z_1)^{1-r}(\sigma_c - \sigma_o)^r = 0 \tag{2.16}$$

where $$q = \{L_1[m_1(Z_1-Z_o) + m_2(Z_o+Z_3)] - m_2\sigma_c\}\sigma_c\dot{\varepsilon}^p_c \quad (2.17)$$

The recovery exponent r can be obtained from Equation (2.16) as:

$$r = \frac{d \log q}{d \log (\sigma_c-\sigma_o)} \quad (2.18)$$

so that r is the slope of q vs $\sigma_c-\sigma_o$ in a log-log plot. Once r is obtained, the recovery constant A can be calculated using known values of q and Equation (2.15), which gives

$$A = \frac{q}{(L_1Z_1)^{1-r}\,(\sigma_c-\sigma_o)^r} \quad (2.19)$$

2.1.2 Hardening Characteristics and the Shape of the γ-σ Curves

The procedure described in the preceding section relies upon linear portions of the γ-σ curves being obtained from uniaxial, monotonic stress-strain tests to delineate isotropic and directional hardening. It has been demonstrated in the base program that the γ-σ curves for B1900+Hf show linear regions at both the low and high plastic strain regimes at temperatures where thermal recovery is insignificant. To examine whether this bilinear characteristic exists in the γ-σ plot for other nickel-base alloys, the hardening behavior of Hastelloy-X has been examined using uniaxial stress-strain curves previously supplied by Pratt & Whitney Aircraft.

Figure 2.2 shows the γ-σ plot at 649°C for Hastelloy-X. The Bodner-Partom model constants which can be determined from Figure 2.2 are m_1, m_2, Z_3, and Z_1 where Z_3 and Z_1 depend on an assumed value for n(=1, based on a previous exercise). The values of these constants for 649°C are summarized in Table 2.3 and compared with those values obtained previously by a trial and error procedure. Table 2.3 indicates that both set of values are similar.

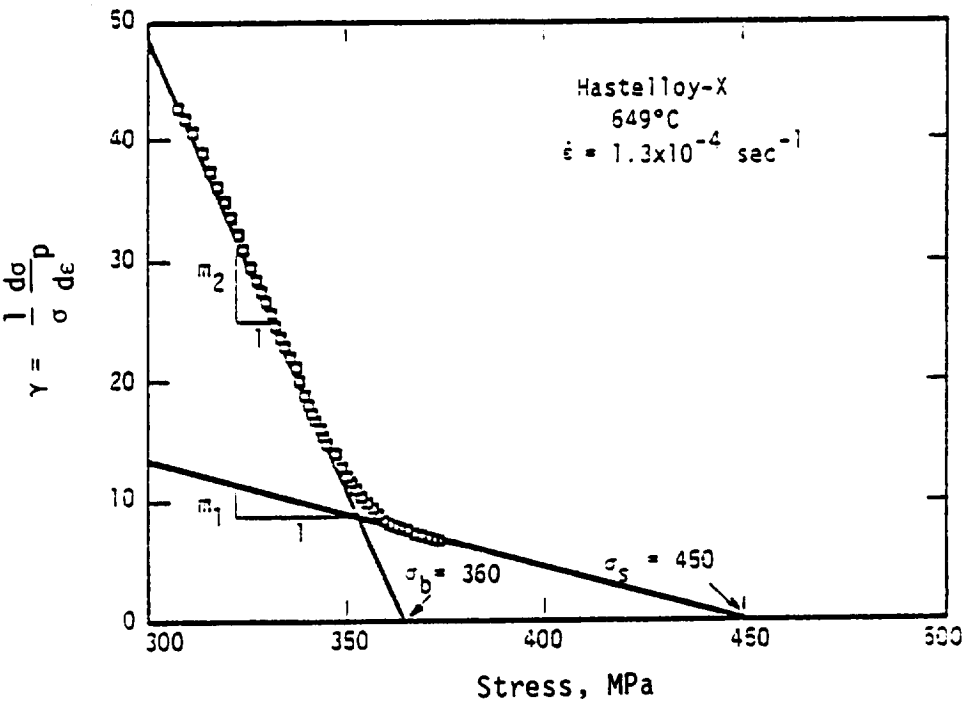

FIGURE 2.2 THE γ-σ PLOT FOR HASTELLOY-X AT 649°C.

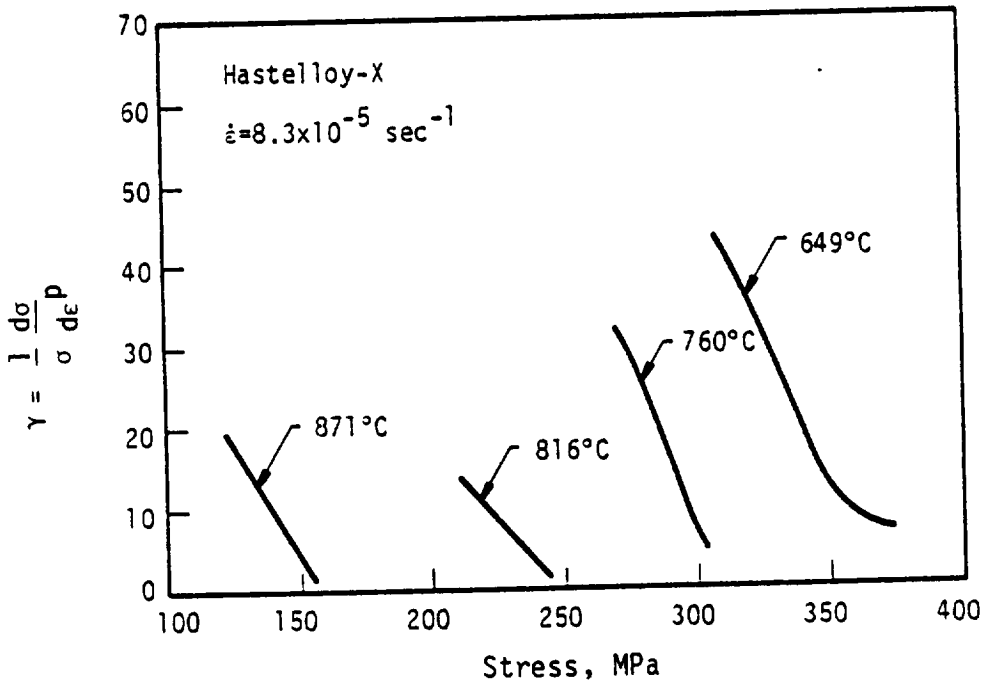

FIGURE 2.3 THE γ-σ PLOTS FOR HASTELLOY-X AT FOUR TEMPERATURES.

TABLE 2.3

COMPARISON OF BODNER-PARTOM MODEL CONSTANTS OBTAINED FOR HASTELLOY-X AT 649°C USING THE TRIAL AND ERROR AND THE γ-PLOT METHODS

	Trial and Error Method	γ Plot Approach
m_1	.1 MPa^{-1}	.09 MPa^{-1}
m_2	2.40 MPa^{-1}	.79 MPa^{-1}
Z_1	2000 MPa	2100 MPa
Z_3	500 MPa	600 MPa
n	1	1

The systematic approach based on the γ-σ plot is, however, more straightforward and reliable than the trial and error approach. Comparison of the γ-σ plots of Hastelloy-X at 648, 760, 816 and 871°C is shown in Figure 2.3. Note that the bilinear characteristic is lost with temperatures above 760°C which is probably due to thermal recovery effects.

The ability to distinguish the various linear segments of the hardening curve is crucial to the delineation of isotropic and directional hardening components from a uniaxial γ-σ diagram. The effects of the relative values of m_1 and m_2 on the shape of the γ-σ curve have been studied by performing γ-σ calculations using the Bodner-Partom model and the material constants for B1900+Hf at 871°C. Figure 2.4 shows the γ-σ curves for various m_2 values with $m_1 = 1.52$, while Figure 2.5 shows the γ-σ curves for various m_1 values with $m_2 = 1.52$. The results in Figures 2.4 and 2.5 reveal that in the absence of thermal recovery: (1) the shape of the γ-σ curve depends on the relative value of m_1 and m_2, and (2) a bilinear γ-σ curve is obtained when m_1 and m_2 are nonzero and have sufficiently different values. This information is useful for interpreting the experimental γ-σ plots.

The effects of the relative values of Z_o and Z_1 on the shape of the γ-σ curve have also been studied using the Bodner-Partom model. Cyclic hardening is obtained when the ratio of Z_o/Z_1 is less than unity (i.e., $Z_o < Z_1$), while cyclic softening results when $Z_o > Z_1$. Isotropic hardening is absent when $Z_o = Z_1$. The corresponding monotonic stress-strain curves calculated using the Bodner-Partom model are shown in Figure 2.6. Note that hardening is observed when $Z_o < Z_1$, and softening is observed when $Z_o > Z_1$. At large plastic strain, Z approaches Z_1 for both the hardening and softening materials, and all the stress-strain curves approach the limiting (saturation)

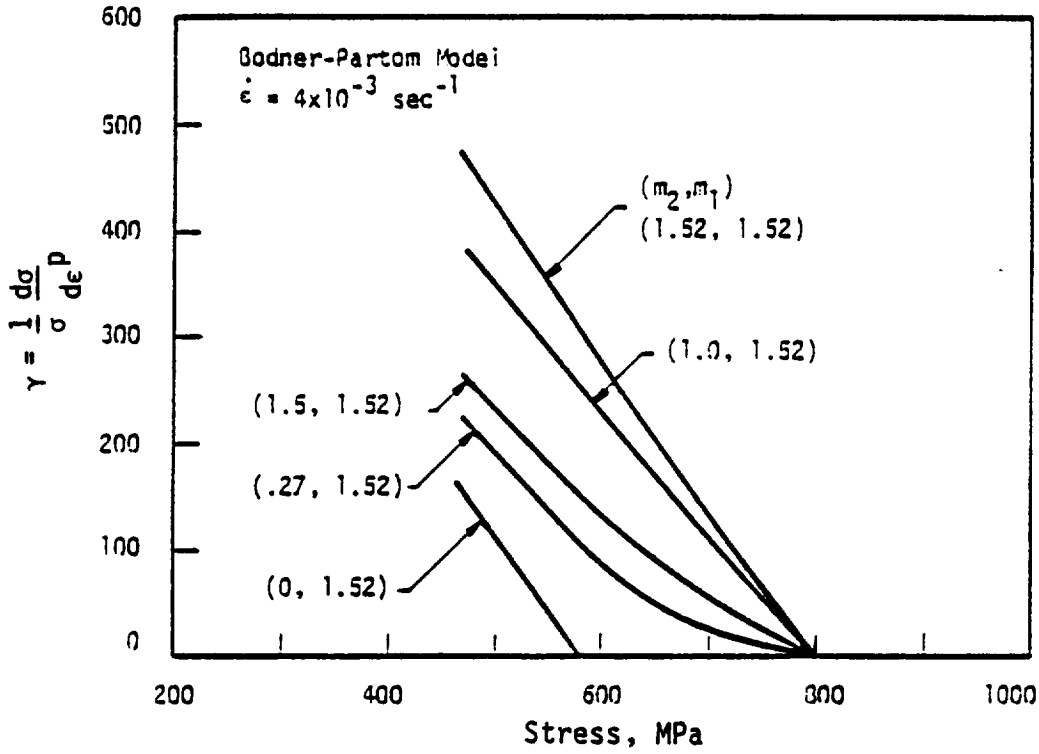

FIGURE 2.4 THE INFLUENCE OF THE VALUES OF m_2 ON THE SHAPE OF THE γ-σ CURVE EXAMINED BY VARYING THE m_2 FROM 0 TO 1.52 AT A CONSTANT VALUE OF m_1 = 1.52.

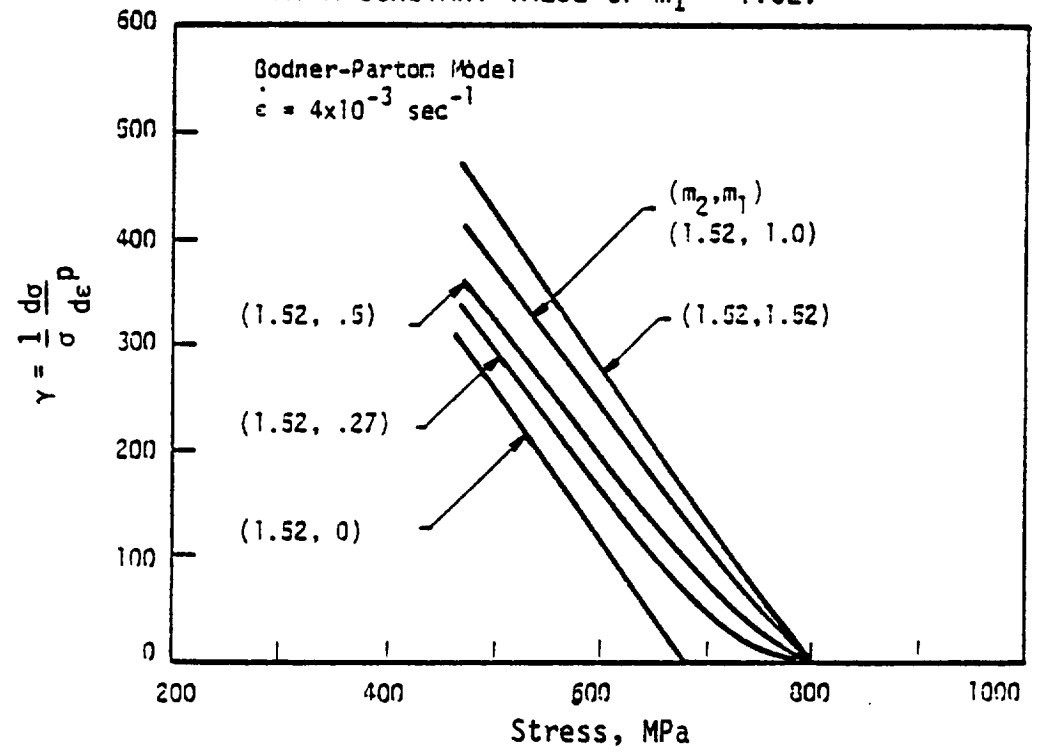

FIGURE 2.5 THE INFLUENCE OF THE VALUES OF m_1 ON THE SHAPE OF THE γ-σ CURVE EXAMINED BY VARYING THE m_1 FROM 0 TO 1.52 AT A CONSTANT VALUE OF m_2 = 1.52.

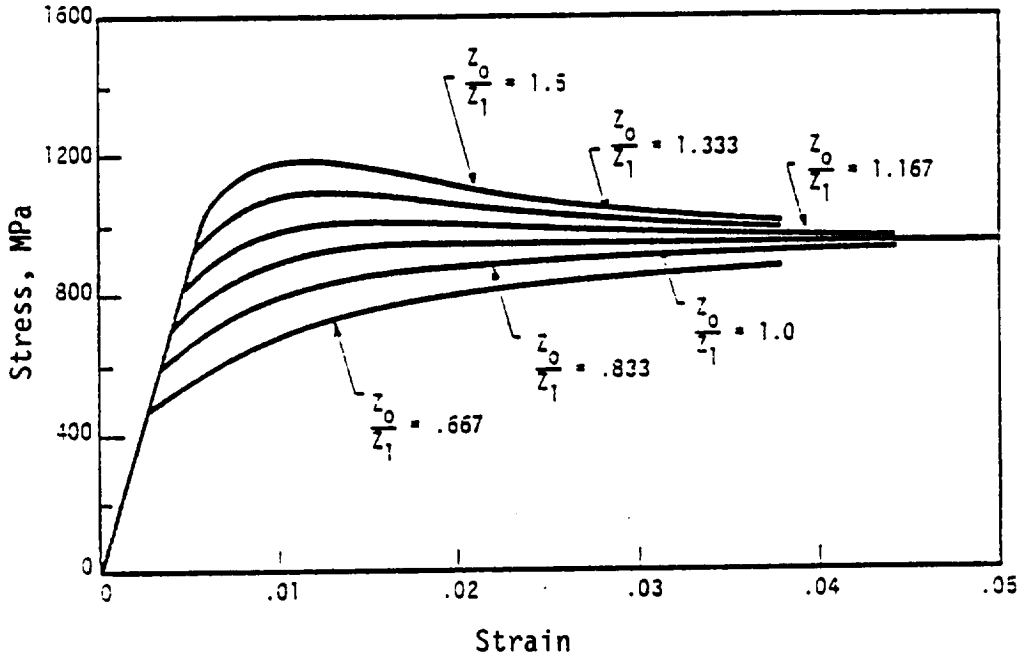

FIGURE 2.6 BODNER-PARTOM MODEL CALCULATIONS OF STRESS-STRAIN CURVES FOR VARIOUS VALUES OF Z_o/Z_1.

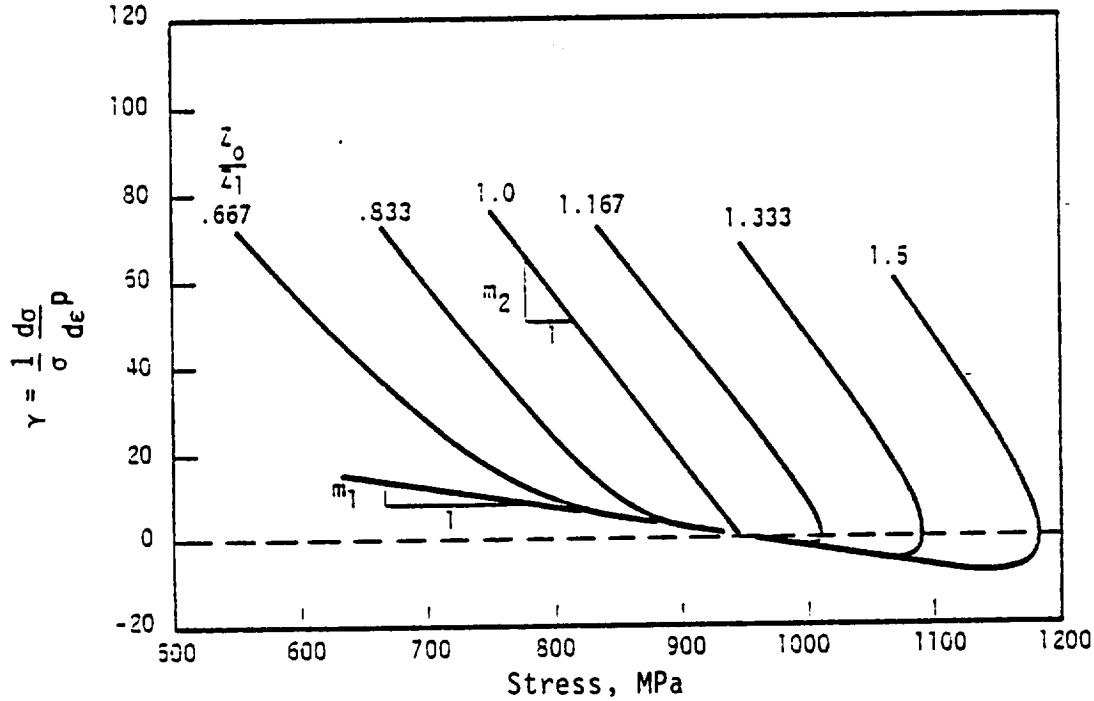

FIGURE 2.7 BODNER-PARTOM MODEL CALCULATIONS OF γ-σ CURVES FOR VARIOUS Z_o/Z_1 RATIOS.

stress for which Z equal to Z_1. The model calculations in Figure 2.7 show that the shape of the γ-σ curve also depends on the relative value of Z_o and Z_1. In addition, the procedures for obtaining m_1 and m_2 from linear portions of the γ-σ curve is applicable for both cyclic hardening and softening. To apply this procedure for cyclic softening materials, the experimental γ-σ curve must be obtained beyond the ultimate tensile strength, and it might be practically difficult to distinguish from data whether the decrease of load beyond the ultimate load is due to work softening, damage development, or diffuse necking. More study is therefore required for applying the γ-σ plot concept to cyclic softening materials.

2.2 Development of Test Procedures

The procedure for evaluating material constants in the Bodner-Partom model has been developed based on five primary response characteristics: (1) hardening response (γ-σ plots); (2) strain rate dependence ($ln\sigma_s$ vs. lnS plots); (3) thermal recovery behavior (q vs. σ_c-σ_o plot); (4) temperature dependence--some of the material constants are temperature-dependent, and (5) nonproportional hardening effects. The first four effects, discussed in Section 2.1, have been evaluated on the basis of uniaxial tensile and creep data from multiple specimens in the base program. At present, it seems that a set of 90° out-of-phase tension/ torsion data is also required for evaluating the nonproportional hardening effect.

A possible method for reducing the number of test specimens is to evaluate the first four effects from a specially designed tensile test. The suggested tensile test, shown in Figure 2.8, involves extending the specimen at an initial strain rate, $\dot{\varepsilon}_i$, to a prescribed strain level close to the

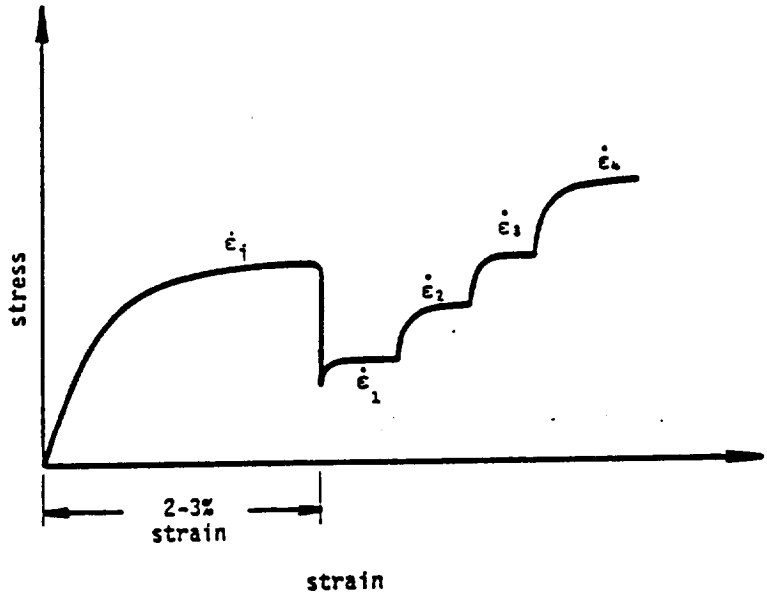

FIGURE 2.8 TENSILE TEST WITH STRAIN RATE JUMPS.

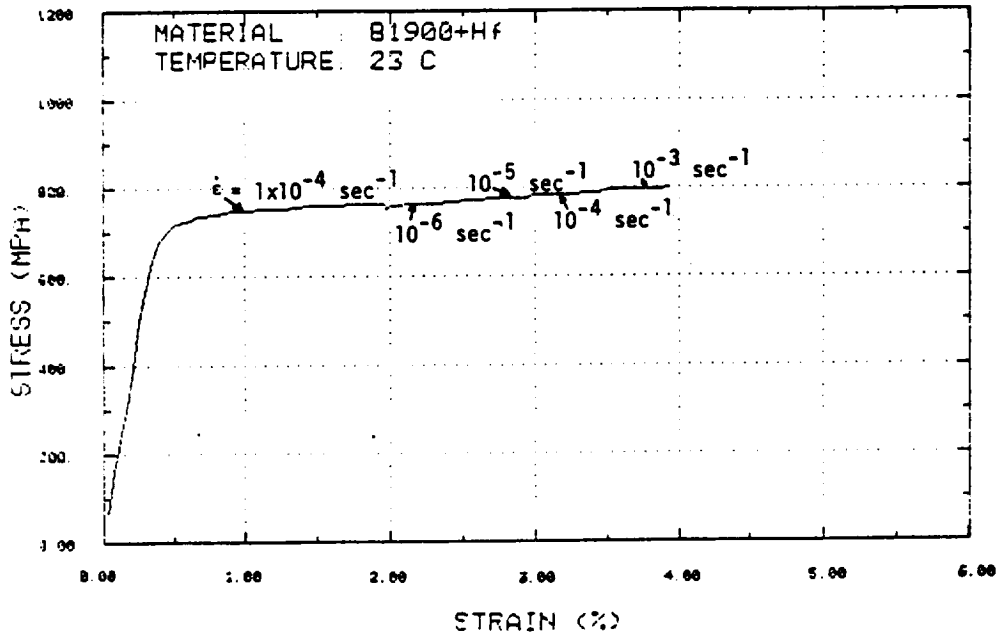

FIGURE 2.9 RESULT OF JUMP TEST FOR B1900+Hf AT 23°C.

saturated stress (ultimate) condition (to 2-3% in this case). After the prescribed strain is reached, the imposed strain rate would be changed to different values in a manner shown in Figure 2.8.

The presumed advantage of the proposed tensile test is that only one specimen is needed to interrogate both the hardening effect and the strain rate dependence of plastic flow at a given temperature, while at least two specimens are required for evaluating strain rate dependence in the conventional approach used in the base program. At elevated temperatures, the same test can also be used to evaluate the thermal recovery behavior by allowing the flow stress at a given strain rate to reach a steady state value before the strain rate is changed.

2.2.1 The "Jump" Tests

Tensile tests with strain rate jumps were conducted on a new set of B1900+Hf specimens at five different temperature in the range of 23-1093°C. As shown in Table 2.4, the initial strain rate was $1x10^{-4}$ sec^{-1}. The strain rate was subsequently lowered to 10^{-6} sec^{-1} and then increased by an order of magnitude after each increment of .5% strain. This process was repeated four times until the strain rate was increased to $1x10^{-3}$ sec^{-1}. Figures 2.9-2.11 show the jump test results for B1900+Hf at 23, 648, and 871°C. Note that B1900+Hf is rate-insensitive at 23°C, and rate-sensitive at 871°C. At 648°C, B1900+Hf shows negative rate-sensitivity at $\dot{\varepsilon} = 1x10^{-6}$ sec^{-1}, but shows strain-rate-insensitive plastic flow during subsequent strain rate increases from 10^{-5} to 10^{-3} sec^{-1}.

The analysis of these test results is given in Sections 2.3, 2.4 and in the Discussion.

TABLE 2.4

MATRIX OF TENSILE TESTS WITH STRAIN RATE JUMPS FOR B1900+Hf. The sequence of strain rate jumps is shown in Figure 2.8.

	Temperatures, °C					
	RT	648	760	871	982	1093
B1900+Hf	X	X		X	X	X

$\dot{\varepsilon}_i = 1x10^{-4}$ sec^{-1}, $\dot{\varepsilon}_1 = 1x10^{-6}$ sec^{-1}, $\dot{\varepsilon}_2 = 1x10^{-5}$ sec^{-1}, $\dot{\varepsilon}_3 = 1x10^{-4}$ sec^{-1}, $\dot{\varepsilon}_4 = 1x10^{-3}$ sec^{-1}

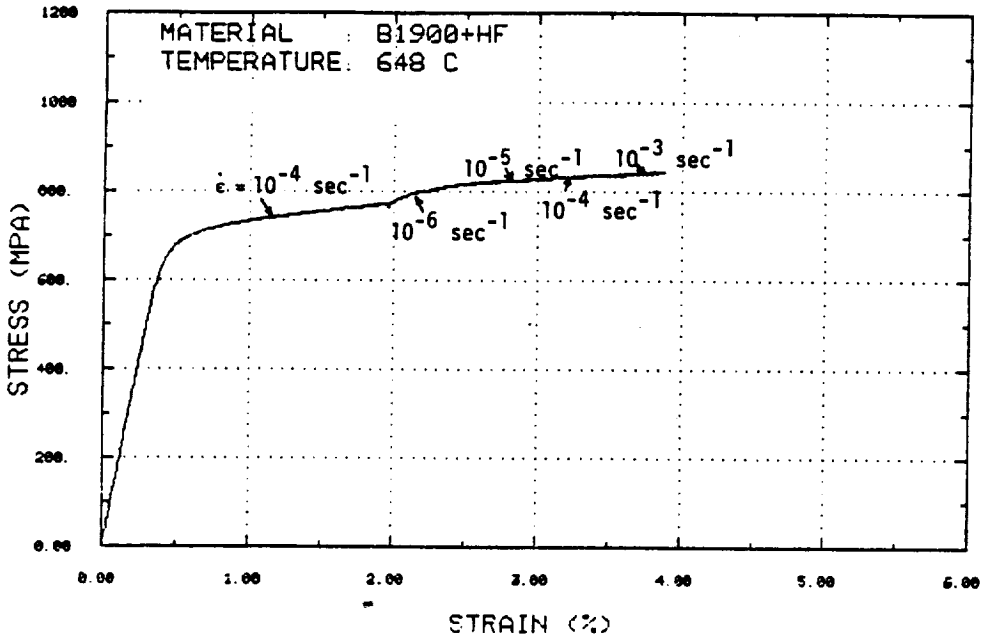

FIGURE 2.10 RESULT OF JUMP TEST FOR B1900+Hf AT 648°C.

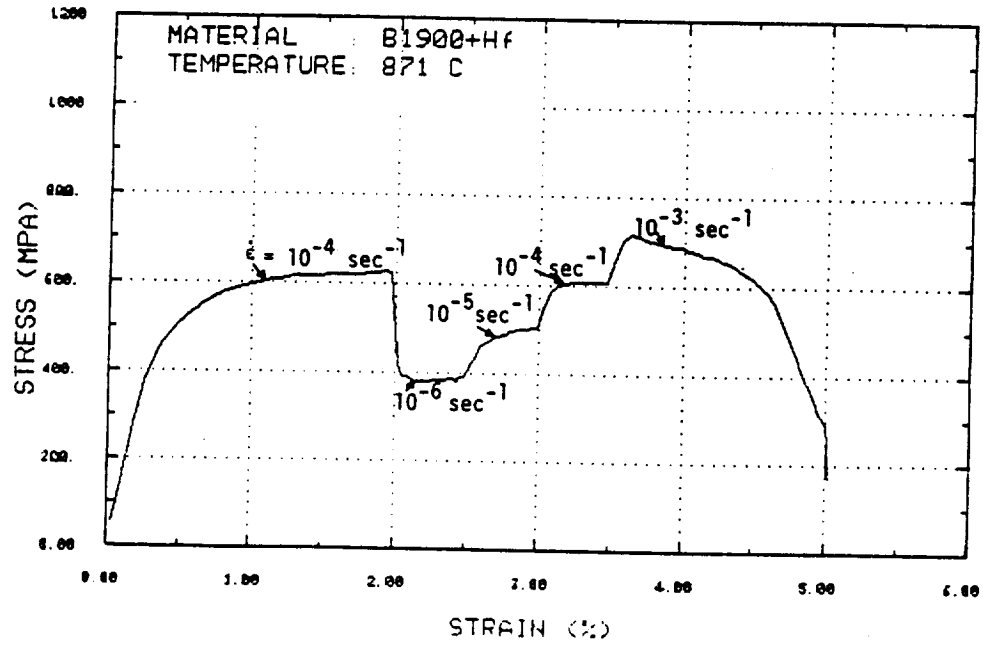

FIGURE 2.11 RESULT OF JUMP TEST FOR B1900+Hf AT 871°C.

2.2.2 Nonproportional Tension-Torsion Tests

One of the questions in developing an efficient test procedure for defining all material constants in a unified constitutive model is whether multiaxial tests are needed for interrogating nonproportional hardening effects and for evaluating material constants. Previous 90° out-of-phase tension-torsion tests in the base program indicated that for there is no additional cyclic hardening resulting from nonproportional strain cycling of B1900+Hf in the temperature range 648-982°C. This is in contrast to the nonproportional hardening behavior observed in Hastelloy-X at room temperature. To provide a better understanding of these conflicting observations, nonproportional multiaxial cyclic testing was performed for B1900+Hf at room temperature for two cycles at each of the following strain history sequences: (1) 90° out-of-phase combined tension-torsion, (2) in-phase combined tension-torsion, (3) fully reversed torsion, and (4) fully-reversed tension. The strain sequence was conducted twice on the same specimen at two effective strain range levels (±.4% and ±.6%). The results, shown in Figure 2.12 for an effective strain range of ±.4%, indicate that there is no additional cyclic hardening consequent to nonproportional loading. Previous nonproportional strain cycling of B1900+Hf at 648, 871, and 982°C also showed no evidence of additional cyclic hardening. The implication here is that at least one nonproportional multiaxial cyclic test is required to determine the nonproportional hardening constant in the Bodner-Partom model and possibly other unified models. A suggested nonproportional biaxial test for interrogating the nonproportional hardening effect would be a 90° out-of-phase tension-torsion test with a strain history such as that described above.

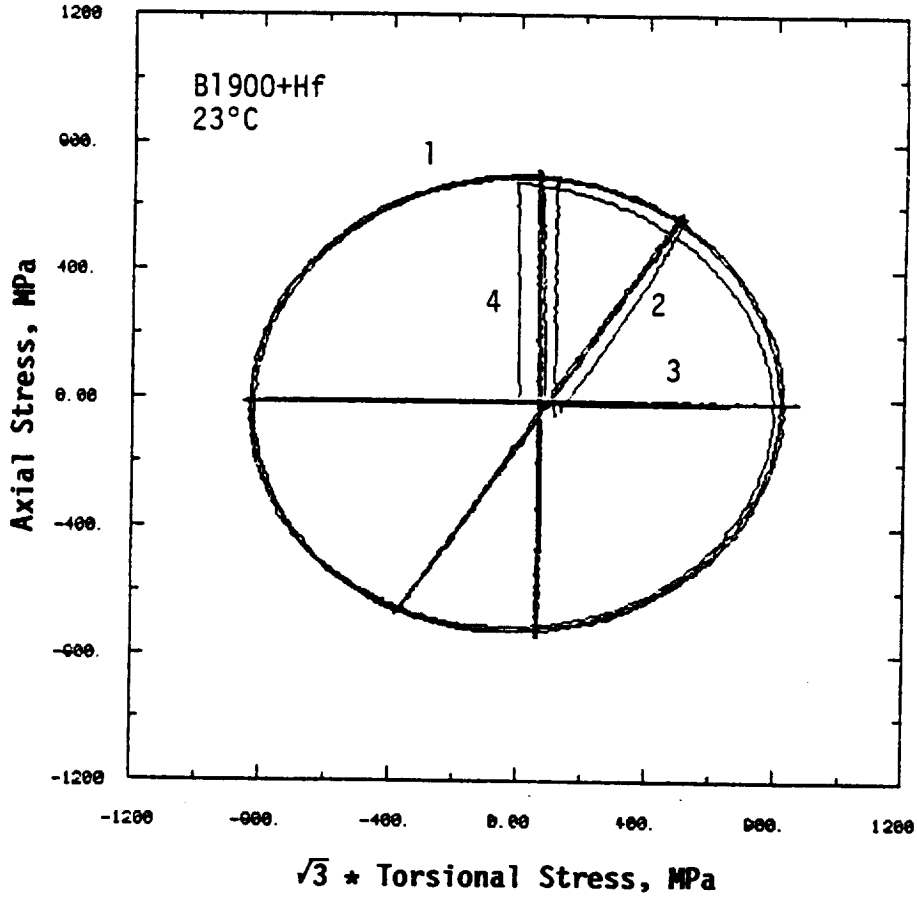

FIGURE 2.12 THE STRESS RESPONSE OF B1900+Hf TESTED UNDER: (1) 90° OUT OF-PHASE TENSION/TORSION, (2) IN-PHASE TENSION/TORSION, (3) TORSION, AND (4) TENSION. The effective strain and strain rate are $\pm$.4% and 4×10^{-1} sec^{-1}.

2.3 Evaluation of Model Constants (Using Data From Jump Tests)

The procedure described in Section 2.1.1 was used for determining the material constants of the Bodner-Partom model for the new set of B1900+Hf specimens. A set of γ-σ plots were generated based on stress-strain curves up to 2% strain at $\dot{\varepsilon} = 1 \times 10^{-4}$ sec^{-1}. The γ-σ plots for temperature below 871°C showed linear regions at both the low and high stress regimes, as illustrated in Fig. 2.13. Values of m_1 and m_2 determined from the γ-σ plots are summarized in Table 2.5. At temperatures above 871°C, thermal recovery is important; m_1 and m_2 cannot be evaluated from the γ-σ plots but are assumed to have values equal to those at the lower temperatures. From the γ-σ plots, the saturation stress σ_s and the stress σ_b were obtained.

The value of n at 871°C was determined from Eq. 2.9. The procedure used for obtaining the stress change resulting from a rapid strain rate change was based on the technique illustrated in Fig. 2.14. The assumptions were was that the value of the internal variable, Z, remains constant during the strain rate jump from $\dot{\varepsilon} = 1 \times 10^{-4}$ to 1×10^{-3} sec and presumed to be at the saturation condition, the basic material properties have not changed due to damage development or specimen necking, and, more fundamentally, that a jump test does not introduce factors not considered in the overall formulation. This strain rate jump was chosen for computing n because the relatively high strain rate would be least affected by thermal recovery. Only the value of n was measured in this manner. The presence of strain aging at 23 and 648°C and thermal recovery at 982 and 1093°C precluded the use of this technique for determining the values for n at those temperatures.

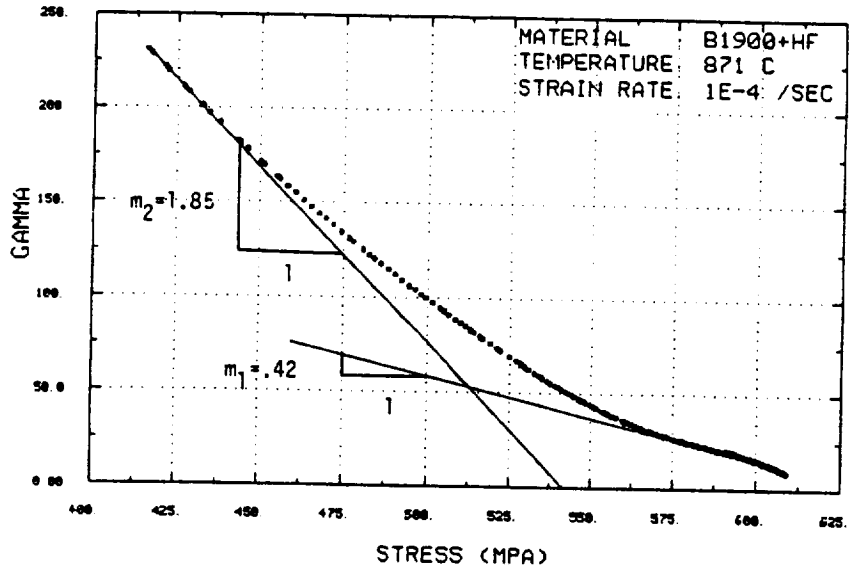

FIGURE 2.13 THE γ-σ PLOT OF B1900+Hf AT 871°C SHOWING m_1=1.85 AND m_2= .42.

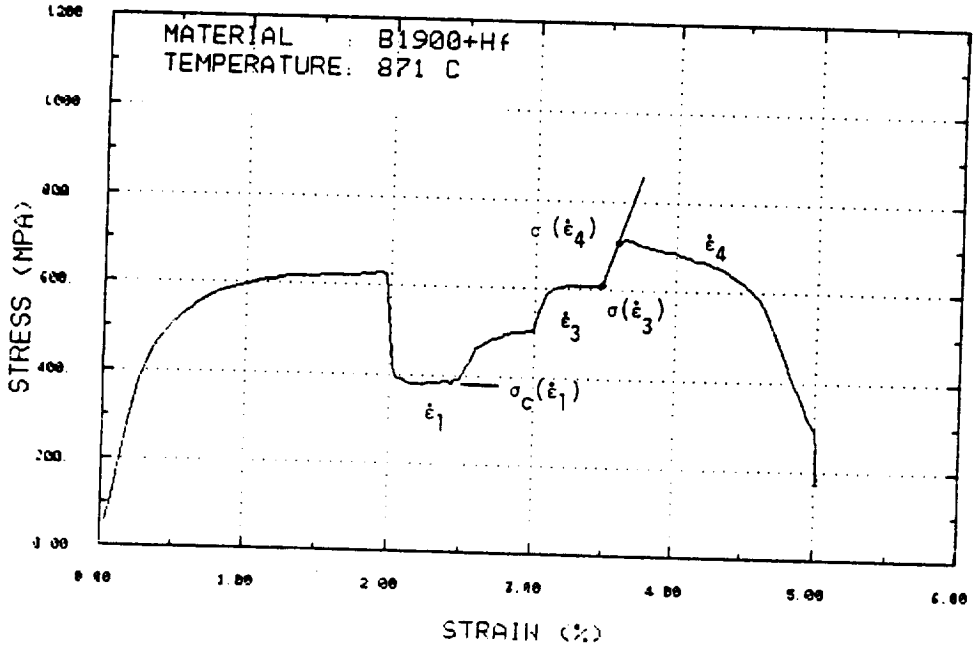

FIGURE 2.14 PROCEDURE FOR OBTAINING THE STRESS VALUES ASSOCIATED WITH AN INSTANTANEOUS STRAIN RATE JUMP AND THE STEADY STATE STRESS VALUE.

TABLE 2.5

BODNER-PARTOM MODEL CONSTANTS DETERMINED FOR B1900+Hf
IN THE OPTIONAL PROGRAM

- Temperature-Independent Constants

  $m_1 = .20\ MPa^{-1}$

  $m_2 = 1.85\ MPa^{-1}$

  $\alpha_1 = 0.0$

  $Z_1 = 29000\ MPa$

  $Z_3 = 8500\ MPa$

  $D_o = 1x10^4\ sec^{-1}$

- Temperature-Dependent Constants

Constants	23°C	648°C	871°C	982°C	1093°C
n	.465	.465	.446	.420	.387
Z_o (MPa)	28000	28000	23000	17500	11500
$A_1 = A_2$ (sec^{-1})	0	0	.001	.1	3
$Z_2(=Z_o)$ (MPa)	28000	28000	23000	17500	11500
$r_1 = r_2$	2	2	2	2	3

Once the value of n for 871°C was known, the sum of Z_1 and Z_3 was calculated using Eq. 2.7 and the saturation stress determined from the γ-σ plot. Using Eq. 2.11, Z_o was initially calculated using the .2% offset yield stress. Subsequent calculations, however, indicated that the proportional limit gave a value for Z_o which better matched the experimental stress-strain curve. Thus, σ_o was taken to be the proportional limit. Then, Z_2 was set to equal to Z_o; the values of Z_1 and Z_3 was obtained by means of Eq. 2.13 and 2.14, respectively.

Assuming Z_1 and Z_3 to be temperature and strain-rate-independent, the values for n at 23, 648, 982, and 1093°C were computed using Eq. 2.9 based on known values of Z_1, Z_3 and σ_s at $\dot{\varepsilon} = 1 \times 10^{-4}$ or 1×10^{-3} sec^{-1}. It is noted that the single jump test at 871°C serves a critical function in this test series since it provides the parameter n for all the other test conditions. This was a consequence of strain aging being present at temperatures lower than 871°C, thermal recovery being important at higher temperatures, and that only a single test was planned at 871°C. The n values for 982 and 1093°C were later slightly modified by fitting the model to the tensile stress-strain curves.

The thermal recovery constants were determined from the steady state stress associated with a given strain rate in the "jump" tests. As illustrated in Fig. 2.14, the steady state stress corresponds to the condition at which the work hardening rate is zero. To reduce the number of material constants in the Bodnèr-Partom model, r_1 and r_2 were assumed to be equal to r (r_2=r_1=r) and A_1 and A_2 were also assumed to be equal to A (A_1=A_2=A). The thermal recovery exponent was obtained by plotting q, given in Eq. 2.17, against σ_c-σ_o in a log-log plot. Such a representation usually yields a

linear relationship between q and $\sigma_c - \sigma_o$, and the slope of a linear q vs. $(\sigma_s - \sigma_c)$ curve is r. Such a plot for the new B1900+Hf tests is shown in Fig. 2.15, and r was determined to be 2 at 982°C and equal to 3 at 1093°C. Once r was evaluated, the thermal recovery coefficient A was calculated from Eq. 2.18 based on the known values of q, r, and other model constants.

2.4 Comparison of Model Constants for B1900+Hf

Tables 2.5 and 2.6 show the Bodner-Partom model constants for B1900+Hf determined in the optional program and in the base program, respectively. Inspection of Tables 2.5 and 2.6 reveal that the values for m_1 and m_2 are similar. The difference in the m_2 values in both sets of constants are primarily due to the change in the analysis of the γ-σ plot which leads to equating the slope of the initial linear portion of the γ-σ curve to m_2 rather than the sums of m_1 and m_2 as in the base program. On the other hand, substantial differences occur in the values of n, Z_o, Z_1, Z_2, and Z_3 in both sets of Bodner-Partom model constants for B1900+Hf. A thorough reexamination of the experimental data and the procedures for determining the model constants indicates that the critical parameter is the value of n at 871°C. Comparison of the saturation stress of B1900+Hf at 871°C obtained in both the base and the optional program is shown in Figure 2.16. In the base program, the n value was determined to be 1.03 from the slope of the σ_s vs. S curve, as represented by the solid line in Figure 2.16 (based on 4 tests). On the other hand, the n value obtained from the single jump test was 0.446 which is represented by the dash line in Figure 2.16. It is noted that the saturation stress for this specimen is considerably lower than that obtained

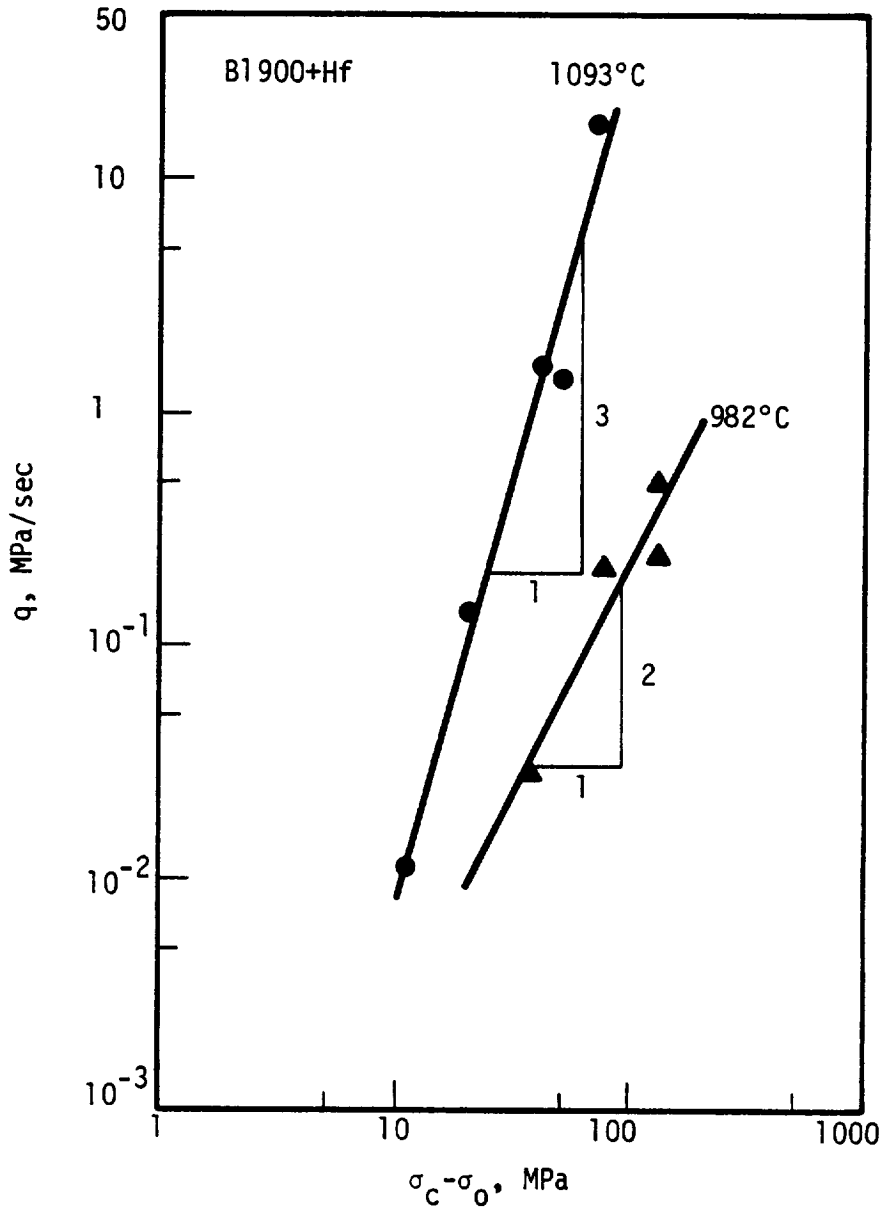

FIGURE 2.15 PLOT OF q VS. $\sigma_c-\sigma_o$ SHOWING r = 3 AT 1093°C AND r = 2 AT 982°C.

TABLE 2.6

BODNER-PARTOM MODEL CONSTANTS DETERMINED FOR B1900+Hf
IN THE BASE PROGRAM

o Temperature-Independent Constants

$m_1 = .270\ MPa^{-1}$

$m_2 = 1.52\ MPa^{-1}$

$\alpha_1 = 0.0$

$Z_1 = 3000\ MPa$

$Z_3 = 1150\ MPa$

$r_1 = r_2 = 2$

$D_o = 1x10^4\ sec^{-1}$

o Temperature-Dependent Constants

		Temperature, °C		
Constants	$T \leq 760°C$	871°C	982°C	1093°C
n	1.055	1.03	.850	.70
Z_o (MPa)	2700	2400	1900	1200
$A_1 = A_2$ (sec^{-1})	0	.0055	.02	.25
$Z_2(=Z_o)$ (MPa)	2700	2400	1900	1200

o Elastic Moduli for B1900+Hf

$E = 1.987 \times 10^5 + 16.78\ T - .1034\ T^2 + 1.143 \times 10^{-5}\ T^3$ MPa with T in °C.

$G = 8.650 \times 10^4 - 17.58\ T + 2.321 \times 10^{-2}\ T^2 - 3.464 \times 10^{-5}\ T^3$ MPa with T in °C

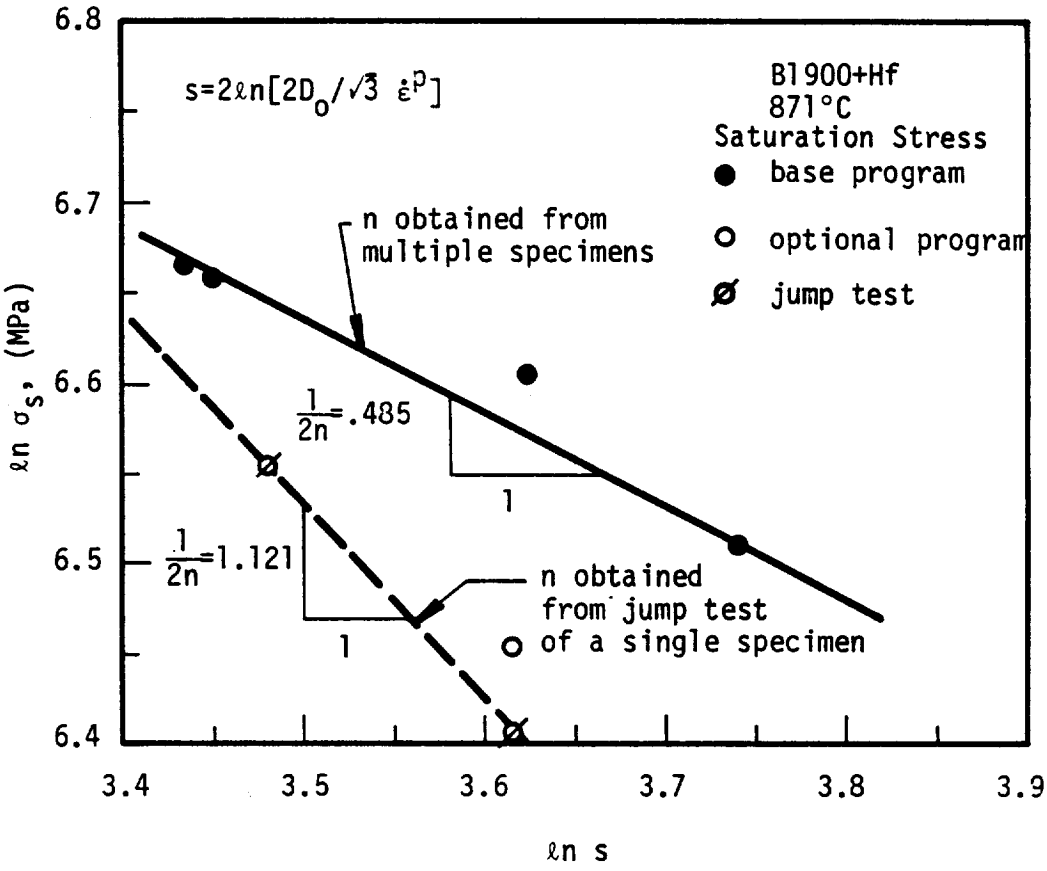

FIGURE 2.16 COMPARATION OF SATURATION STRESS VALUES OBTAINED IN THE BASE AND OPTIONAL PROGRAMS.

in the base program. The difference in the saturation stress at $\dot{\epsilon} = 1 \times 10^{-4}$ sec^{-1} is also reflected in the stress-strain curves, shown in Figure 2.17(a). It therefore appears that the new set of specimens differ significantly from those used in the base program with respect to strain rate sensitivity (n) and the overall flow stress level (σ_s). On the basis of the procedure using the γ-σ relation, the set of hardening constants Z_i is directly associated with the value of n. The consequence of a lower n value would be larger values for Z_o, Z_1, Z_2, and Z_3, through the relations represented in Eqs. 2.9 and 2.11. Since the constants Z_1 and Z_3 at 871°C which are based on the value of n obtained from the jump test, were used to compute the n values for the other temperatures, those values of n are actually extrapolations of the single test result for n.

Figure 2.17(b) and (c) show the stress-strain curves for three strain rates calculated using the old and the new set of Bodner-Partom model constants for B1900+Hf at 871°C. Both sets of constants give stress-strain curves which are in reasonable agreement with the respective experimental data. The significant difference in Fig. 2.17(b) and (c) is in the stress-strain curve for $\dot{\epsilon} = 1 \times 10^{-4}$ sec^{-1}. In this case, the old constants (base program) yield results which are in agreement with data obtained in the base program (the solid line), while the new constants (optional program) yield results which are in agreement with data obtained in the optimal program (the solid line with symbols). Comparisons of calculated and experimental stress-strain curves at various temperatures are shown in Fig. 2.18(a) and (b) for the experiment and calculations based on old and the new constants, respectively; again, there is reasonable agreement between model calculations and experimental results in the range of temperature considered.

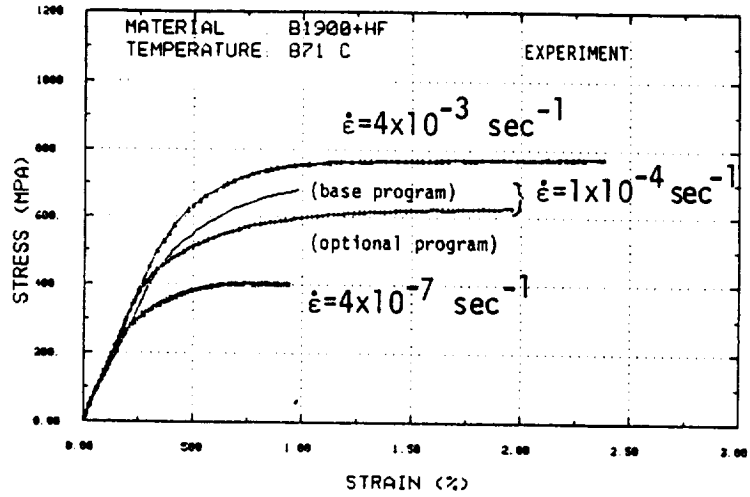

(a)

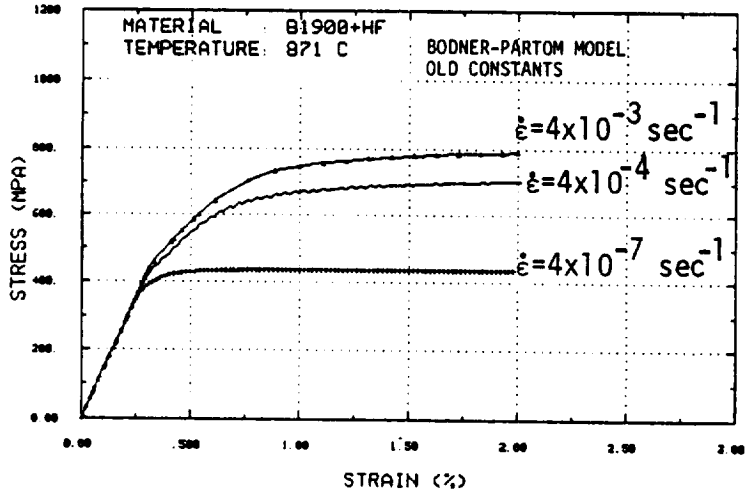

(b)

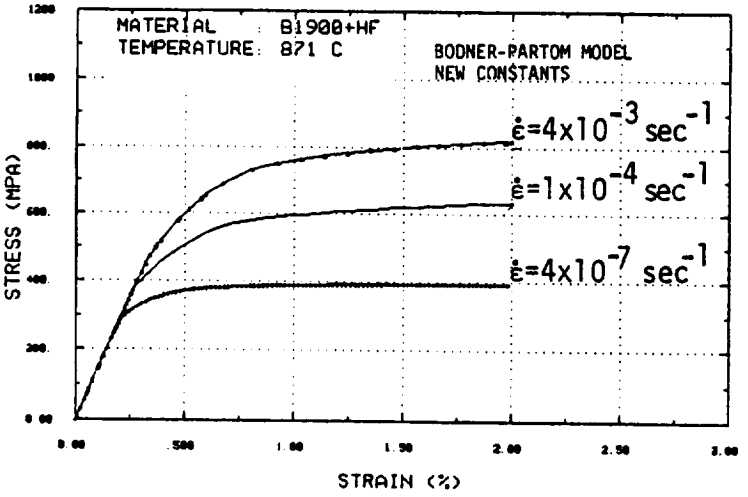

(c)

FIGURE 2.17 COMPARISON OF STRESS-STRAIN CURVES OF B1900+Hf: (a) EXPERIMENT, (b) CALCULATION WITH THE OLD CONSTANTS, AND (c) CALCULATION WITH THE NEW CONSTANTS. Note the substantial difference observed in the experimental curves obtained in the base and the optional program for 871°C.

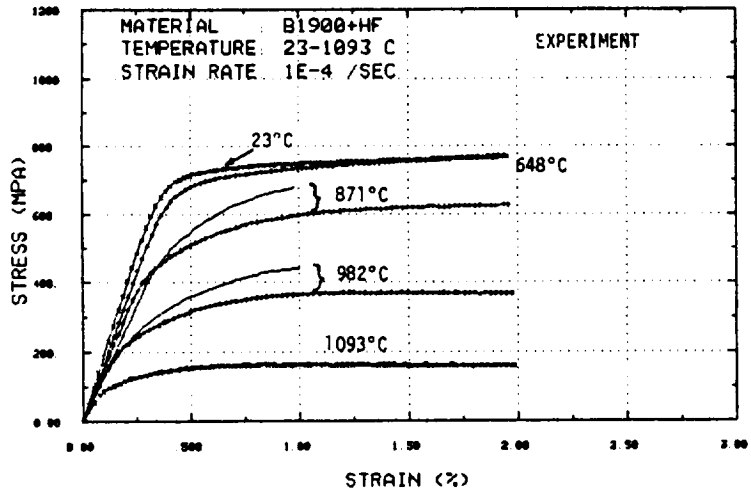

(a)

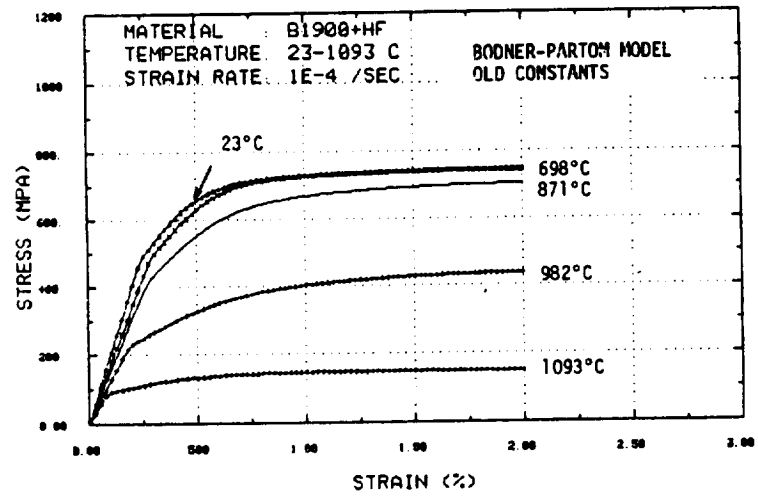

(b)

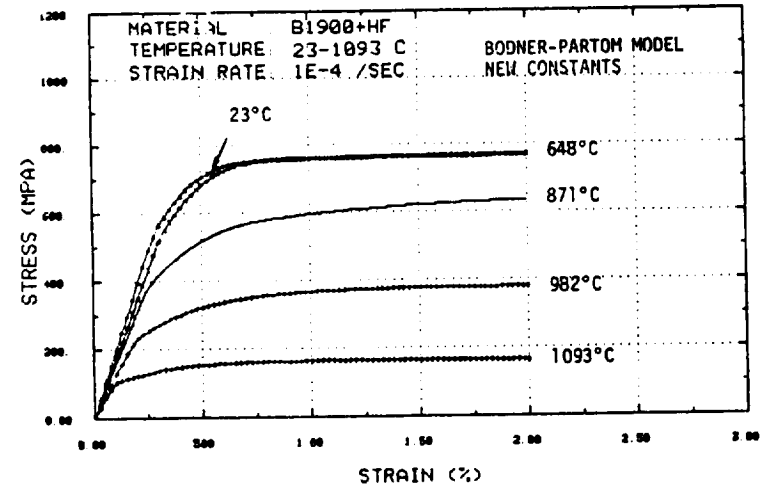

(c)

FIGURE 2.18 COMPARISON OF STRESS-STRAIN CURVES OF B1900+Hf AT FIVE DIFFERENT TEMPERATURES: (a) EXPERIMENT, (b) CALCULATION WITH THE OLD CONSTANTS, AND (c) CALCULATION WITH THE NEW CONSTANTS.

It should be noted here that modeling of the shape of a single stress-strain curve depends on obtaining appropriate hardening and recovery constants from the γ-σ relation for a particular value of the rate sensitivity parameter n. That is, the modeling procedure permits alternative values of n to lead to comparable stress-strain curves at a given strain rate and temperature. Only suitable rate sensitivity tests could provide the proper n value.

Another exercise involving the two sets of model constants are stress-strain calculations involving strain-rate jumps. These results are shown in Fig. 2.19 for 1093°C which indicates that reasonable agreement is obtained for both sets of material constants. For this temperature and strain rate history, the response is governed primarily by the hardening and recovery properties and is not sensitive to the particular value of n. A properly chosen set of hardening and recovery constants corresponding to a given n value would therefore lead to reasonable response characteristics under these conditions. It would seem, however, from the results of the jump from 10^{-4} to 10^{-3} sec^{-1} that the n value used for the new set of constants may be too low since the computed stress jump is too large.

A further check on the procedure for determining n based on the jump test is to examine the value of the internal variable and the history of the plastic strain rate during a strain rate change at 871°C. Figure 2.20(a) shows the experimental stress-strain curve compared with the calculated curve using the new set of model constants. The corresponding calculated total and plastic strain rate histories are shown in Fig. 2.20(c), while Z, which is the sum of Z^I and Z^D, is shown in Fig. 2.20(b). During a strain rate jump from $\dot{\varepsilon} = 1 \times 10^{-4}$ to 1×10^{-3} sec^{-1}, the calculated Z remains relatively constant and the resulting change of stress would therefore be a reasonable

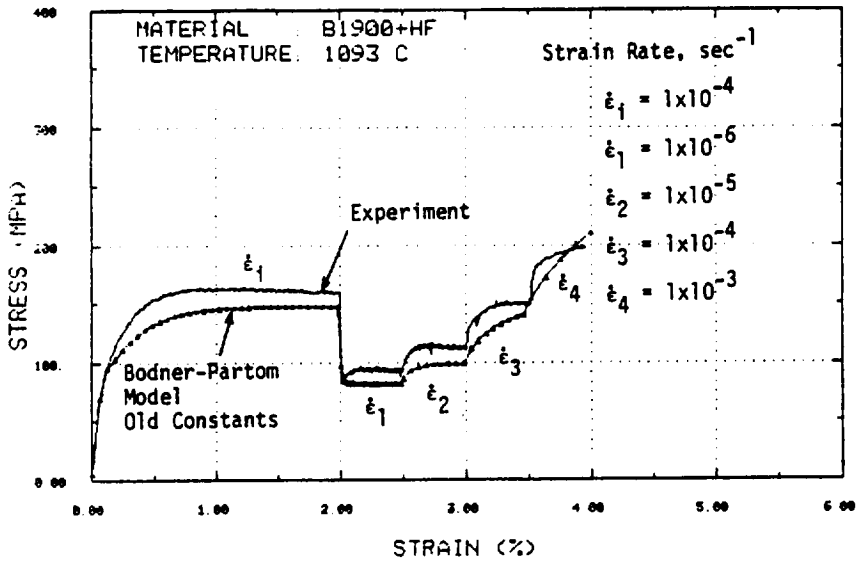

(a)

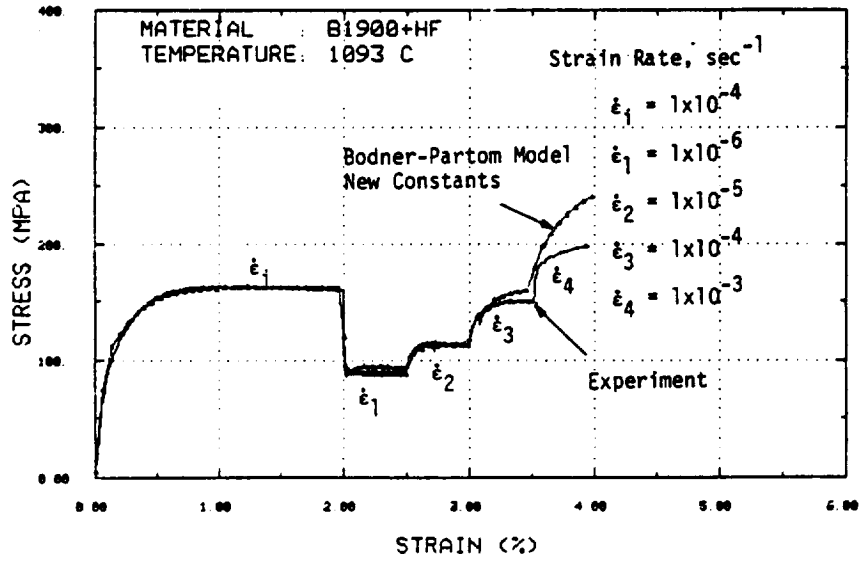

(b)

FIGURE 2.19 COMPARISON OF RESULTS FOR TENSILE TEST WITH STRAIN RATE JUMP AT 1093°C: (a) EXPERIMENT/MODEL CORRELATION WITH OLD CONSTANTS, AND (b) EXPERIMENT/MODEL CORRELATION WITH NEW CONSTANTS

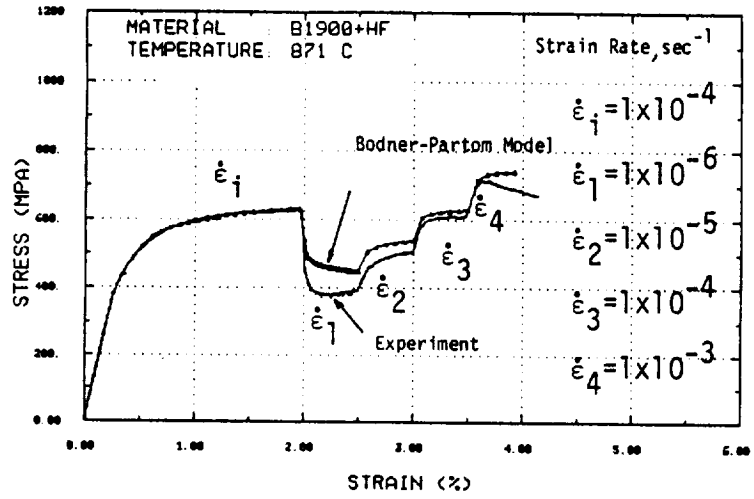

(a)

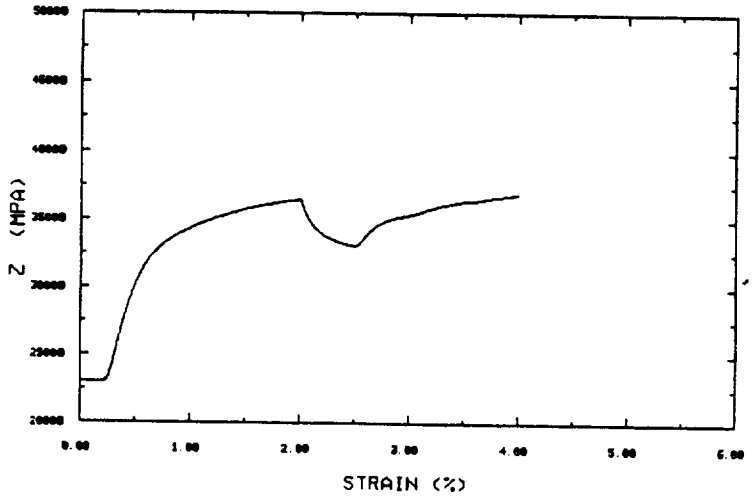

(b)

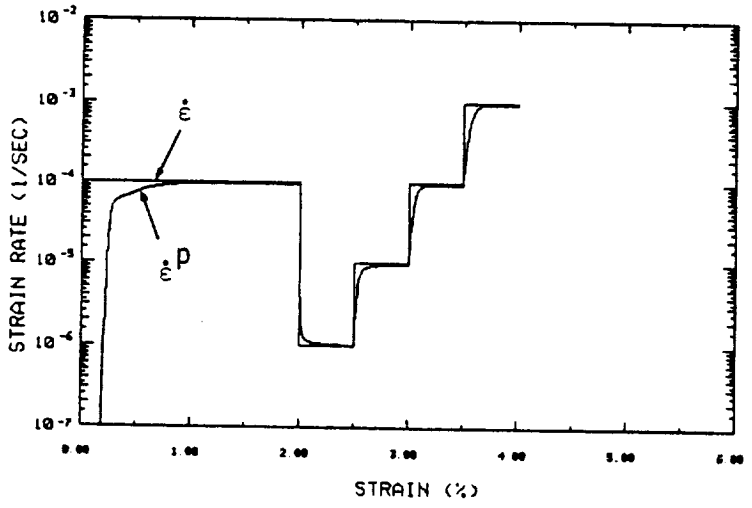

(c)

FIGURE 2.20 TENSILE TEST WITH STRAIN RATE JUMPS AT 871°C: (a) EXPERIMENT/MODEL CORRELATION WITH NEW CONSTANTS, (b) HISTORY OF Z, AND (c) HISTORY OF THE APPLIED AND THE PLASTIC STRAIN RATES.

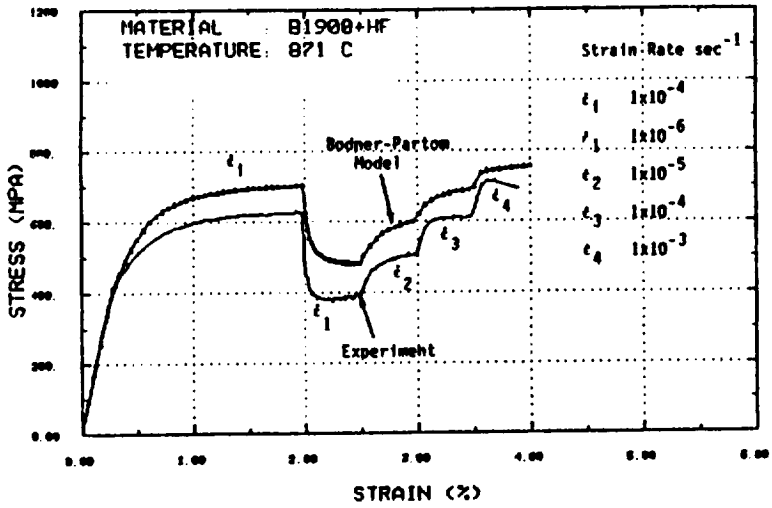

(d)

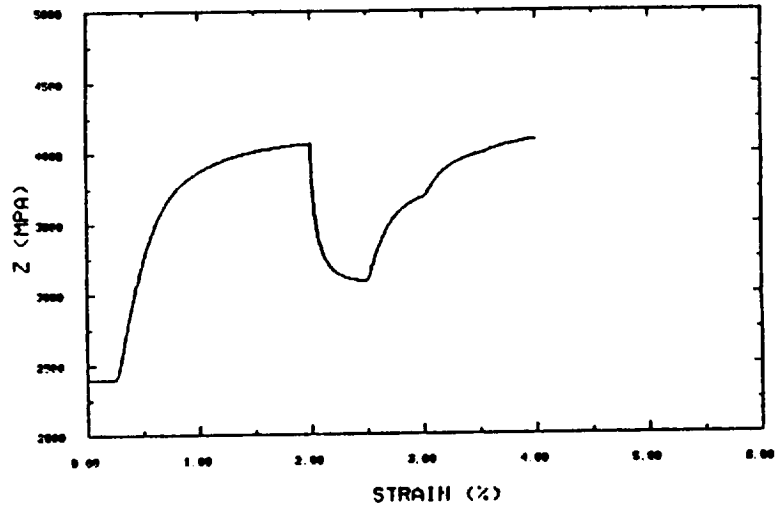

(e)

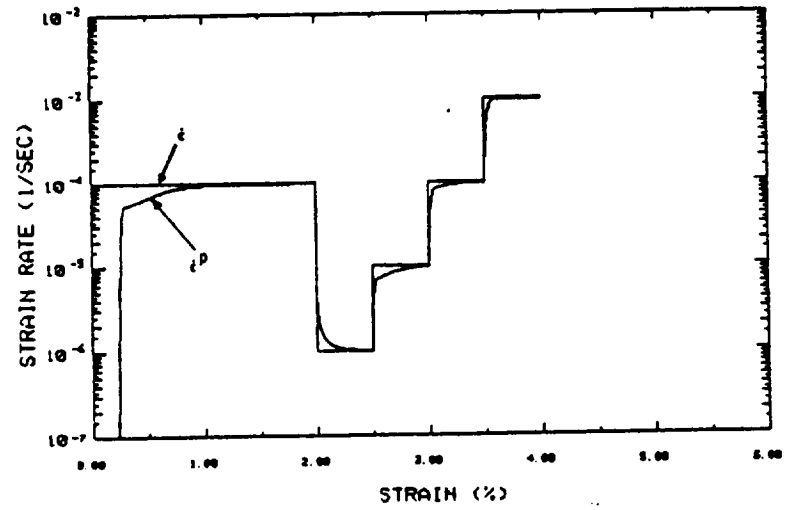

(f)

FIGURE 2.20 (Continued) TENSILE TEST WITH STRAIN RATE JUMPS AT 871°C: (d) EXPERIMENT/MODEL CORRELATION WITH OLD CONSTANTS, (e) HISTORY OF Z (OLD CONSTANTS), AND (f) HISTORY OF THE APPLIED AND THE PLASTIC STRAIN RATES (OLD CONSTANTS).

measure of the strain rate dependence of plastic flow if other factors did not enter. On the other hand, Z is not constant during a strain rate jump from $\dot{\varepsilon} = 1 \times 10^{-6}$ to 1×10^{-5} sec^{-1}; the resulting stress change include contributions of both thermal recovery and strain rate dependence of plastic flow. An evaluation of n based on the stress change associated with a strain rate jump in this range would yield erroneous results. For comparison purposes, the corresponding calculations using the old set of constants are shown in Figs. 2.20(d), (e), and (f).

These considerations indicate that each set of the Bodner-Partom model constants is self consistent and leads to reasonable representation of the stress-strain curves at a number of strain rates and temperatures in the range of the current test program. This suggests that the discrepancies in the two sets of constants may be due, in part, to the difference in the data base (material properties) which was used to obtain the constants, and partly to uncertainties in the jump test which could not be fully checked due to limitations of the test program. In particular, the specimen used for the jump test at 871°C appears to differ from those in the base program. This exercise points out that the possible variability of material properties could negate the advantages of efficient test procedures that rely on a small number of test specimens. A useful check of the jump test procedure would be to perform a monotonic test at the higher strain rate, e.g. $\dot{\varepsilon} = 1 \times 10^{-3}$ sec^{-1}. This test would be performed in the coming year program.

2.5 Grain Size Effects

The tensile test data of B1900+Hf at 871 and 982°C obtained in the base and the optional program show relatively large specimen to specimen

variations [see Fig. 2.17(a) and Fig. 2.18(a)]. A variable that may influence the behavior of the material is the casting grain size. Depending upon the complexity of the casting, a considerable variation in the grain size may occur within the same component. A limited test program was conducted to explore the effects of grain size. Five (5) smooth specimens were cast with a grain size different from that of the base material studied in the previous tasks by adjusting casting preheat temperature. The surface grain size of the based material is .8 mm (ASTM grain size number of -2 to -3)* while that for this task is 2.5 mm (ASTM grain size number of -5 to -6) (Fig. 2.21). To examine the effects of grain size on yield stress, hardening and strain rate sensitivity, the jump test described in the previous section was used. Figures 2.22 and 2.23 show the results for tests at 648 and 982°C. There was no significant difference observed in the yield stress and hardening behavior of the specimens with the two grain size at $\dot{\varepsilon} = 1 \times 10^{-4}$ sec^{-1} at both temperatures. There are only small differences in the strain rate sensitivity at 648°C and in the thermal recovery at 982°C. Cyclic tests were also performed at 982°C for three different imposed strain ranges. Figure 2.24 indicates that there is essentially no difference in the cyclic behavior. Based on these limited tests, it appears that variations in the casting grain size is probably not the responsible factor for the variation in material properties described earlier.

* A subgrain size of ASTM grain size number of 1 to 2 was reported in the previous reports [1,2].

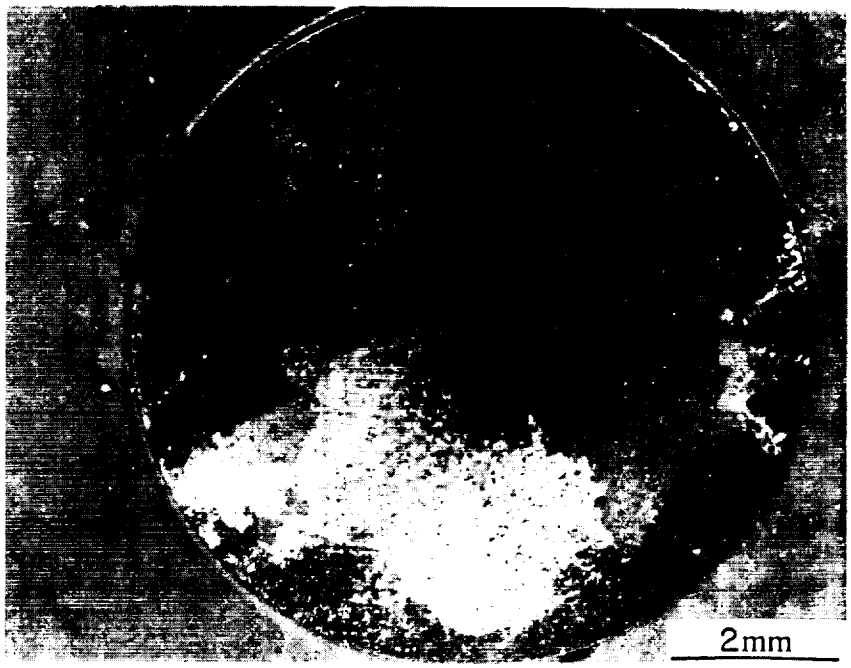

(a)

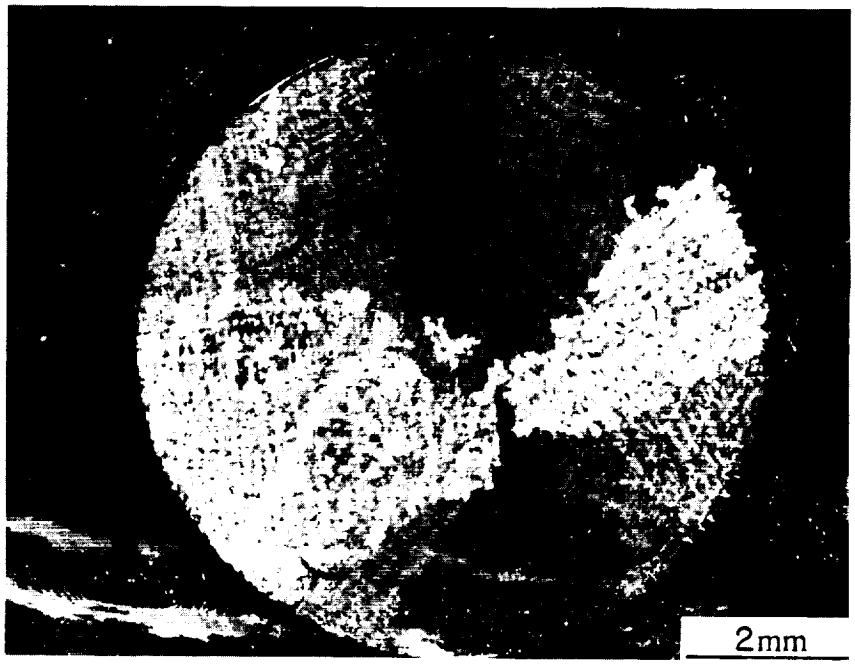

(b)

FIGURE 2.21 COMPARISON OF GRAIN SIZES OF CAST B1900+Hf SPECIMENS IN THE BASE PROGRAM AND IN TASK J4 OF THE OPTIONAL PROGRAM: (a) BASE PROGRAM, ASTM GRAIN SIZE NO. -2 TO -3, AND (b) TASK J4, ASTM GRAIN SIZE NO. -5 TO -6.

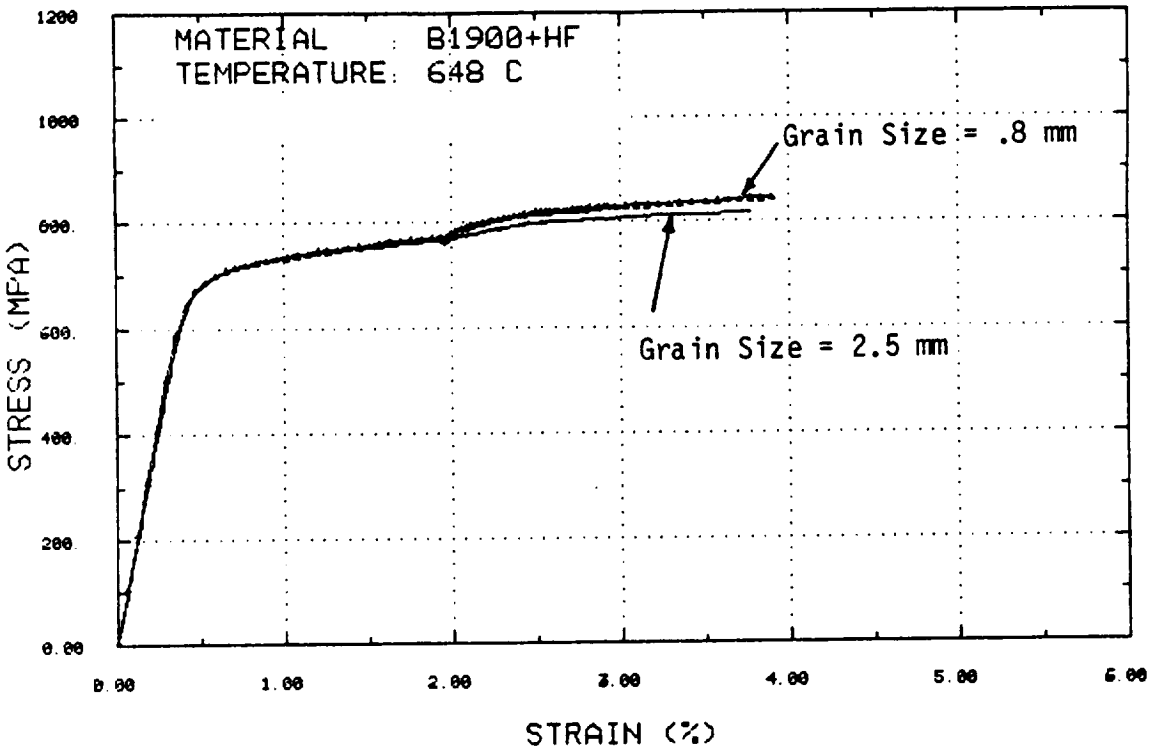

FIGURE 2.22 COMPARISON OF JUMP TEST RESULTS FOR B1900+Hf SPECIMENS AT 648°C AND WITH TWO DIFFERENT GRAIN SIZES.

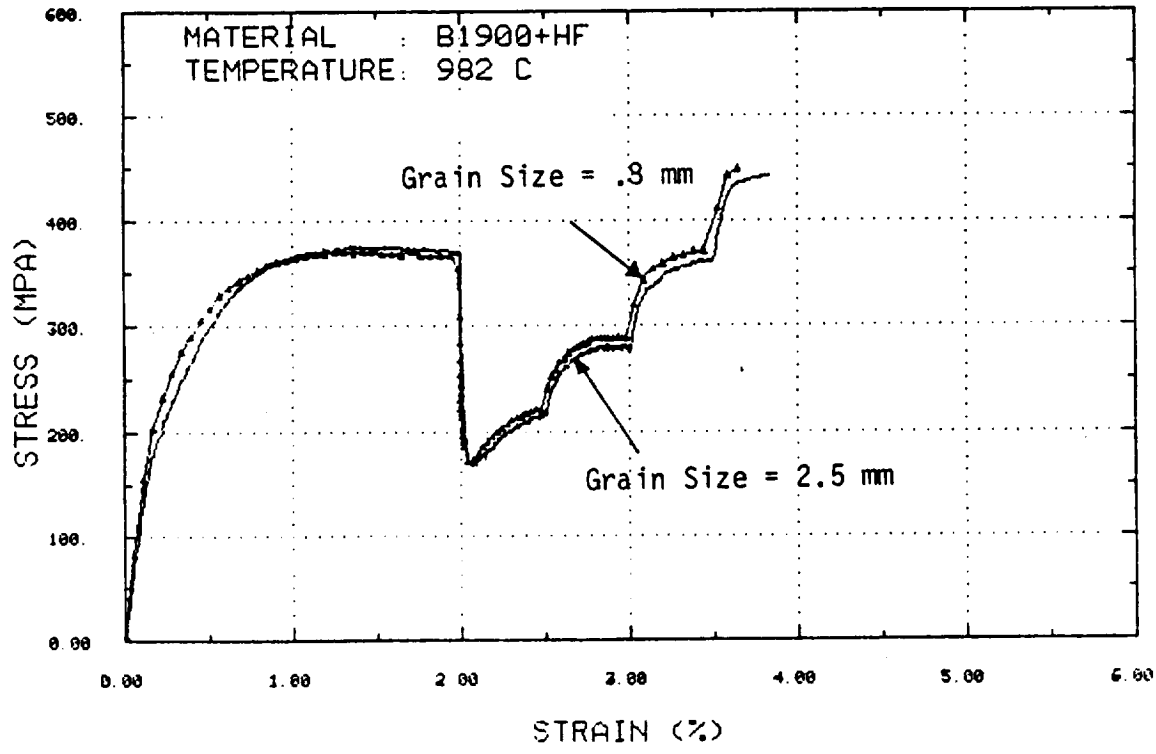

FIGURE 2.23 COMPARISON OF JUMP TEST RESULTS FOR B1900+Hf SPECIMENS AT 648°C AND WITH TWO DIFFERENT GRAIN SIZES.

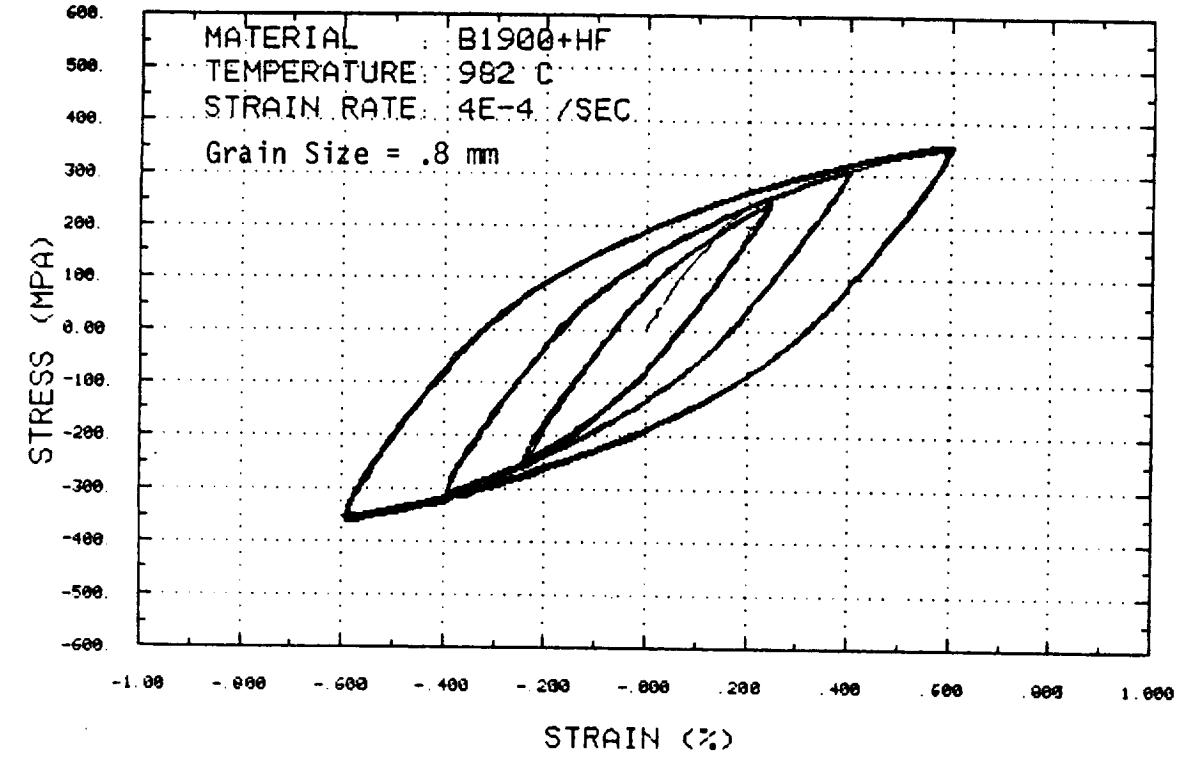

(a)

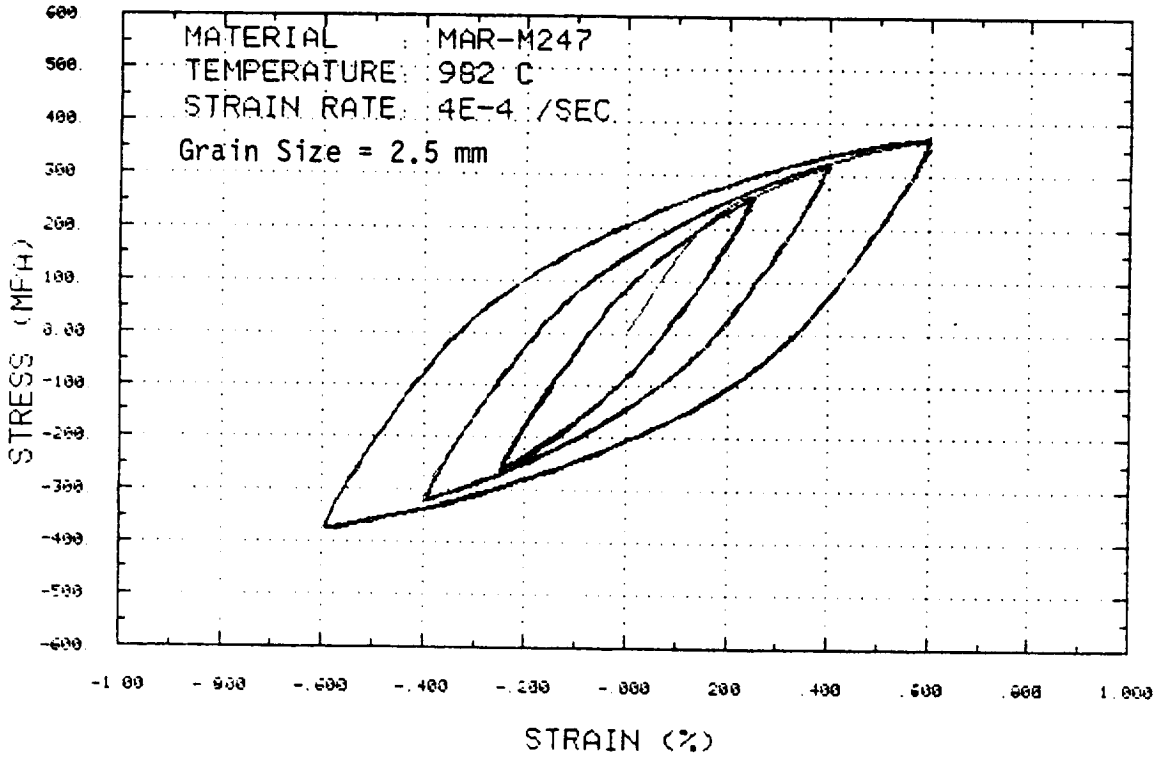

(b)

FIGURE 2.24 COMPARISON OF CYCLIC BEHAVIOR OF B1900+Hf SPECIMENS WITH TWO DIFFERENT GRAIN SIZES: (a) .8 mm, AND (b) 2.5 mm.

2.6 Discussion

The results in Task J indicate that for known values of n and D_o the γ-σ plots provide information from which the material constants m_1, m_2, Z_1, and Z_3 can be evaluated. From tensile tests with strain rate jumps, the constants Z_o, Z_2, A, and r can also be obtained. Thus, it appears feasible to evaluate all the hardening and thermal recovery constants in the Bodner-Partom model at a given temperature by performing suitable jump tests on a single specimen. However, the capability for determining the strain rate sensitivity parameter n from a single jump test has not been fully verified, and the possible variability of material properties could negate the advantage of tests that rely on a single specimen. Balancing on both test efficiency and material variability, it appears that the most reasonable test procedure for determining Bodner-Partom model constants from tensile test data should be based on multiple specimens. The compromise between test efficiency and material variability also applies to the type of test data utilized in determining the model constants. For example, the additional use of creep or cyclic data to fine-tune the model constants should improve their predictive capability. On the other hand, the jump test could be a possible method for obtaining most or all the model constants if there are insufficient test specimens and can be a good test to examine predictive capability. In the next section, the use of the jump tests for determining the model constants for the alternate material, Mar-M247, will be demonstrated.

3.0 APPLICATION OF CONSTITUTIVE MODEL TO AN ALTERNATE MATERIAL (TASK L)

The application of the Bodner-Partom model to the alternate material, Mar-M247, was conducted in three phases. In Task L1, the minimum number of monotonic tensile, creep, and isothermal cyclic constitutive tests (both uniaxial and biaxial) was conducted to generate a data base for determining the model constants. Task L1 was completed this year; Task L2 and L3 are scheduled to be completed next year. In Task L2, three cyclic thermomechanical tests using the same test parameters that were employed in Task C for the base material will be performed. The applicability of the Bodner-Partom model shall be demonstrated for Mar-M247 in Task L3 by performing nonlinear analyses for the thermomechanical test cycles.

For these tasks, a total of twenty (20) Mar-M247 specimens were fabricated. Fourteen (14) specimens were used for isothermal tension, creep, and cyclic strain tests; three (3) specimens were used for isothermal biaxial tests and three (3) specimens were fabricated for the TMF tests.

3.1 Isothermal Tensile, Creep, and Cyclic Testing

Tensile tests for Mar-M247 were conducted using the approach developed in Task J. As indicated earlier in Section 2.0, the tensile test with strain rate jumps involved extending the specimen at an initial strain rate, $\dot{\varepsilon}_i$, to a prescribed 2% strain level (corresponding to the saturation stress level). After reaching the prescribed strain, four changes of strain rate were imposed as shown in Fig. 2.8. The tensile test matrix for Mar-M247 is shown in Table 3.1. In addition, isothermal cyclic and creep tests were performed for Mar-M247. As indicated in the test matrix, the cyclic tests were conducted at

TABLE 3.1

ISOTHERMAL TENSILE, CYCLIC AND CREEP TEST MATRICES FOR Mar-M247

	Temperatures, °C					
	23	648	760	871	982	1093
Mar-M247	X	X	X	X	X	X

$\dot{\varepsilon}_i = 1x10^{-4}$ sec^{-1}, $\dot{\varepsilon}_1 = 1x10^{-6}$ sec^{-1}, $\dot{\varepsilon}_2 = 1x10^{-5}$ sec^{-1}, $\dot{\varepsilon}_3 = 1x10^{-4}$ sec^{-1}, $\dot{\varepsilon}_4 = 1x10^{-3}$ sec^{-1}

CYCLIC TEST MATRIX FOR Mar-M247

Temperature, °C	$\dot{\varepsilon}_1$ sec^{-1}	$\Delta\varepsilon_1=\pm.25\%$	$\Delta\varepsilon_2=\pm.4\%$	$\Delta\varepsilon_3=\pm.6\%$
23	$5x10^{-4}$	X	X	X
648	$5x10^{-4}$	X	X	X
871	$5x10^{-4}$	X	X	X
982	$5x10^{-5}$	X	X	X
1093	$5x10^{-5}$	X	X	X

CREEP TEST MATRIX FOR Mar-M247

Temperature, °C	σ
871	600 MPa
982	300 MPa
1093	150 MPa

three strain range levels (0.25%, 0.4% and 0.6%) and at five temperatures (23, 648, 871, 982, and 1093°C). Only three creep tests were performed under conditions listed in Table 3.1.

The biaxial deformation behavior of Mar-M247 was interrogated using three nonproportional strain cycles. The first strain cycle was conducted at 648°C and contained the strain history sequence: (1) 90° out-of-phase combined tension-torsion, (2) in-phase combined tension-torsion, (3) fully-reversed torsion, and (4) fully-reversed tension. The strain sequence was conducted under strain-controlled condition and was repeated on the same specimen at two effective strain ranges (± .4% and ± .6%). The second nonproportional strain cycle was identical to the first one but was performed at 982°C. The third strain cycle was a combined tension-torsion cycle conducted under 90° out-of-phase condition with strain hold at each of the strain peaks. The test temperature was 982°C and the imposed effective strain range was ± 0.4%.

3.2 Determination of Bodner-Partom Model Constants

The procedures developed in Task J were used as the basis for determining the Bodner-Partom model constants for Mar-M247. As shown in Fig. 2.1, the first step in evaluating the model constants was to develop a set of work hardening rate (γ) versus stress (σ) plots from the experimental stress-strain data using the procedures described earlier. Typical γ-σ plots of Mar-M247 at 648 and 871°C are shown in Figs. 3.1 and 3.2, respectively. For temperatures below 871°C the γ-σ relations were essentially linear at both the low and the high stress regimes. The constants m_1 and m_2 could then be evaluated from the linear slopes of the γ-σ curve. For Mar-M247, m_2 was found to vary with temperature and its values were modified after comparing calculation

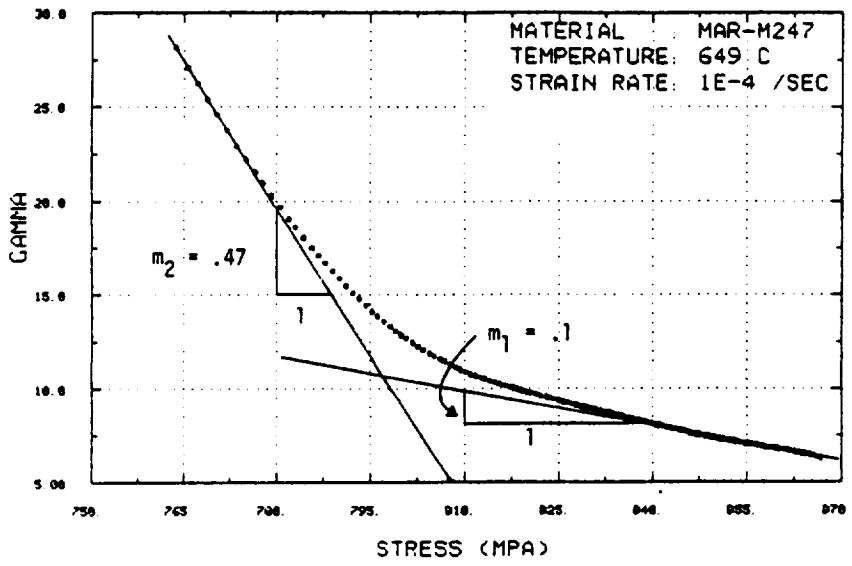

FIGURE 3.1 PLOT OF γ VS. σ INDICATING m_1 = .1 AND m_2 = .47 FOR Mar-M247 AT 649°C.

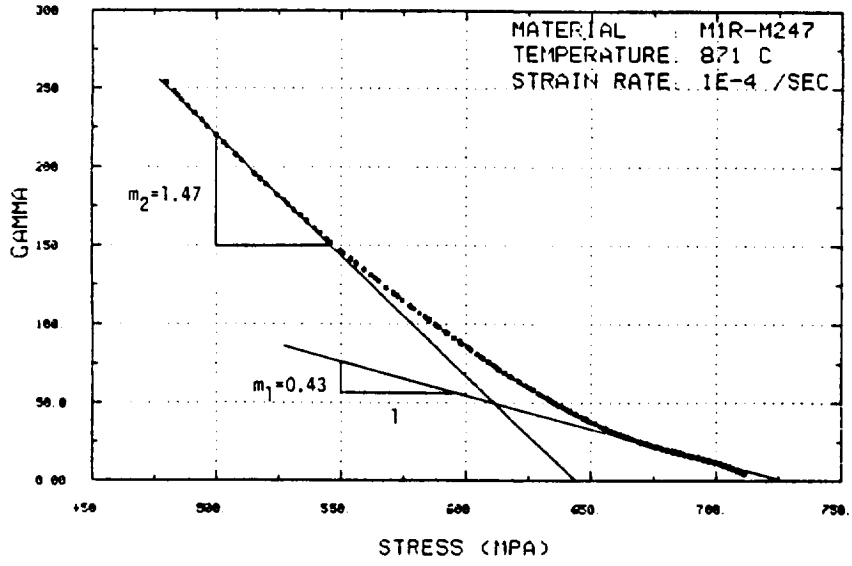

FIGURE 3.2 PLOT OF γ VS. σ INDICATING m_1 = .43 AND m_2 = 1.47 for Mar-M247 AT 871°C.

with experiment. Values of m_1 and m_2 for Mar-M247 obtained in this manner are shown in Table 3.2. These temperature dependent values were probably influenced by strain aging effects which are currently not included in the model.

The kinetic parameter n, which represents strain rate dependence of plastic flow in the Bodner-Partom model, was determined from the jump test that involves strain rate changes during the test. As discussed previously in Section 2.3, this particular procedure for evaluating n is based on assumptions, one of which is that the internal hardening variables remains essentially constant during an instantaneous strain rate change. The jump test data of Mar-M247 at 23, 648, 760, 871, 982, and 1093°C are presented in Figs. 3.3(a)-(f). In these tests, the specimens were initially pulled at a strain rate of 1×10^{-4} sec^{-1}. The strain rate was then subsequently changed to 10^{-6}, 10^{-5}, 10^{-4}, and 10^{-3} sec^{-1}. The results indicated that Mar-M247 was essentially rate insensitive at 23°C, but was rate sensitive at temperatures above 760°C. At 648°C, Mar-M247 showed negative strain rate sensitivity at 1×10^{-6} sec^{-1} and was rate insensitive at strain rates above 1×10^{-5} sec^{-1}.

The values of n for temperatures at 760 and 871°C were determined based on Eq. 2.8. The procedure used for determining the stress change consequent to a rapid strain rate change was based on the technique illustrated in Fig. 2.14. Only the n values determined for 760 and 871°C were based directly on test data [Fig. 3.4(a)]. Once the value of n was known, the sum of Z_1 and Z_3 was calculated using Eq. 2.7 and the saturation stress determined from the γ-σ plot. The n values at 982 and 1093°C were estimated from known values of Z_1 and Z_3 at 871°C assuming that Z_1 and Z_3 were temperature independent over this temperature range. The calculated n values were then slightly modified by fitting the model to the tensile stress-strain

TABLE 3.2

BODNER-PARTOM MODEL CONSTANTS FOR Mar-M247

Temperature - Independent Constants

$m_1 = .1\ MPa^{-1}$

$\alpha_1 = 0.0$

$Z_1 = 1.64 \times 10^4\ MPa$

$r_1 = r_2 = 3$

$D_o = 1 \times 10^4\ sec^{-1}$

Temperature - Dependent Constants

Constants	Temperature, °C					
	23	648	760	871	982	1093
n	.556	.556	.556	.522	.467	.415
m_2 (MPa^{-1})	1.35	.47	.47	1.35	1.35	1.35
Z_o (MPa)	1.6×10^4	1.6×10^4	1.6×10^4	1.3×10^4	1.2×10^4	1.05×10^4
Z_2 (MPa)	1.6×10^6	1.6×10^4	1.6×10^4	1.3×10^4	1.2×10^4	1.05×10^4
Z_3 (MPa)	5×10^3	5×10^3	8.63×10^3	8.63×10^3	8.63×10^3	8.63×10^3
$A_1 = A_2$ (sec^{-1})	0	0	0	2×10^{-2}	.25	2
E (MPa)	1.9×10^5	1.61×10^5	1.71×10^5	1.49×10^5	1.29×10^5	9.7×10^4

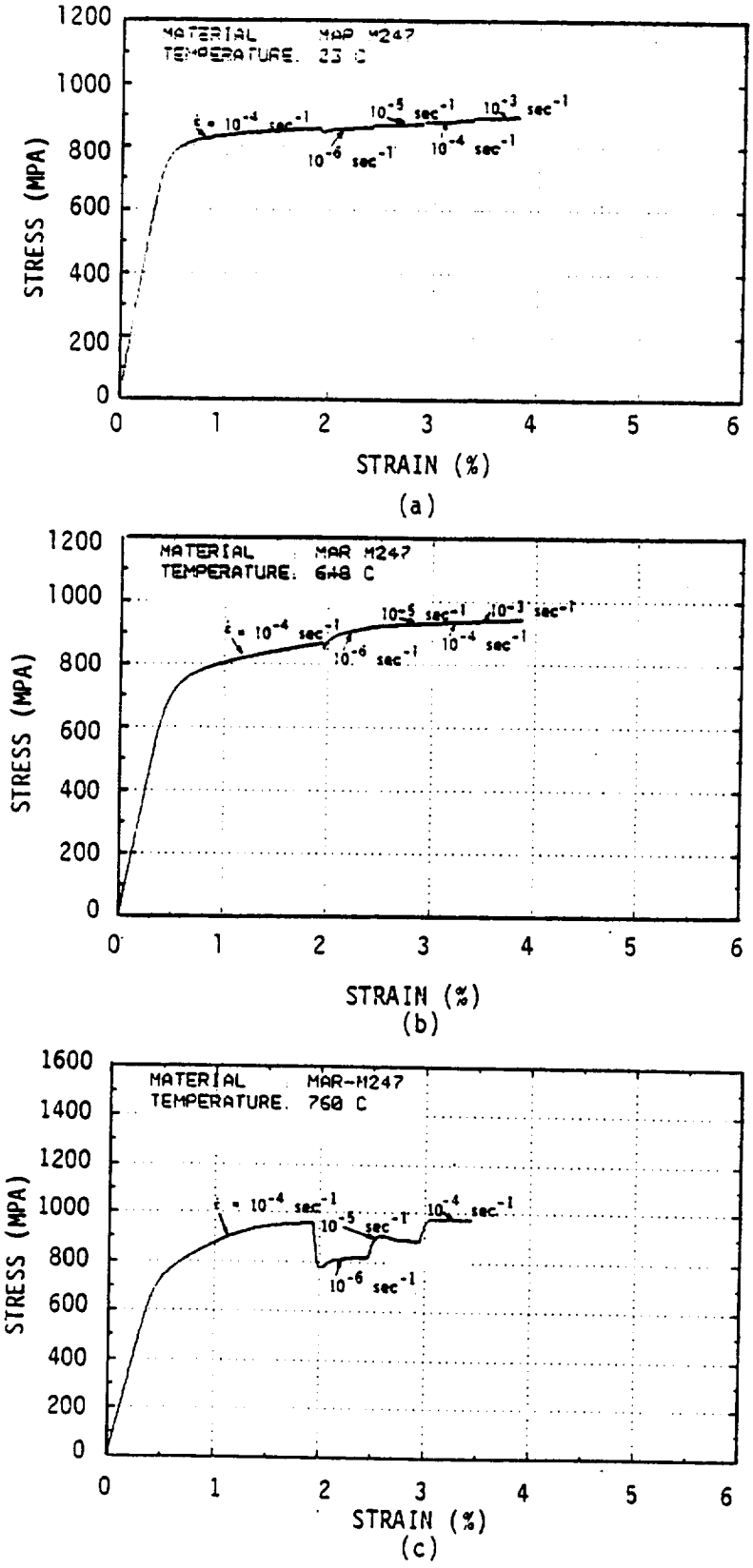

FIGURE 3.3 RESULTS OF "JUMP" TEST OF Mar-M247: (a) 23°C, (b) 648°C, AND (c) 760°C.

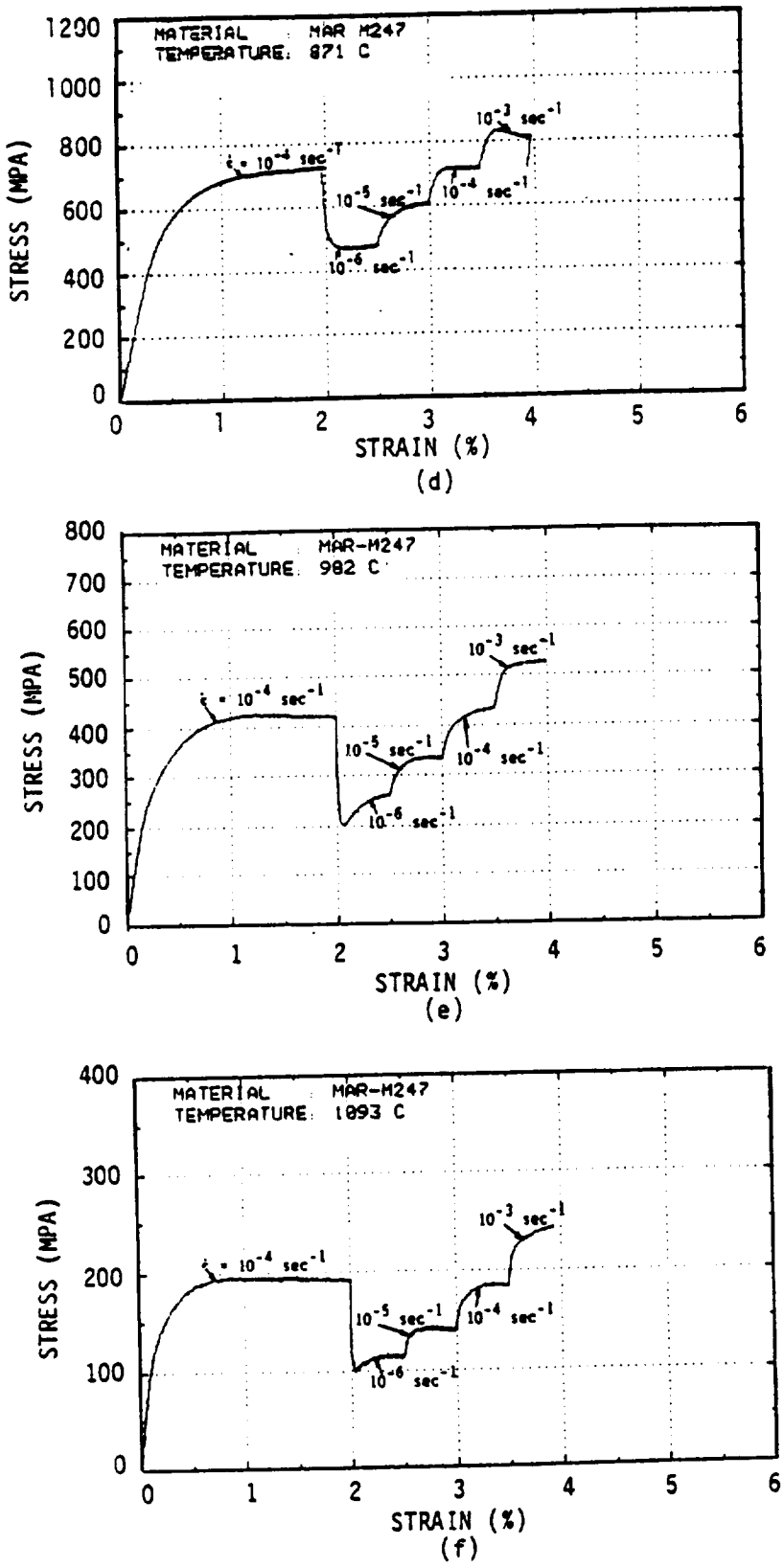

FIGURE 3.3 (Continued) RESULTS OF "JUMP" TEST OF Mar-M247: (d) 871°C, (e) 982°C, AND (f) 1093°C.

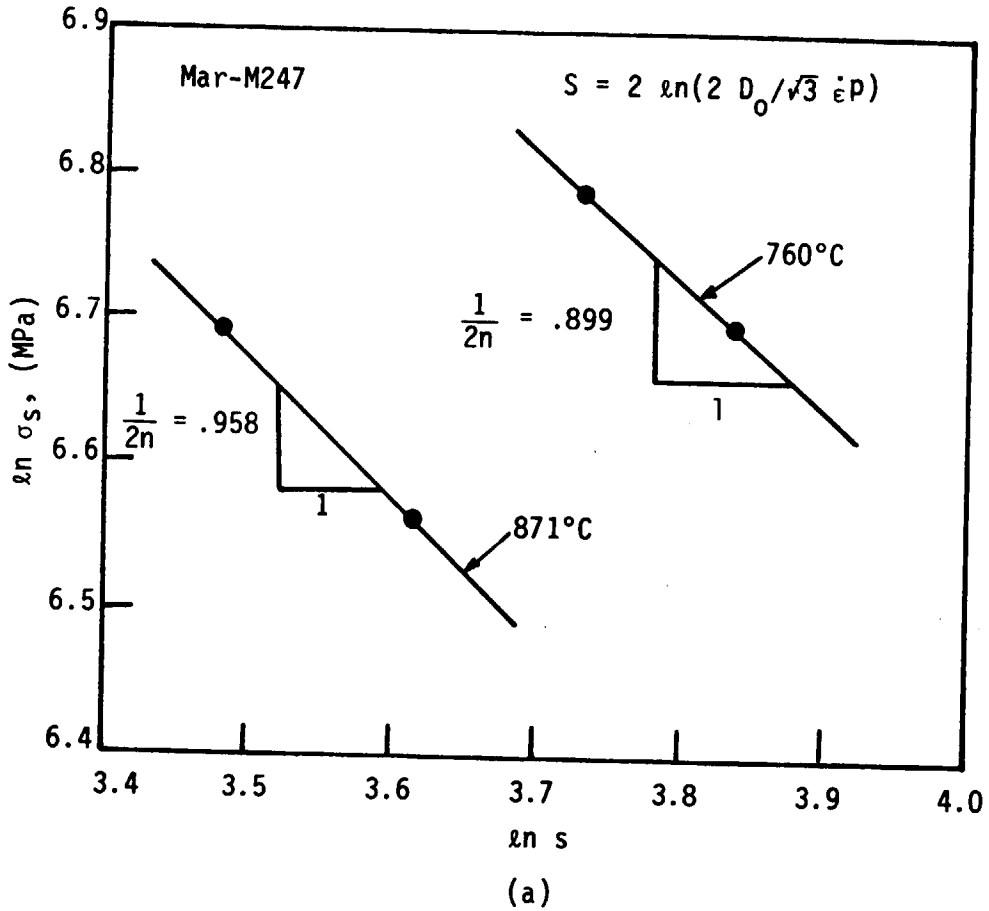

FIGURE 3.4 PLOT OF ℓn σ_s AGAINST ℓn s FOR OBTAINING n AT 760°C AND 871°C.

curves for $\dot{\varepsilon} = 1 \times 10^{-4}$ sec^{-1}. The apparent strain rate insensitivity of Mar-M247 at 23 and 648°C seems to be due to strain aging effects and precludes the use of these data for evaluating the values for n. The value of Z_3 could not be obtained at 23 and 648°C and it did not appear to be temperature independent at temperatures below 760°C. As a result, the n value for these temperatures were assumed to be identical to that for 760°C.

Using Eq. 2.11, Z_o was calculated based on the proportional limit. In the base program, the yield stress at .2% plastic strain offset was found to be adequate for computing Z_o for B1900+Hf. For Mar-M247, the proportional limit stress was found to give Z_o values which conformed better with the experimental stress-strain curves. The value of Z_2 was set to the value of Z_o, and the values of Z_1 and Z_3 were obtained by means of Eqs. 2.13 and 2.14, respectively.

The thermal recovery constants were determined from the steady state stress associated with a given strain rate in the jump test, as illustrated in Fig. 2.14. Again, r_2 was assumed to be equal to r_1 ($r_1=r_2=r$) and A_1 was also assumed to be equal to A_2 ($A_1=A_2=A$). The thermal recovery exponent was obtained by plotting versus $\sigma_c-\sigma_o$ in a log-log plot. From Fig. 3.4(b), r was determined to be 3 at 871, 982 and 1093°C. Once r was evaluated, the thermal recovery coefficient A was calculated from Eq. 2.19 based on the known values of q, r, and other model constants.

The procedure described above relied only on the tensile data to obtain all the model constants in the Bodner-Partom constitutive equations. Previous work in the base program, however, indicated that the recovery constant A obtained from tensile-creep data did not give good agreement with the cyclic data. As a result, creep and cyclic data were used, in addition to

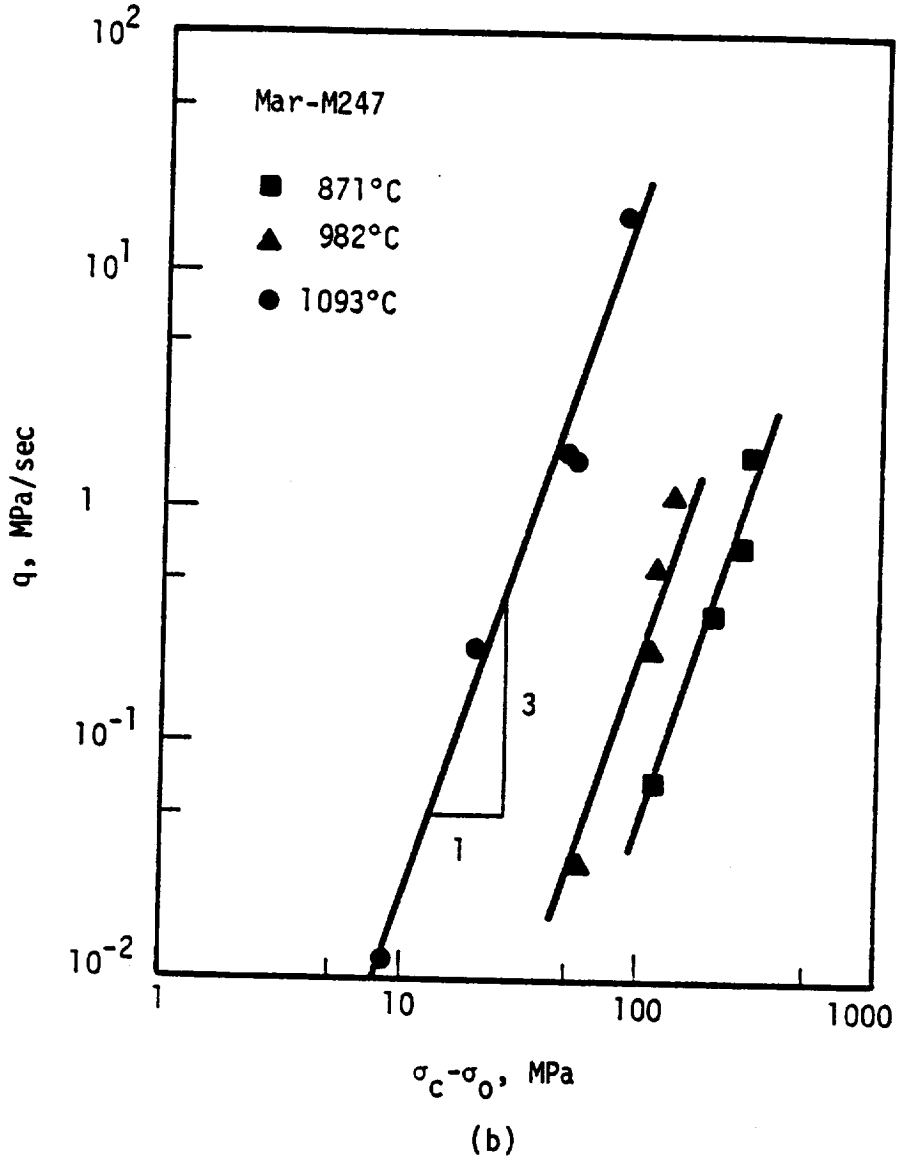

FIGURE 3.4 (Continued). PLOT OF q VS. $\sigma_c-\sigma_o$ SHOWING THE RECOVERY EXPONENT, r, BEING EQUAL 3 FOR Mar-M247 AT 571°C, 982°C, and 1093°C.

tensile data, to obtain the value of A by fitting the Bodner-Partom model to the experimental data. The A values obtained from these three different sets of data are consistent at 871°C but differ at 982 and 1093°C.

Table 3.2 summarizes the Bodner-Partom model constants for Mar-M247 which gives the best overall correlations with the experimental tensile, creep, and cyclic data. It should be noted that all of the model constants except the values for A listed in Table 3.2, were determined from the tensile data. The values of A for 871, 982 and 1093°C were determined based on the cyclic data. This set of A values was selected because it gave good correlation with both the tensile and cyclic data, though not with all of the creep data.

For applications involving nonproportional multiaxial loading paths, it is also necessary to evaluate the constant α_1 in the Bodner-Partom model which describes the amount of additional hardening due to nonproportional strain cycling. For Mar-M247, the value of α_1 was obtained from the nonproportional biaxial (tension-torsion) data corresponding to cycling under the strain history sequence: (1) 90° out-of-phase combined tension torsion, (2) in-phase combined tension-torsion, (3) fully reversed torsion, and (4) fully-reversed tension. The strain sequence was conducted under strain-controlled conditions at the effective strain ranges of 0.4% and 0.6% for each specimen. Figures 3.5(a) and (b) show the biaxial data for 648 and 982°C, respectively, which indicate that there is essentially no additional hardening associated with nonproportional strain cycling of Mar-M247 after the first cycle. The value of α_1 was therefore set to zero.

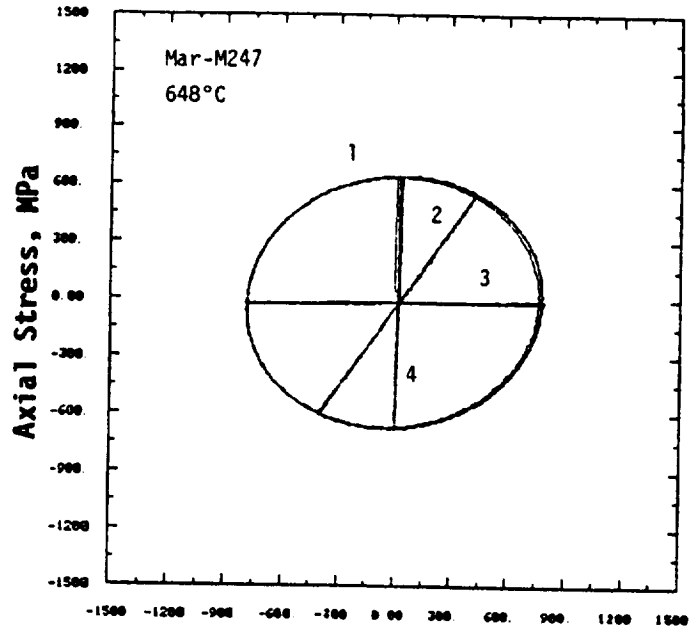

(a)

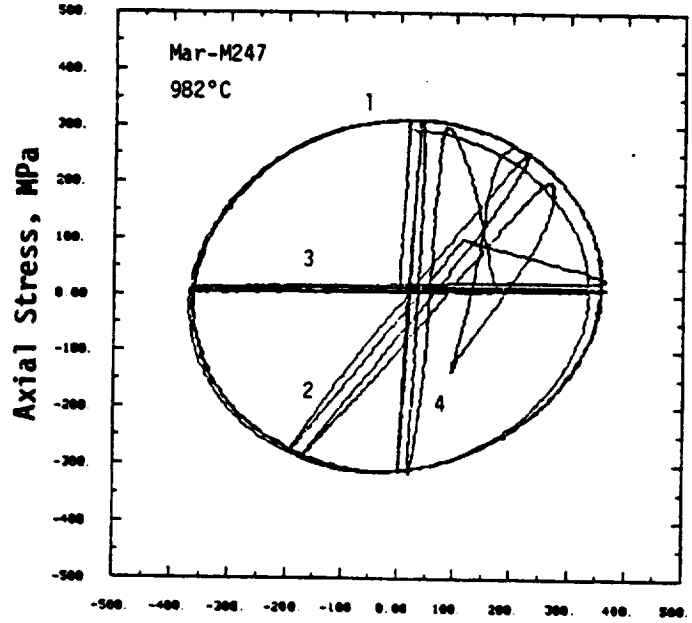

(b)

FIGURE 3.5 THE STRESS RESPONSE OF Mar-M247 TESTED UNDER: (1) 90° OUT-OF-PHASE TENSION-TORSION, (2) IN-PHASE TENSION-TORSION, (3) TORSION, AND (4) TENSION. The effective strain and strain rate are $\pm .47°$ and 4×10^{-1} sec^{-1}: (a) 648°C and (b) 982°C.

3.3 Correlation of Model and Experiment

Correlation of model and experimental tensile stress-strain curves for six test temperatures at $\dot{\varepsilon} = 1 \times 10^{-4}$ sec^{-1} are shown in Fig. 3.6. The unusual temperature behavior at the lower temperature appears to be due to strain aging effects which were directly incorporated in the hardening constants. This procedure is effective at a single strain rate but does not demonstrate the influence of strain aging on the applicable strain rate sensitivity. Figures 3.7(a), (b), (c), (d), (e), and (f) show comparisons of model calculation and experimental results of the stress-strain response under variable strain rate conditions at 23, 648, 760, 871, 982, and 1093°C, respectively. Comparison of model and experimental creep curves under an applied stress of 600 MPa at 871°C is presented in Figs. 3.8. The poor correlations of the predictions with the test results at 23 and 648°C are again due to strain aging effects which are currently not included in the model. For cyclic loading, the Bodner-Partom model predicts the stress range at a given imposed strain range reasonably well, but the calculated hysteresis loops are overly squared, as demonstrated in Figs. 3.9 and 3.10.

Correlations of model and experiment for biaxial loading under nonproportional 90° out-of-phase tension-torsion strain cycling at 648 and 982°C are shown in Figs. 3.11 and 3.12. The imposed effective strain range is ± 0.4%. As shown in Figs. 3.11, the σ-$\sqrt{3}\tau$ loci at 649°C are predicted by the model but individual hysteresis loops are larger than those experimentally observed. The results for 982°C, shown in Figs. 3.12, indicate that the model tends to overpredict the stress range in tension/compression and the width of the corresponding hysteresis loop. A comparison of model prediction and experimental data for 90° out-of-phase tension-torsion strain cycling with strain hold at each of the strain peaks is shown in Fig. 3.13. In this case, the model also overpredicts the tension/compression stress range and the width of the associated hysteresis loop.

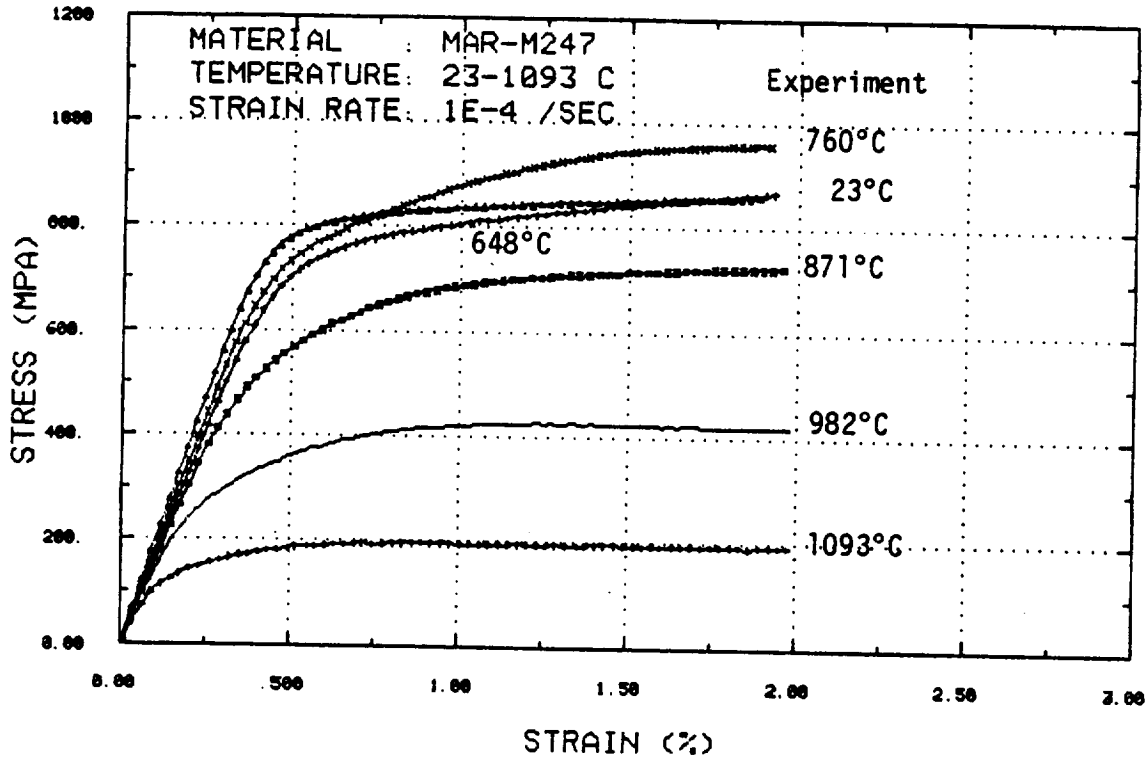

(a)

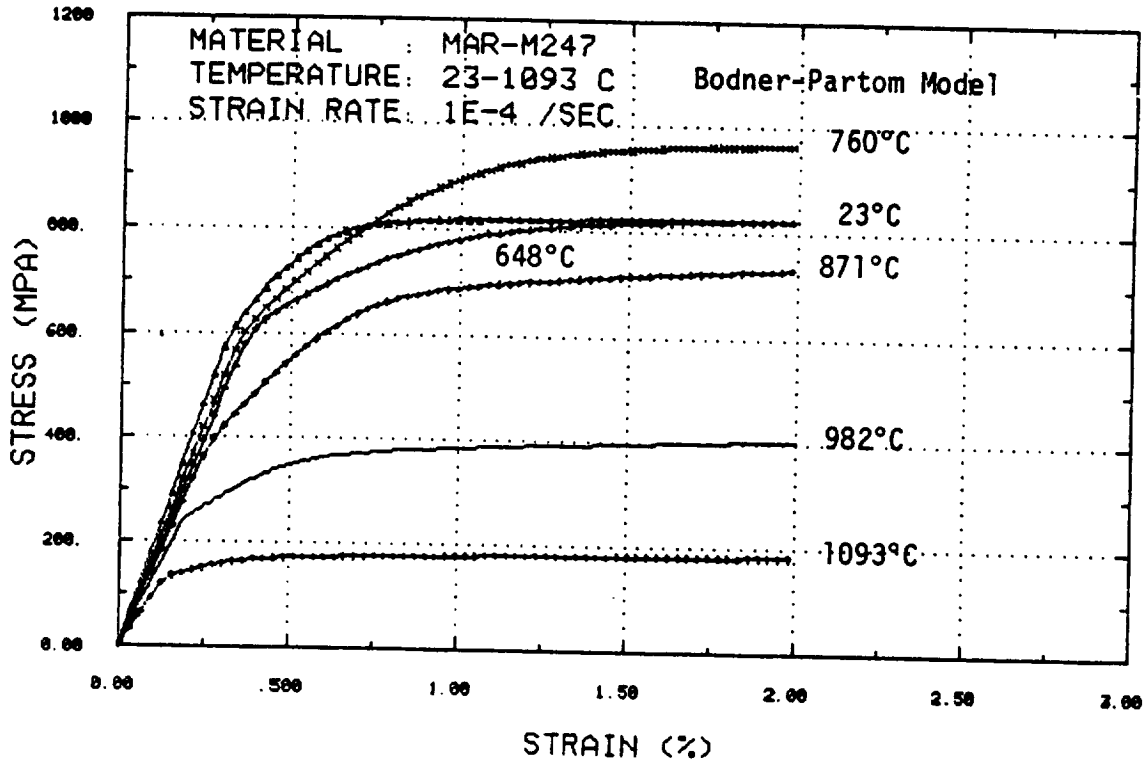

(b)

FIGURE 3.6 CORRELATION OF THE BODNER-PARTOM MODEL WITH EXPERIMENTAL TENSILE CURVES AT SIX TEMPERATURES: (a) EXPERIMENT, AND (b) MODEL CALCULATIONS.

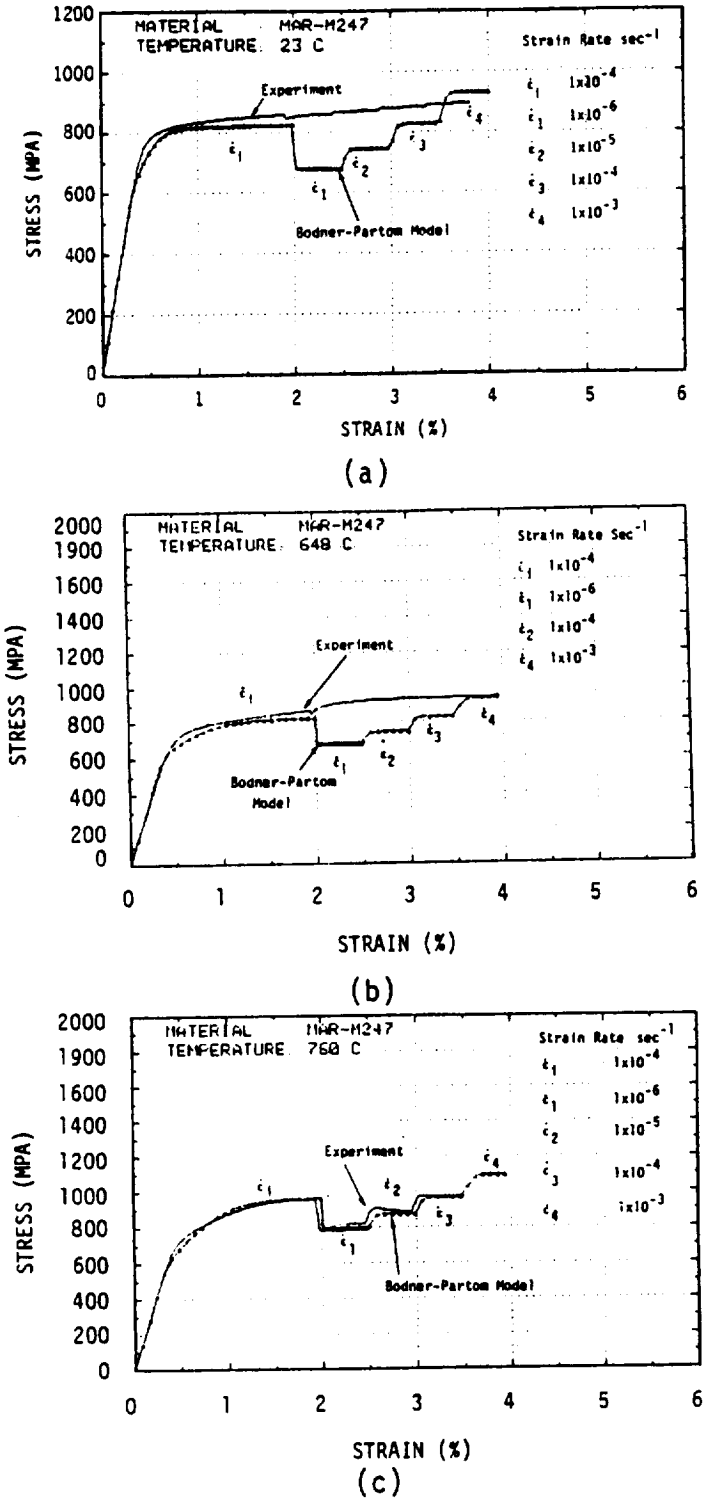

FIGURE 3.7 COMPARISONS OF MODEL CALCULATION AND EXPERIMENT FOR TENSILE TEST WITH STRAIN RATE CHANGES: (a) 23°C, (b) 648°C, and (c) 760°C.

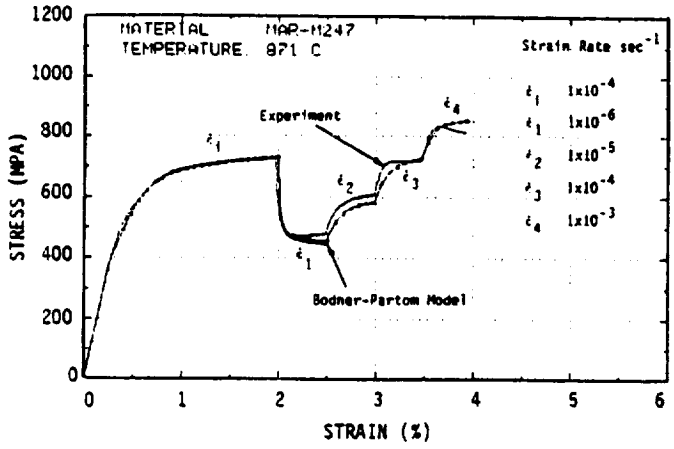

(d)

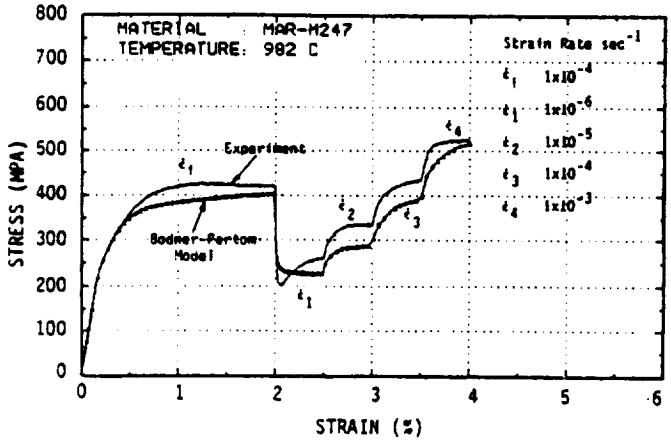

(e)

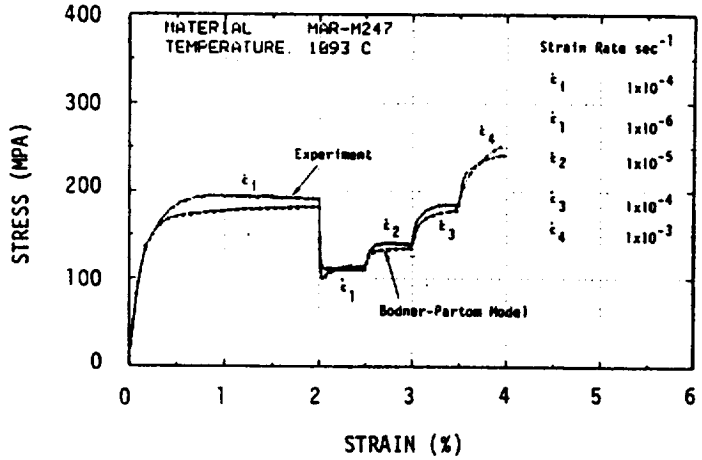

(f)

FIGURE 3.7 (Continued) COMPARISONS OF MODEL CALCULATION AND EXPERIMENT FOR TENSILE TEST WITH STRAIN RATE CHANGES: (d) 871°C, (e) 982°C, and (f) 1093°C.

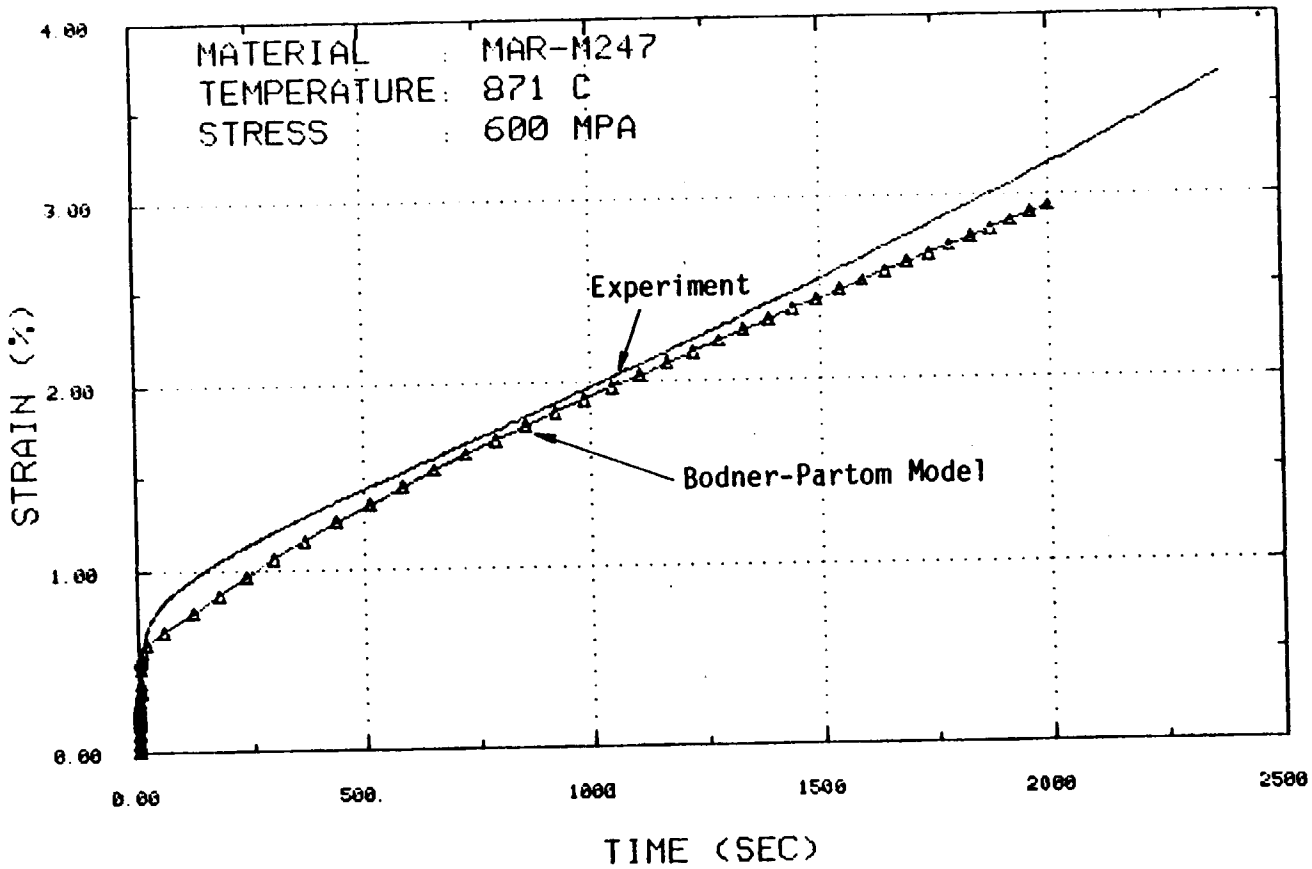

FIGURE 3.8 CREEP CURVE OF Mar-M247 AT 871°C UNDER AN APPLIED STRESS OF 600 MPa.

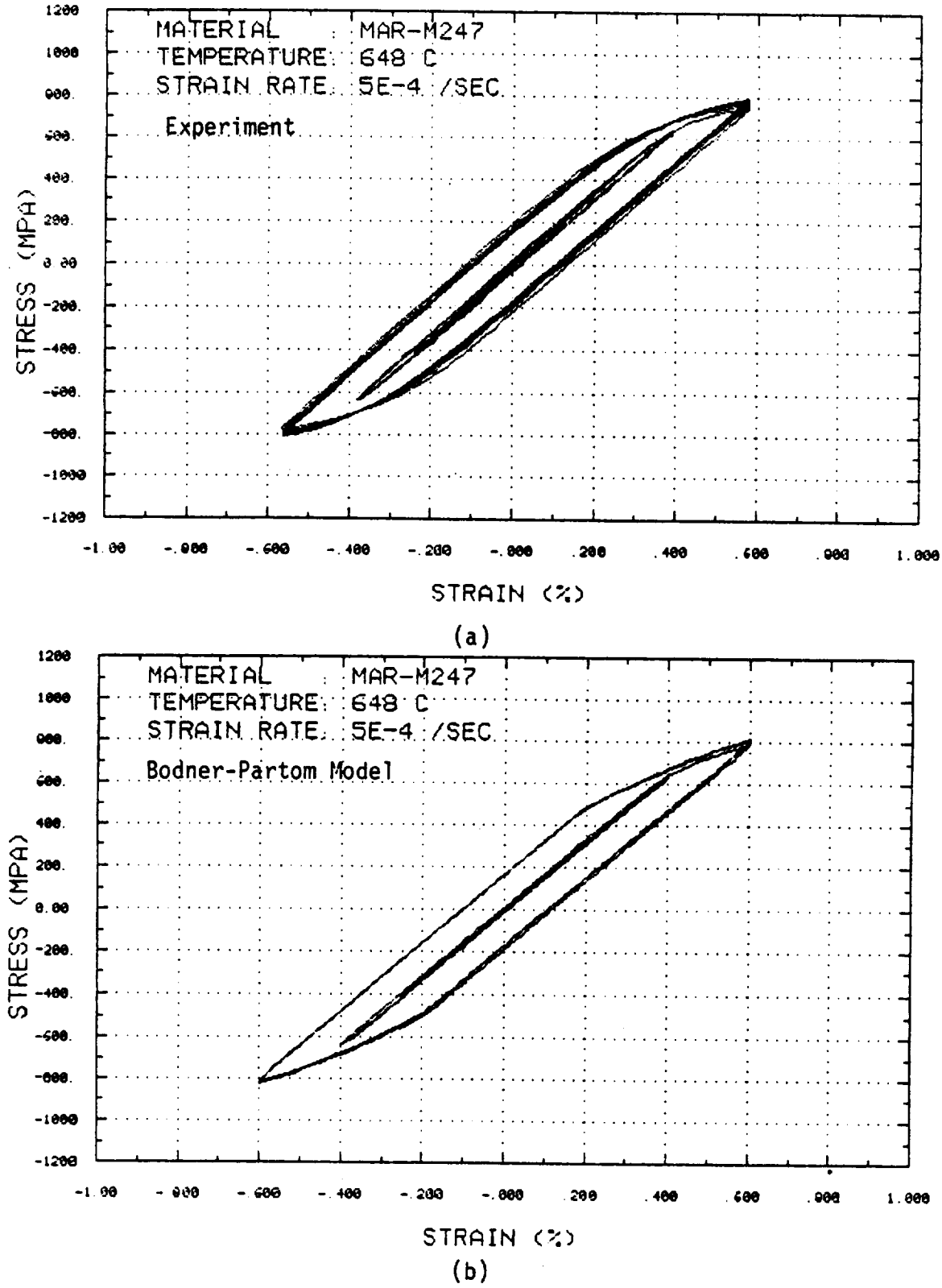

FIGURE 3.9 COMPARISON OF MODEL CALCULATION AND EXPERIMENTAL CYCLIC DATA AT 648°C. The cyclic test was conducted under fully-reversed condition at strain ranges of ±.25%, ±.4%, and ±.6%: (a) experiment, and (b) Bodner-Partom Model.

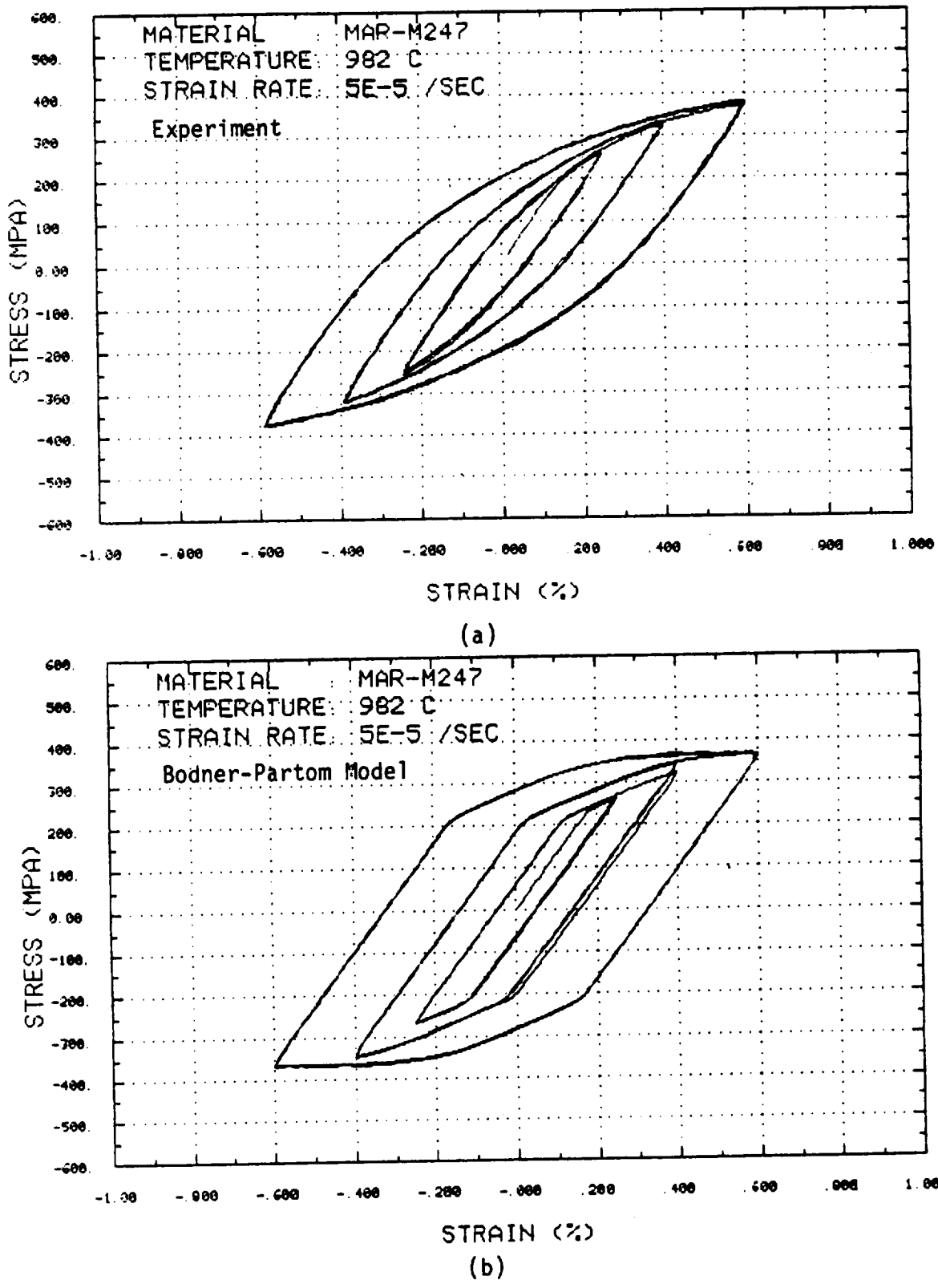

FIGURE 3.10 COMPARISON OF MODEL CALCULATION AND EXPERIMENTAL CYCLIC DATA AT 982°C. The cyclic test was conducted under fully-reversed condition at strain ranges of ±.25%, ±.4%, and ±.6%: (a) experiment, and (b) Bodner-Partom Model.

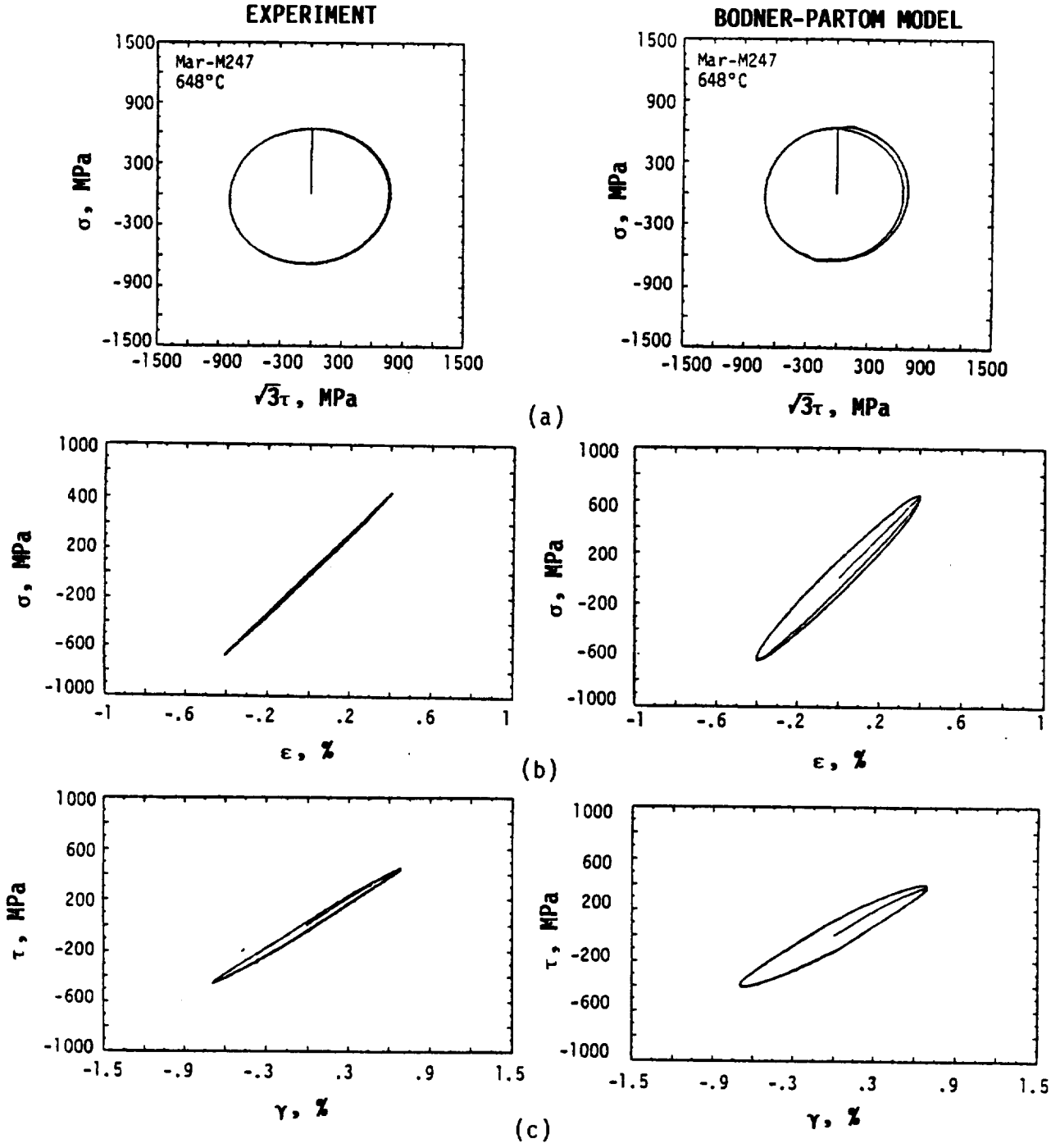

FIGURE 3.11 COMPARISON OF MODEL CALCULATION AND EXPERIMENT FOR Mar-M247 UNDER 90° OUT-OF-PHASE STRAIN CYCLING AT 648°C. The effective strain and strain rate are +.4% and 4×10^{-4} sec^{-1}: (a) σ-τ plot, (b) σ-ε plot, and (c) τ-γ plot.

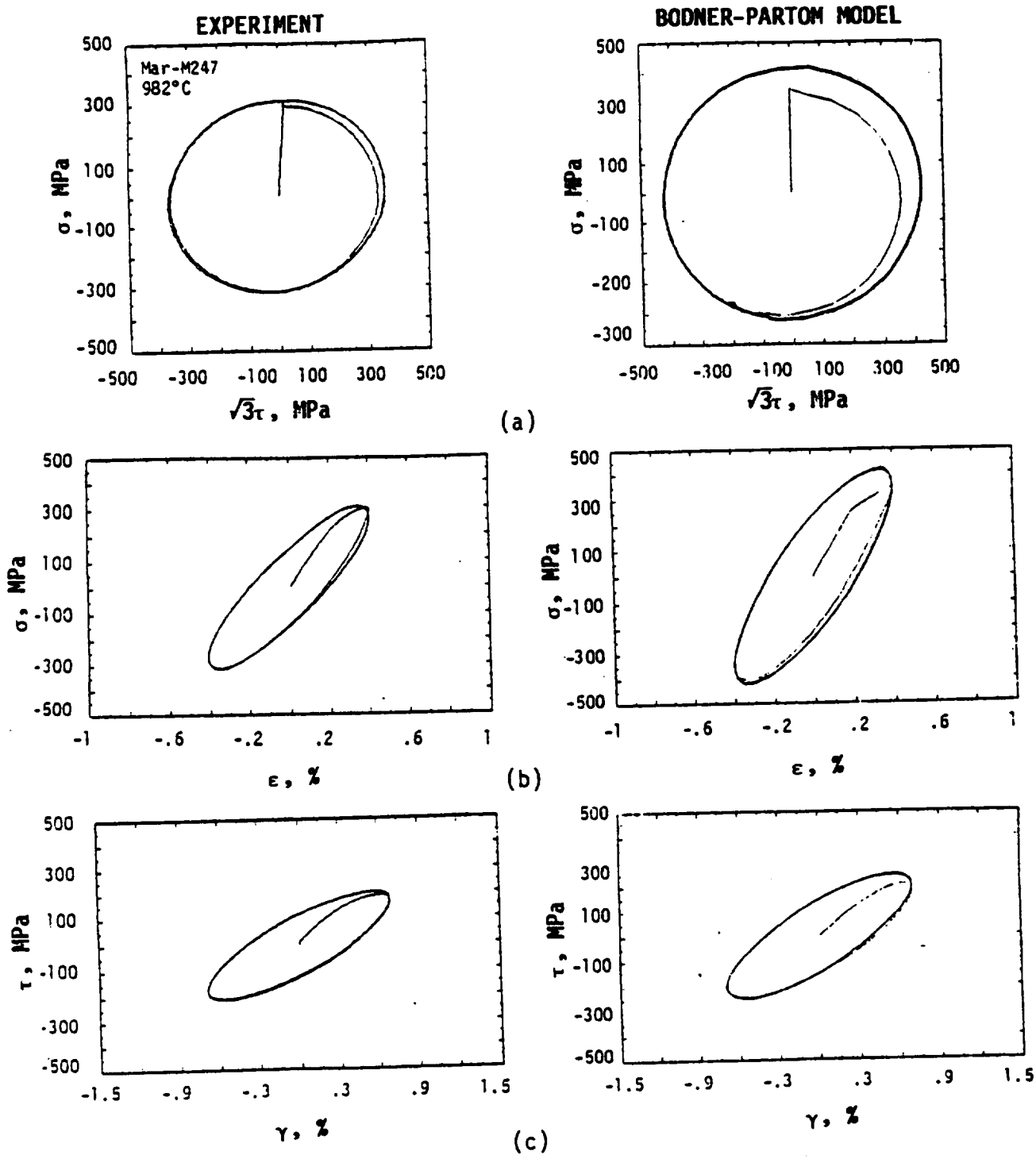

FIGURE 3.12 COMPARISON OF MODEL CALCULATION AND EXPERIMENT FOR Mar-M247 UNDER 90° OUT-OF-PHASE STRAIN CYCLING AT 982°C. The effective strain and strain rate are $\pm$ .4% and 4×10^{-4} sec^{-1}: (a) σ-τ plot, (b) σ-ε plot and (c) τ-γ plot.

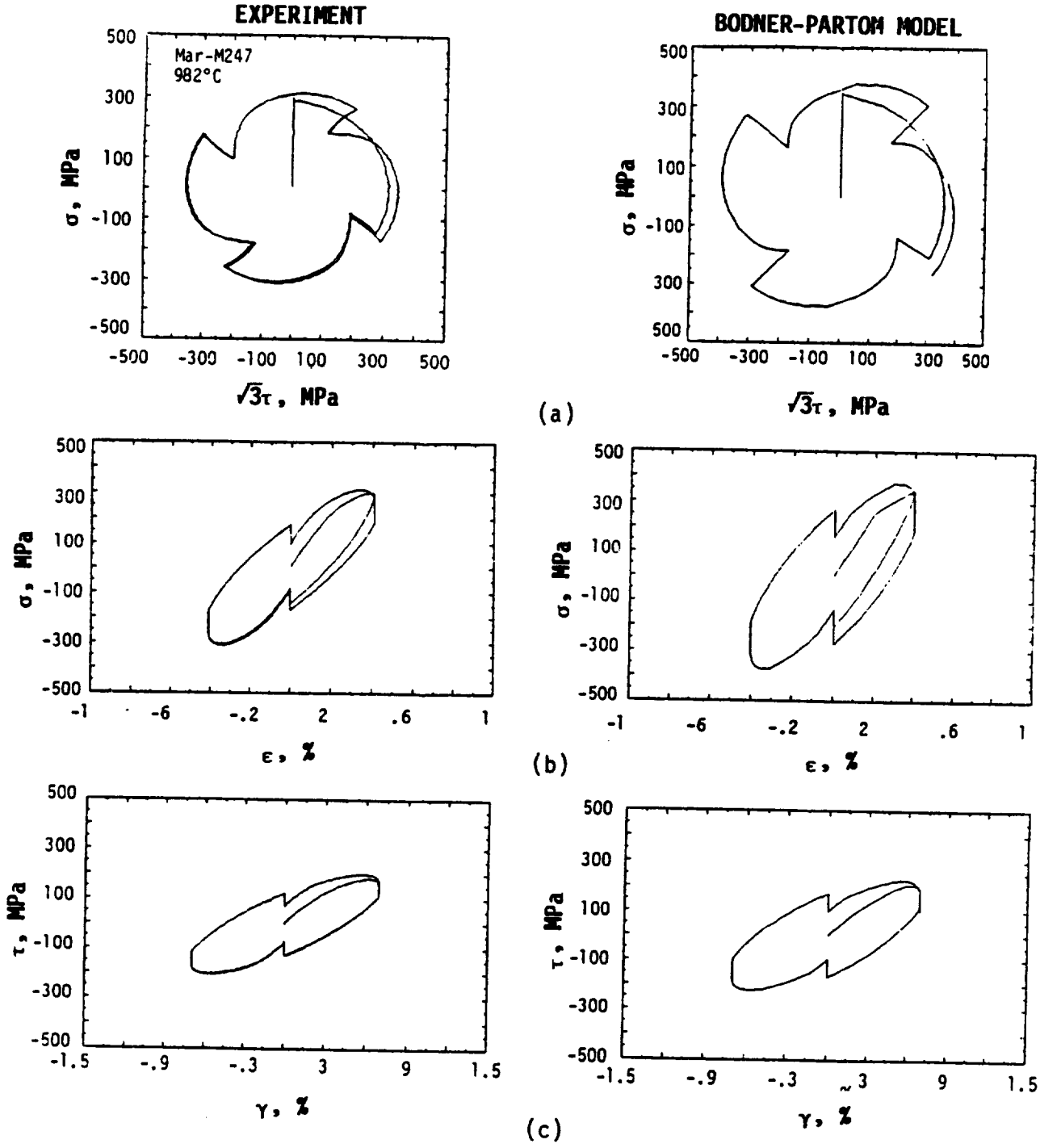

FIGURE 3.13 COMPARISON OF MODEL CALCULATION AND EXPERIMENT FOR Mar-M247 UNDER 90° OUT-OF-PHASE STRAIN CYCLING AT 982°C WITH STRAIN HOLD AT EACH OF THE STRAIN PEAKS. The effective strain and strain rate are $\pm 4 \times 10^{-4}$ sec^{-1}: (a) σ-τ plot (b) σ-ε plot and (c) τ-γ plot.

4.0 FINAL DEVELOPMENT OF THE CONSTITUTIVE MODEL (TASK K)

4.1 Thermal History Effects - Literature Survey

A literature survey was conducted as part of Task K1 to assess the effects of thermal history on constitutive behavior and their implications with regard to constitutive modeling based on the unified approach. The literature survey indicates that inelastic response of metals [7,8,9] including yield surfaces [10], depends not only on temperature but also on thermal history. This is analogous to the well-established fact that inelastic deformation depends on the current stress as well as the deformation history. In many instances, different hardening response is observed in materials under isothermal and nonisothermal conditions and the different hardening behavior has generally been attributed to either strain aging [8,9] or microstructural effects [7].

Thermal history effects are usually modeled in the unified constitutive approach by including thermal terms in the evolution equations for the isotropic and directional hardening variables [11,12]. The general forms of the evolution equations for the isotropic hardening variable, K, and the directional hardening variable, Ω_{ij}, are as follows [11]:

$$\dot{K} = h_1(K)\dot{M}_1 - r_1(T,K) + \theta_1(K,T)\dot{T} \tag{4.1}$$

$$\dot{\Omega}_{ij} = h_2(\Omega_{ij})\dot{M}_{ij} - d(\Omega_{ij},T)\dot{N}_{ij} - r_2(\Omega_{ij},T)V_{ij} + \theta_2(\Omega_{ij},\dot{T})T\, W_{ij} \tag{4.2}$$

where h_1, r_1, and θ_1 represent, respectively, the hardening, static thermal recovery, and thermal history functions for K; h_2, d, r_2, and θ_2 represent the hardening, dynamic recovery, static thermal recovery, and thermal history

functions for Ω_{ij}, respectively; $\dot{M}_{ij}$ and $\dot{N}_{ij}$ are the hardening measure; V_{ij} and W_{ij} are directional indices. Specific forms of $\dot{M}_{ij}$, $\dot{N}_{ij}$, V_{ij}, and W_{ij} are given in [11].

The appropriate forms of θ_1 and θ_2 are not well established at this time. A general approach for modeling thermal history effects is to express θ_1 and θ_2 as functions of the internal variable and temperature [11,12]. New internal variables may also be introduced [7]. In a particular approach [2,5], θ_1 and θ_2 are assumed to depend on temperature only and are taken as functions represented by the variation of the material constants with temperature [2,5], i.e.,

$$\theta_1(T) = \frac{\partial C_i(T)}{\partial T} \tag{4.3}$$

$$\theta_2(T) = \frac{\partial C_i'(T)}{\partial T} \tag{4.4}$$

where C_i and C_i' are temperature-dependent material constants based on isothermal data. Temperature-dependent material constants in the kinetic equation are treated in a similar manner. Comparisons of thermomechanical constitutive data of B1900+Hf and calculations using the Bodner-Partom and Walker Models at SwRI and PW&A indicated that the approach based on Eq. 4.3 and 4.4 led to reasonably good agreement between theory and experiment [2], suggesting that thermal history effects associated with TMF cycling can be predicted based on isothermal data alone. Whether or not this conclusion is valid for other materials or thermal paths remains an open question.

Recent thermomechanical studies [8,9] report response charactertics under nonisothermal conditions which are substantially different from those manifested under isothermal circumstances. While these studies clearly

demonstrate the presence of strain aging and thermal history effects on the behavior of a number of structural alloys, the results do not prove that thermal history effects cannot be predicted by an appropriate constitutive model which uses material constants based on isothermal data. A systematic evaluation of model prediction against experimental results obtained under a variety of thermomechanical paths is required to resolve this issue.

Based on the results of this literature survey, SwRI recommends that efforts in Task K2 be directed to examining thermal history effects in B1900+Hf by thermomechanical cycling: (1) at a temperature range where strain aging effect is prominent, (2) at a temperature range where microstructure changes such as precipitation and/or resolution of precipitates might occur, (3) under various heating rates, (4) using different thermal paths, and (5) using elastic as well as inelastic loading paths. The experimental efforts will be coupled with parallel analytical efforts to determine whether or not thermal history effects can be predicted using the Bodner-Partom model in conjunction with material constants obtained solely from isothermal data.

4.2 Modifications of the Bodner-Partom Model

4.2.1. Strain Aging Effects

Extensive testing in both the base and the optional program indicated that strain aging effects are present in Mar-M247 in the temperature range of 23-648°C, and also exist for the B1900+Hf material in a temperature range bounded above by about 760°C. Under this circumstances, certain predictions of the Bodner-Partom model do not correlate well with the experimental data because strain aging effects are not included in the model. It is apparent that the strain aging effect should be incorporated into the Bodner-Partom

model in order to improve the accuracy of the model in the regime of influence.

Strain aging effects are primarily due to the interaction of dislocations and solute atoms with moving dislocations [13,14,15]. Common observations associated with strain aging are: (1) serrated flow; (2) negative strain rate sensitivity; (3) a plateau in the temperature dependence of the yield stress. In a review paper, Schmidt and Miller [14] indicated that solute enhanced strain hardening can be due to a number of processes, including precipitation and solute affecting the rate of dislocation multiplication, annihilation or the recovery of dislocation structures. As indicated earlier, strain aging and precipitation have also been linked to thermal history effects [7-9].

Schmidt and Miller [16] have incorporated a strain aging term into the unified constitutive equations of Miller [17] by introducing a function which is added to the isotropic hardening variables. The functional form proposed by Schmidt and Miller to represent solute strengthening is:

$$F(\text{solute hardening}) = a_o \exp\left[-a_1 \log(\dot{\varepsilon}/\dot{\varepsilon}_o)^2\right] \qquad (4.5)$$

where a_o, and a_1 are constants; $\dot{\varepsilon}$ and $\dot{\varepsilon}_o$ are the applied and reference effective strain rates. It is noted that this procedure is an empirical method for representing the effect of strain aging and does not correspond directly with physical processes. This functional relationship was adopted in the Walker model for incorporating strain aging effects [2]. Walker, however, considered solute hardening to be directional in character and the strain aging effects were incorporated in the evolution equation for the equilibrium stress [2]. A possible way of modifying the Bodner-Partom model to include

strain aging effects would be to adopt Eq. (45) into the evolution equation for the direction hardening variable, β_{ij}, so that

$$\dot{\beta}_{ij} = m_2[Z_3 U_{ij} - \beta_{ij} (1-a)] \dot{W}_p - \text{thermal recovery term} \qquad (4.6)$$

where a represents the strain aging term given by Equation 4.5. The constants a_o, a_1, and $\dot{\varepsilon}_o$ must be evaluated from tensile data in the strain aging regime. Other formulations of strain aging and the effect of thermal history on Eq. 4.6 also need to be examined pending the results of the thermomechanical cyclic tests.

4.2.2 Nonproportional Hardening

As discussed in Section 3.3, the Bodner-Partom model somewhat overpredicts the stress response of Mar-M247 subjected to 90° out-of-phase tension-torsion strain cycling. Similar results were also observed in the calculations for B1900+Hf [2]. In order to examine this effect, exercises were performed using the Bodner-Partom model and the constants for Mar-M247 at 982°C: (1) uniaxial strain cycling under an axial strain range of ± .4% for 5 cycles; (2) 90° out-of-phase tension-torsion for two and a half cycles at an effective strain range of ± .4%; (3) return to axial loading as described in (1). The calculated σ-$\sqrt{3}\tau$ responses associated this strain sequence is shown in Figure 4.1. Note that cyclic saturation is almost attained after uniaxial cycling for 5 cycles. Additional cyclic hardening, however, is observed when the 90° out-of-phase cycle is applied. This nonproportional hardening saturated rapidly and the σ-$\sqrt{\tau}$ locus becomes stable in the second cycle. Examination of the internal variables reveals that the nonproportional hardening is the consequence of an increase of the directional hardening

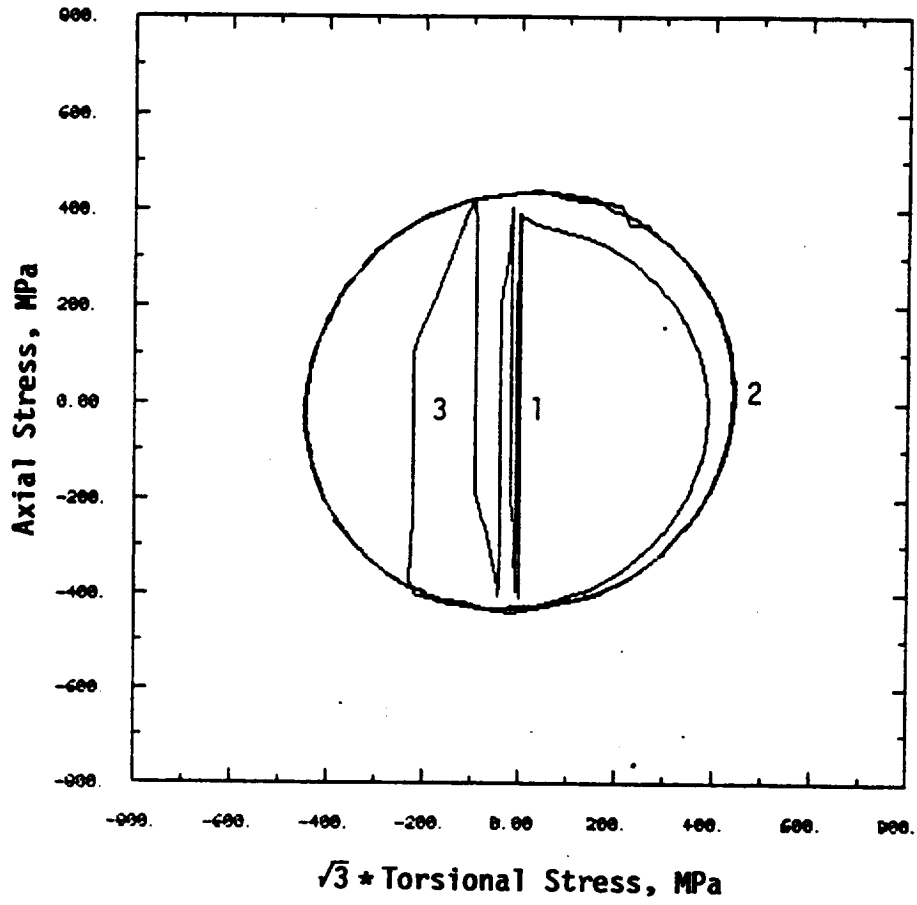

FIGURE 4.1 BODNER-PARTOM MODEL CALCULATION FOR MAR-M247 UNDER:
(1) UNIAXIAL CYCLING FOR 5 CYCLES, FOLLOWED BY
(2) 90° OUT-OF-PHASE CYCLING FOR 2 1/2 CYCLES, AND
(3) UNIAXIAL CYCLING FOR 5 CYCLES.

variable, Z^D, when the loading condition is changed from uniaxial to out-of-phase loading, Figure 4.2. This nonproportional hardening is transient and diminishes as the loading condition is returned to uniaxial loading. The corresponding histories for the directional hardening variable tensor, β_{ij}, are shown in Figure 4.3.

An explanation for this transient nonproportional hardening is that the conditions for cyclic saturation under uniaxial loading and nonproportional, multiaxial loading are different. From Figure 4.3, it appears that

$$Z^D = \beta_{ij} u_{ij} = \text{constant} \tag{4.7}$$

during cyclic saturation under a 90° out-of-phase strain cycle. As a result,

$$\dot{Z}^D = \beta_{ij} \dot{u}_{ij} + \dot{\beta}_{ij} u_{ij} = 0 \tag{4.8}$$

$$\dot{Z}^I = 0 \tag{4.9}$$

would be the conditions for cyclic saturation under nonproportional loading. On the other hand, the condition for cyclic saturation under uniaxial straining is $\dot{Z}^I = 0$ only.

This type of nonproportional hardening effect appears to be present in B1900+Hf and Mar-M247 (see Figs. 3.15-3.16). The effect, however, is quite small and becomes saturated within one cycle. The overprediction of the axial stress by the Bodner-Partom model for 90° out-of-phase loading appears to be primarily due to overestimation of this transient, nonproportional hardening effect. Additional efforts need to be directed in the future toward clarifying this aspect of the model.

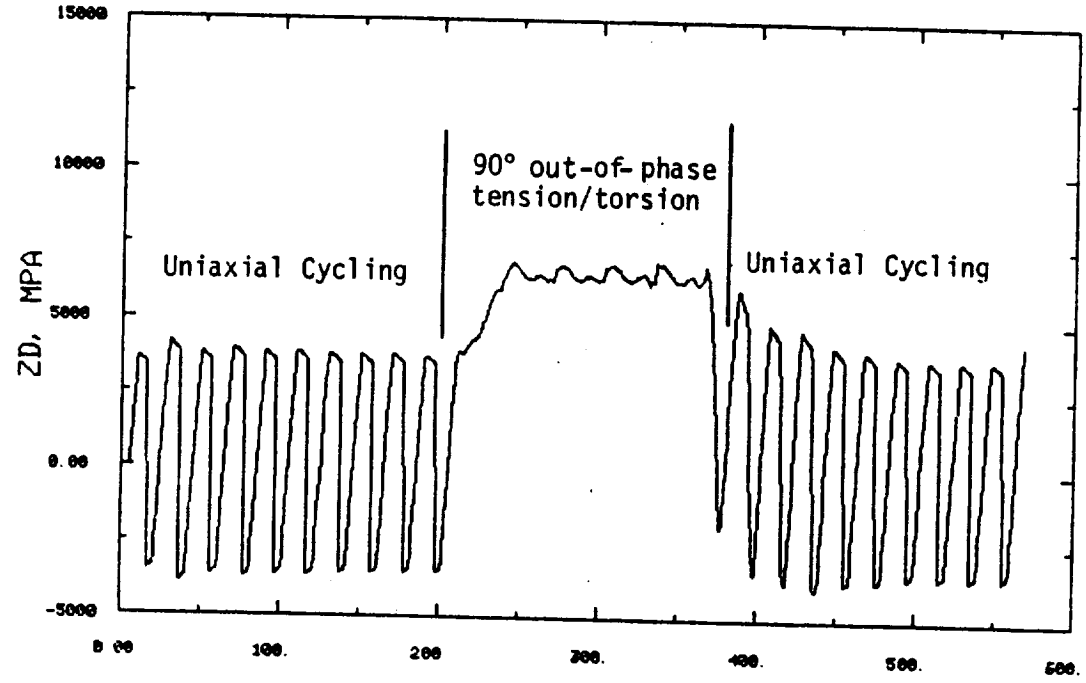

(a)

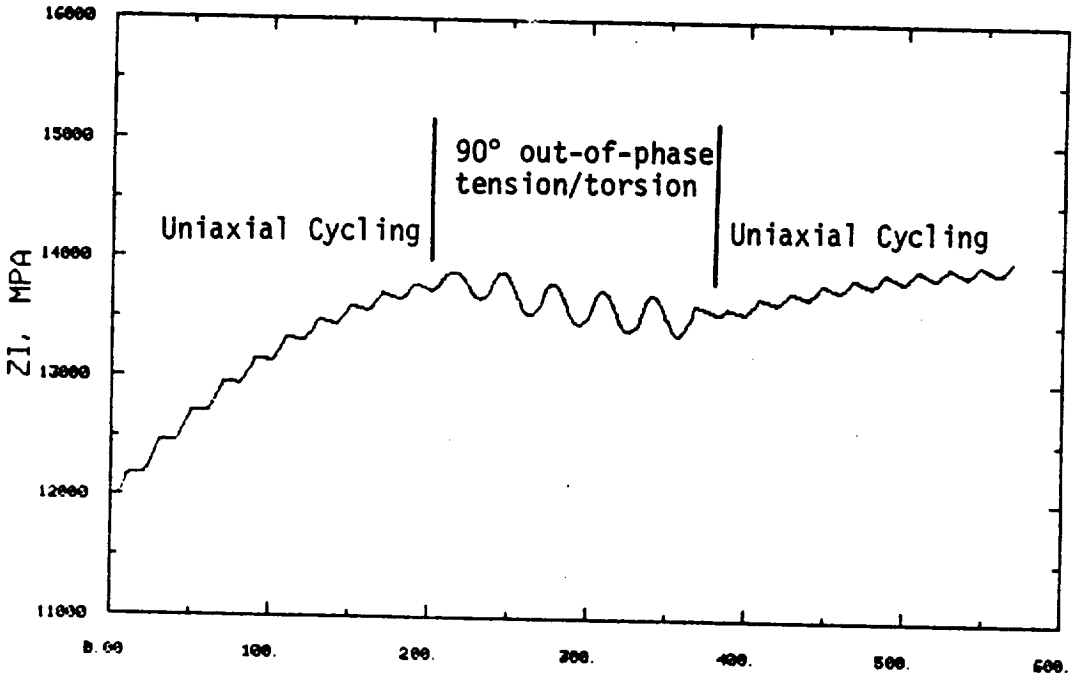

(b)

FIGURE 4.2 HISTORIES OF HARDENING VARIABLES FOR THE STRAIN CYCLE DESCRIBED IN FIGURE 4.1: (a) DIRECTIONAL HARDENING VARIABLE, Z^D, AND (b) ISOTROPIC HARDENING VARIABLE, Z^I.

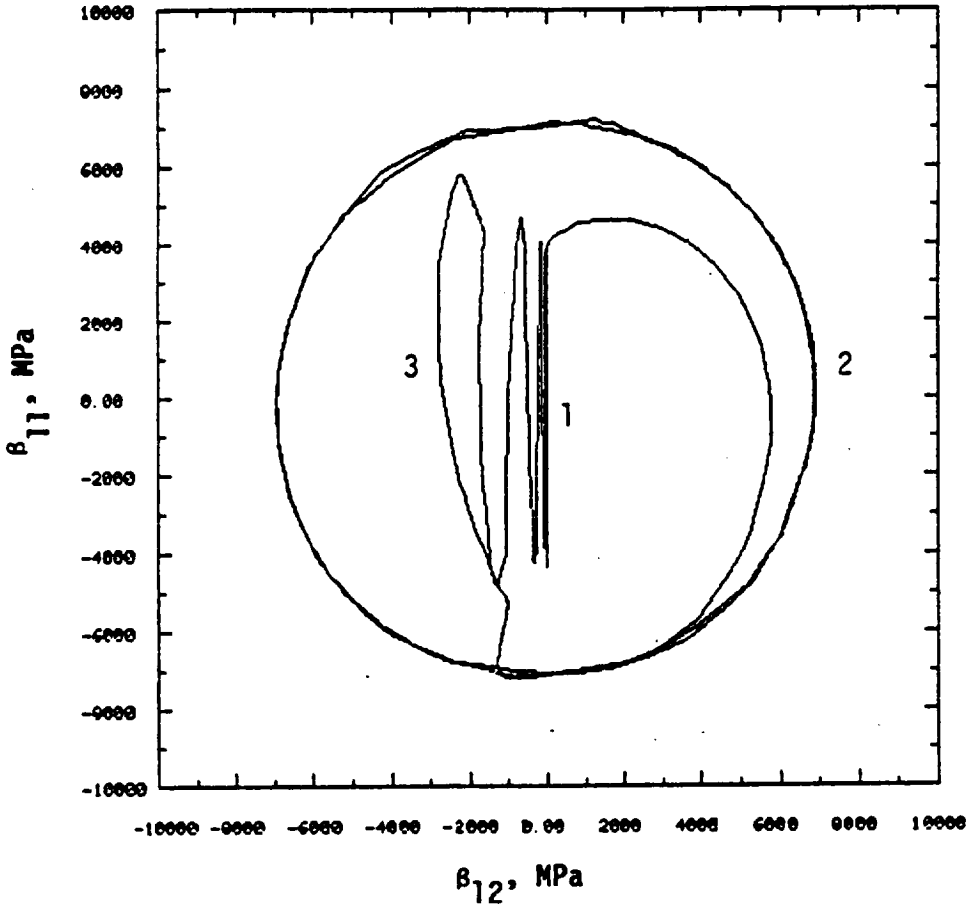

FIGURE 4.3 HISTORIES OF THE DIRECTIONAL HARDENING TENSOR FOR THE STRAIN CYCLE DESCRIBED IN FIGURE 4.1.

5.0 HOT SECTION COMPONENT ANALYSIS

5.1 Demonstration of the Walker Constitutive Model for an Airfoil

The analysis described in the following report was conducted as part of Task G. The material model demonstrated is the Walker viscoplastic formulation [5,18] with the the improved efficiency integration scheme developed by Cassenti [19]. This is one of two analytic models developed under this contract [2].

5.1.1 Component Finite Element Analysis Model Description

The component chosen for the demonstration of the B1900+Hf viscoplastic model is the airfoil portion of a typical cooled turbine blade. The foil was analyzed using the MARC [20] finite element program. Figure 5.1 shows the finite element mesh used in the analysis. A total of 173 elements and 418 nodes were used to describe the geometry, resulting in 1086 degrees of freedom. Two element types were used in the mesh. The bulk of the airfoil was modeled using 8 node solid elements (MARC element type 7), but a portion of the leading edge was modeled with higher order 20 node solid elements (MARC element type 21). A total of twenty four higher order elements were used in this region. This was done to obtain a better definition of local conditions in the region expected to have the most nonlinearity, and demonstrates the ability of the viscoplastic routine to accommodate various element types. Appropriate tying equations were included in the MARC analysis to insure proper compatibility at the interface of the two element types. The finite element model also included a simulation of structural and heat transfer

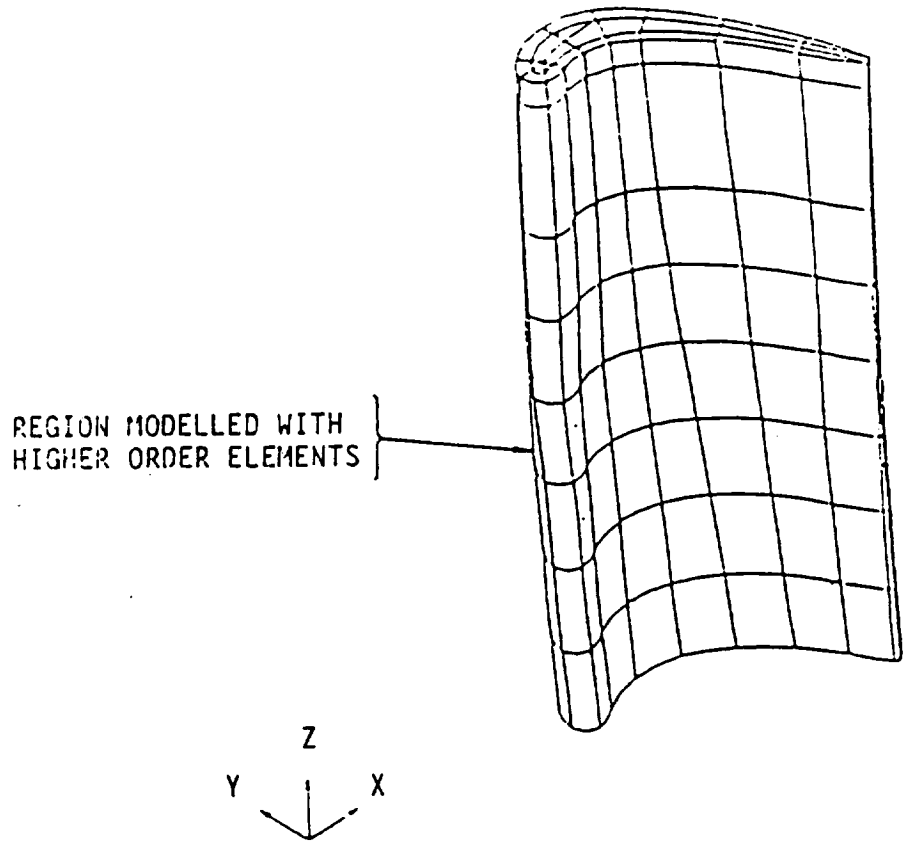

FIGURE 5.1 FINITE ELEMENT MESH USED FOR CONSTITUTIVE MODEL DEMONSTRATION.

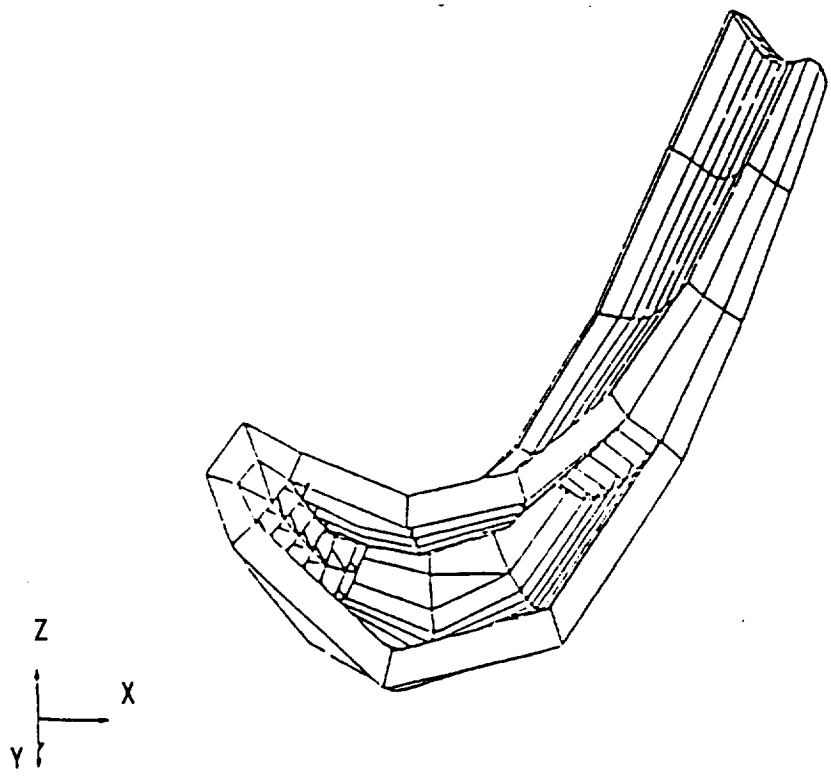

FIGURE 5.2 RADIAL VIEW ILLUSTRATING INTERNAL FEATURES OF THE HOLLOW AIRFOIL.

features in the internal cavity which are common in cooled turbine blades. These features were modeled by using reduced stiffness elastic solid elements. The density of these elements was also reduced to obtain the appropriate centrifugal loading. Figure 5.2 shows the location of these elements near the leading and trailing edges. The reduced stiffness and elastic behavior of these elements was achieved within the HYPELA user subroutine by bypassing the viscoplastic portions of the routine for the internal elements. The efficiency measures introduced by Cassenti [19] avoids matrix inversion on every increment by formulating the stiffness matrix, D, at a reference temperature only. Any elastic deviation from this reference stiffness due to incremental temperature change as well as all inelasticity is passed to the elements, the only portions of the routine which are accessed are those relating to calculating the stiffness matrix, D, at the reference temperature, and the elastic portion of the load vector, G.

5.1.1.1 Boundary Conditions and Loading

The loading and boundary conditions were chosen to simulate a typical commercial engine flight. The flight simulation is shown schematically in Figure 5.3 and includes periods of Taxi, Take-Off, Climb, Cruise, Descent, Taxi and finally Shutdown. The Take-Off potion includes a momentary pause in engine acceleration to more faithfully simulate actual "rolling take-off" conditions. This occurs between 15 and 20 seconds after the beginning of Take-Off (i.e. point "A" in Figure 5.3). Figure 5.4 shows the range of foil temperatures and the centrifugal load spectrum encompassed in the simulated flight. This range of temperatures exercises the material model over most of its range of applicability.

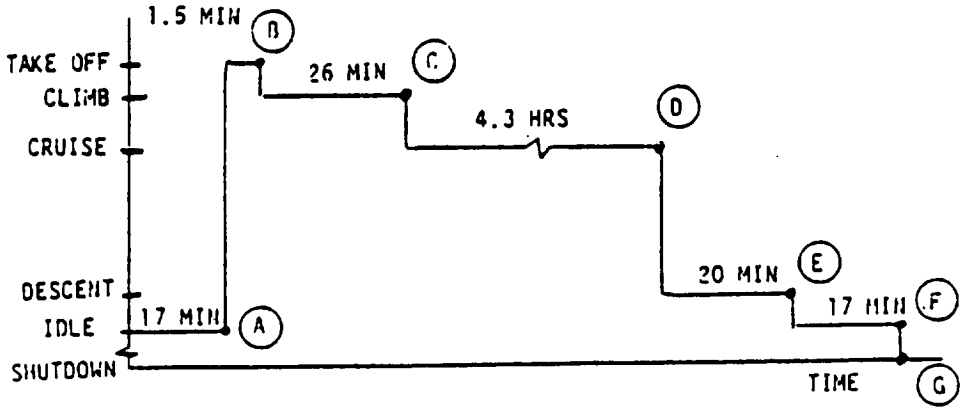

FIGURE 5.3 SIMULATED FLIGHT USED IN THE DEMONSTRATION OF THE WALKER B1900+Hf CONSTITUTIVE MODEL.

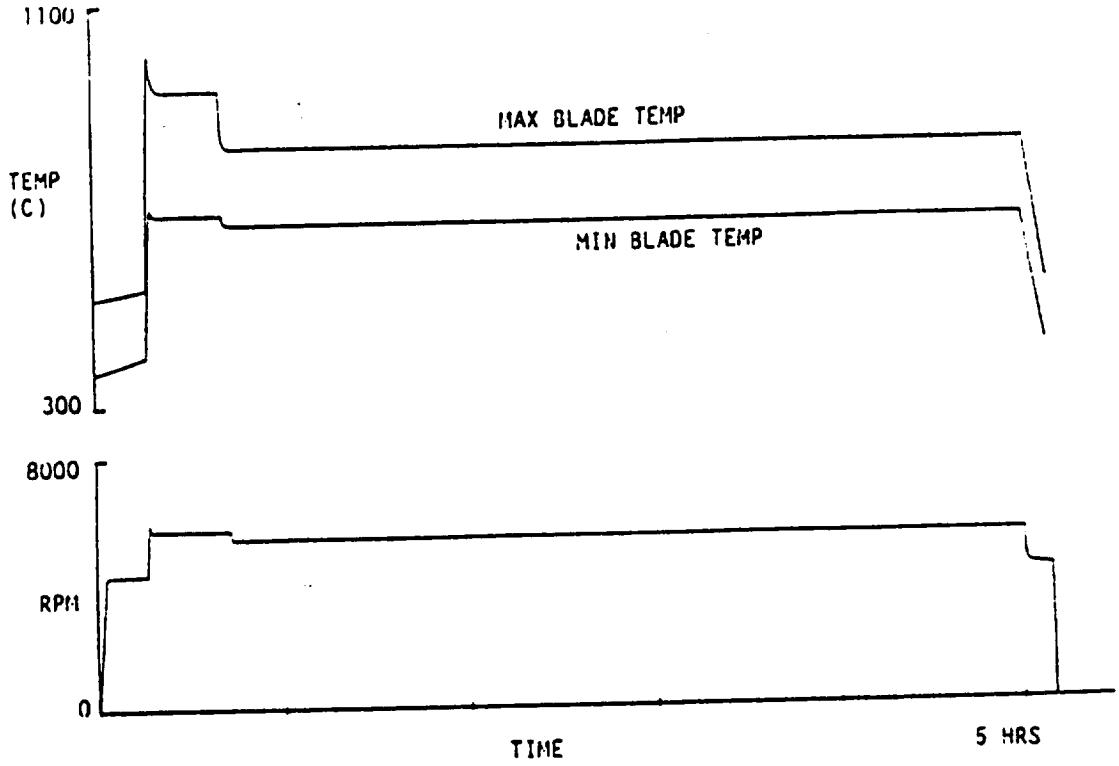

FIGURE 5.4 RANGE OF TEMPERATURES AND MECHANICAL LOADS DURING THE FLIGHT CYCLE.

Radial deflections were specified to be zero at the radially innermost section of the foil. Additional nodal boundary conditions were imposed in this plane to fully suppress rigid body motion.

In the MARC nonlinear stress analysis, an initial loading (MARC increment zero) is applied to the model. This "zero " increment is assumed to be elastic. In this analysis, a nominal centrifugal load corresponding to 200 RPM, and a uniform temperature of 429C was chosen. This loading was sufficiently small to preclude any nonlinear material behavior. Actual flight simulation loading began with increment one and proceeded by applying centrifugal and thermal loading in subsequent increments described in the "history definition" portion of the MARC job stream. Centrifugal loads were applied through the TRACTIONS option. The time at the end of each load increment was supplied through the CHANGE STATE option or the THERMAL LOAD option. Nodal temperatures were supplied through the CHANGE STATE option which accessed a previously generated thermal tape. The analysis proceeded until the cyclic response of the foil was noted to be stable from one flight to the next.

In a stress analysis involving nonlinear material behavior, the step size used to define the load history is extremely important. To allow the possibility of a very small step size in the stress analysis, temperature profiles were defined frequently on the thermal tape. The maximum nodal temperature change from one profile to the next was 50°C. In the Take-Off portion of the flight, where foil temperatures change rapidly, 25 time points were used. To provide results which were as accurate as possible, all available time points were used in the first analysis. Subsequent analyses used larger step sizes and will be discussed in a subsequent section. During

the Cruise portion of the flight, the temperature profile is essentially constant. However, the material model state variables continue to evolve (e.g. creep deformation), so that step size is still important. Consequently, a large number of increments were used in this portion of the flight. Sensitivity to step size in the Cruise portion will also be discussed in a separate section. Table 5.1 shows the number of stress increments used to define the various parts of the flight.

5.1.2 Stress Analysis Results; Accuracy and Stability

Two locations on the airfoil have been selected to illustrate the results of the analysis. The behavior at these locations was expected to be very different and to provide an evaluation of the model over the widest possible range of conditions on the airfoil. Figure 5.5 shows the location of these points superimposed on the temperature profile during Cruise. Point A corresponds to the integration point nearest the external wall at the leading edge "hot spot", and was expected to have the largest amount of inelasticity in the foil. Point B corresponds to the integration point nearest the internal wall at an adjacent "cool spot". Both points are in the region of the model having higher order solid elements.

There are no simple or well established methods for evaluating the accuracy of solution in a nonlinear analysis of a complex component like the turbine airfoil analyzed here. The normal checks on overall equilibrium and compatibility provide little information about the fidelity of the inelastic stress-strain results. However, some measure of confidence can be gained by checking that the effective stress-strain state during initial loading corresponds to the stress-strain response of a uniaxial bar, by monitoring the

TABLE 5.1 NUMBER OF STRESS INCREMENTS USED TO DESCRIBE THE FLIGHT

Portion of Flight	Reference Point in Figure 3	Stress Increments in 1st Flight	Number of increments	Duration (sec)
Taxi	up to A	1 - 3	3	1000
Take-Off	A to B	4 - 26	23	90
Climb	B to C	27 - 34	8	1522
Cruise	C to D	35 - 62	28	15298
Descent	D to E	63 - 78	16	503
Taxi	E to F	78 - 82	4	1100
Shut-Down	G	83	1	500

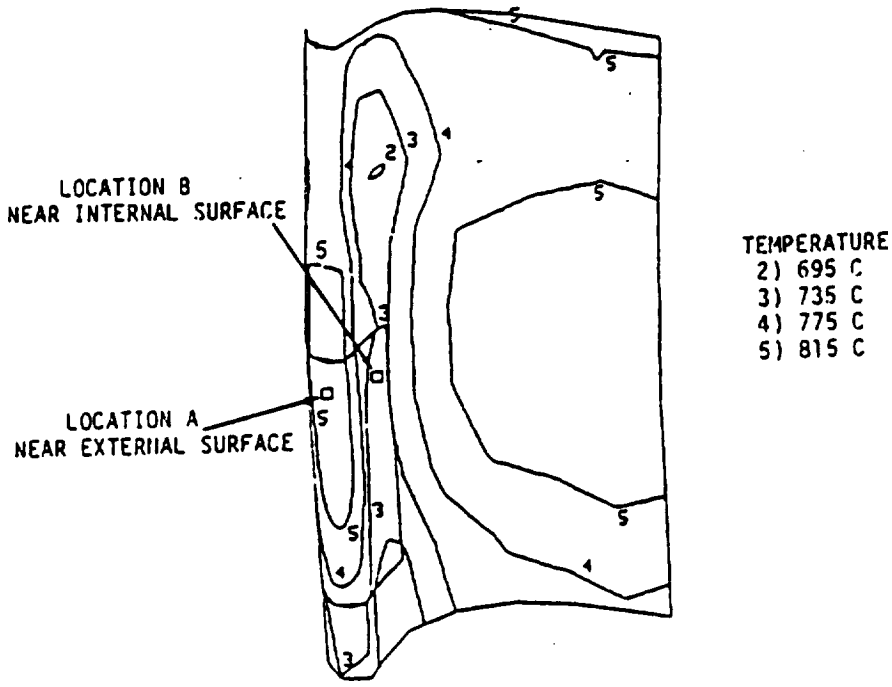

FIGURE 5.5 STEADY STATE TEMPERATURE PROFILE DURING CRUISE AND LOCATIONS A AND B EXAMINED IN DETAIL.

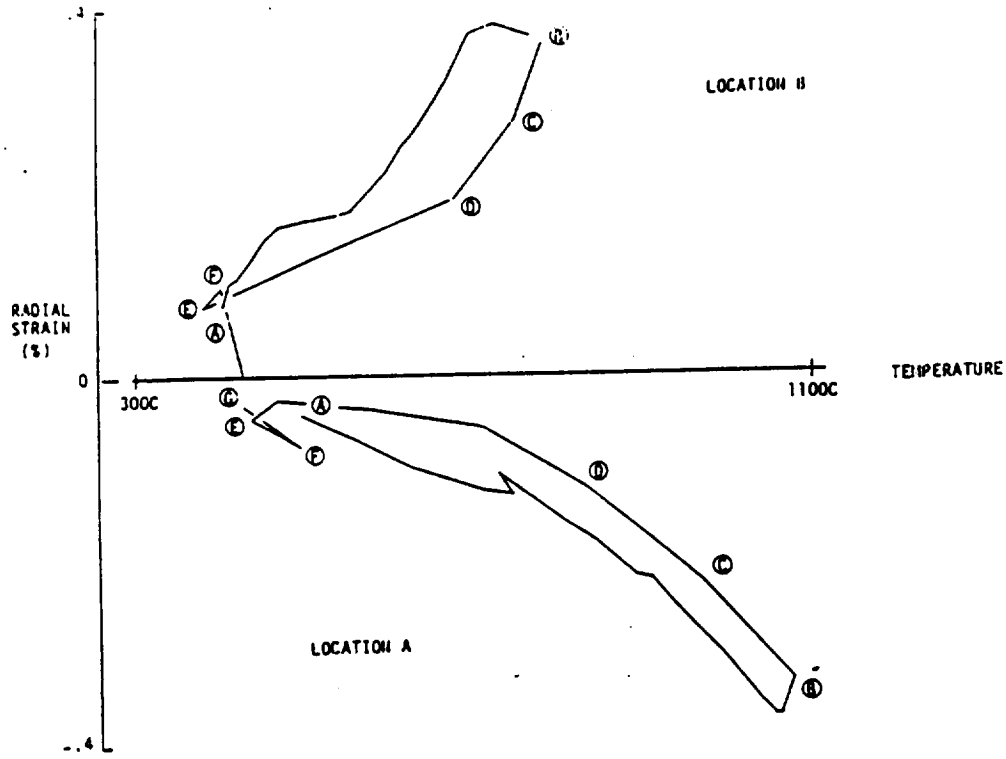

FIGURE 5.6 STRAIN-TEMPERATURE HISTORY AT LOCATIONS A AND B DURING FIRST FLIGHT.

C-2

"smoothness" of the material model's behavior and the sensitivity of the the results to step size. Finally, engineering judgement must be used to evaluate whether the overall structural behavior is reasonable. The results of the analysis at locations A & B (Figure 5.5) will be reviewed with regard to these "criteria".

Figure 5.6 shows the strain-temperature history at the locations of interest during the first flight. The Take-Off portion is shown in more detail than the remainder of the flight. The various parts of the flight are labeled consistently with the flight definition shown in Figure 5.3. Figures 5.7 and 5.8 show the stress-strain response during all three flights at locations A and B respectively. The two locations present somewhat different pictures of the cyclic response: At location A, it is appears that a stabilized hysteresis loop is achieved after just three flights. At the end of Take-Off, the largest variation in stress or strain between the second and third flights is less than 2% (see Table 5.2) and this is much less than the change between the first and second flight. However at location B the change between successive flights is decreasing less rapidly (5% and 4%). Thus the analysis predicts that different parts of the foil stabilize at different rates, which is reasonable since the loading and temperatures vary significantly from one location to another. In an actual airfoil it could be expected that the cyclic response from one flight to the next may be very similar even though it may never completely "stabilize" due to load redistribution from adjacent sections. As a result the hysteresis loop at any location may ratchet throughout the service life. Consequently, it is not appropriate to judge the material model stability based on the stress - strain response alone. More useful criteria are those of smoothness and sensitivity

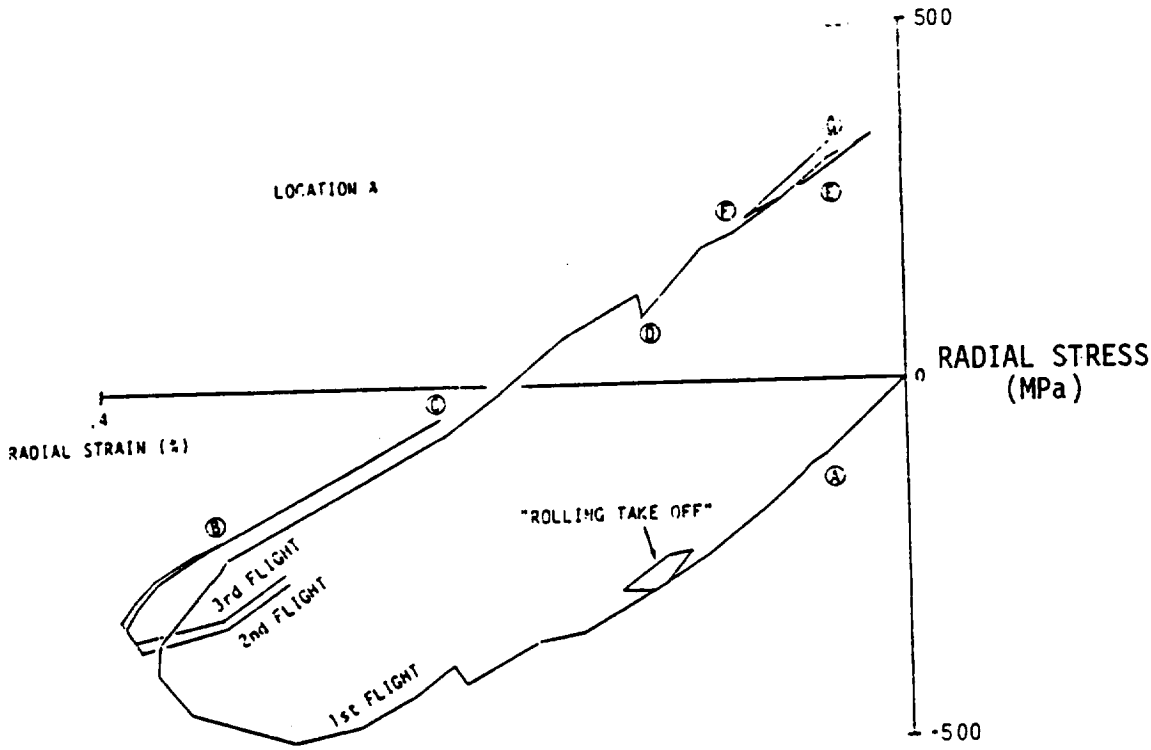

FIGURE 5.7 STRESS-STRAIN RESPONSE AT LOCATION A.

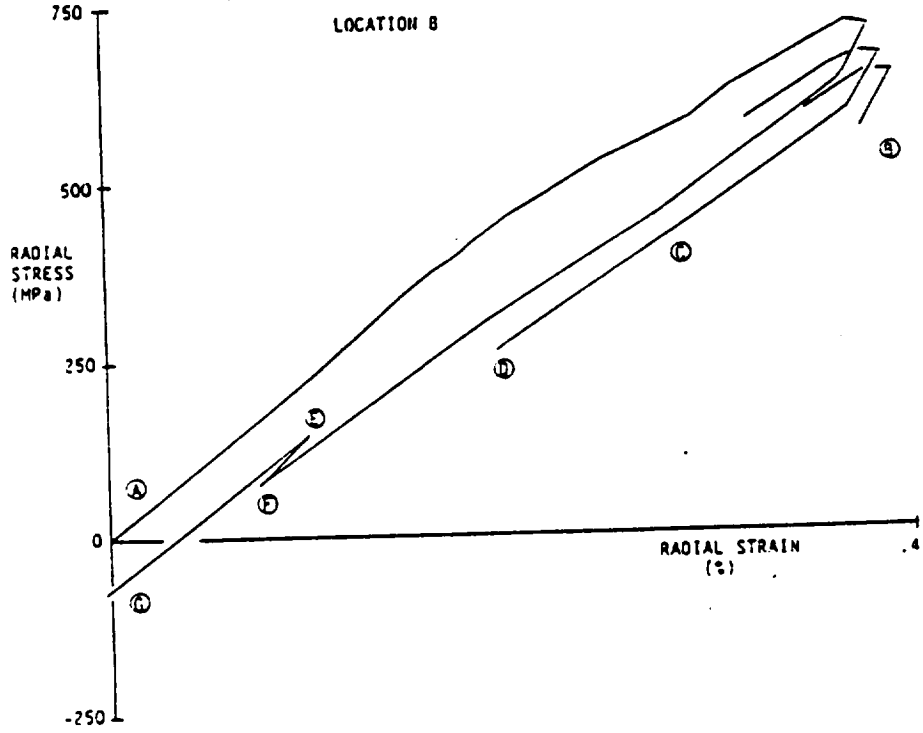

FIGURE 5.8 STRESS-STRAIN RESPONSE AT LOCATION B.

TABLE 5.2 CHANGE IN STRESS AND STRAIN FROM ONE FLIGHT TO THE NEXT

		Values at End of Take-Off		
		Stress (MPa)	Strain (%)	Inelastic Strain (%)
At Location A	1st Flight	-235.9	-.339	-.239
	2nd Flight	-213.1	-.344	-.267
	3rd Flight	-209.7	-.343	-.276
At Location B	1st Flight	629.7	.365	.068
	2nd Flight	594.5	.371	.096
	3rd Flight	569.0	.376	.119

to step size. The stress-strain response in Figures 5.7 and 5.8 shows no tendency to severe oscillation. The "looping" observed during initial loading at location A is a result of the complex thermal and mechanical loading on the foil and should not be interpreted as of a material model deficiency. Such is the case during the acceleration pause in Take-Off as seen in Figure 5.7.

Additional insight regarding the behavior of the material model and the adequacy of the solution can be gained by examining the evolution of key state variables and the inelastic strains. Figure 5.9 shows the evolution of the back stress in the radial direction at locations A and B during the first flight. Once again, the Take-Off pause is easily identified. The evolution of the inelastic strain in the radial direction during the first flight is shown in Figure 5.10 for location A. It is clear that these variables evolve smoothly, adding confidence in the behavior of the model and the fidelity of the analysis.

Figure 5.11 shows the accumulation of inelastic strain at location A during all three flights. Several observations can be made. First, the bulk of the inelastic strain is accumulated during Take-Off on the first flight. Secondly, the element exhibits some degree of reversed inelasticity as evidenced by the decrease in the inelastic strain during Cruise and Descent. The Take-Off portions of the second and third flights have nearly the same amounts of inelastic strain accumulation, indicating that the overall hysteresis loop shape is essentially unchanged.

A further check on the model can be made by checking that the effective stress and effective strains during initial stages of loading coincide with the normal monotonic tensile behavior. This check is valid only during early stages of loading before significant inelastic history has been

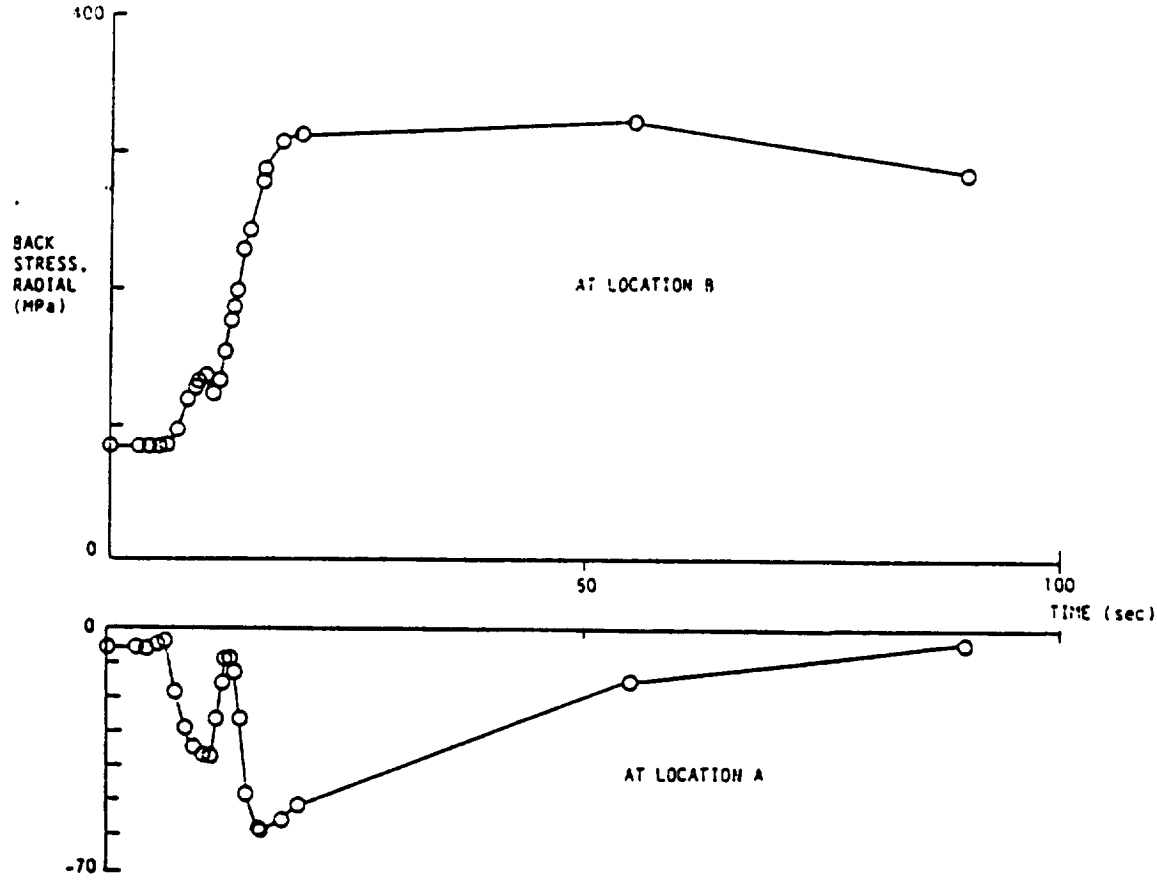

FIGURE 5.9 EVOLUTION OF BACK STRESS DURING TAKE-OFF IN THE FIRST FLIGHT.

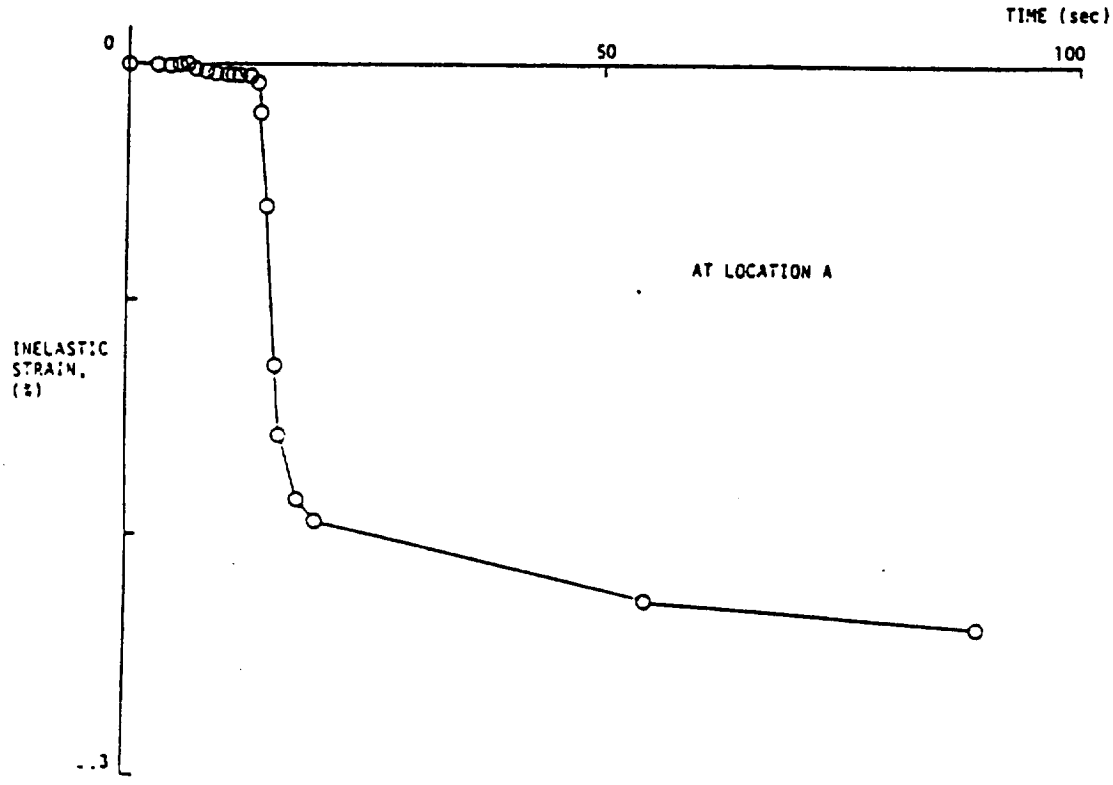

FIGURE 5.10 EVOLUTION OF INELASTIC STRAIN IN THE RADIAL DIRECTION DURING THE FIRST FLIGHT.

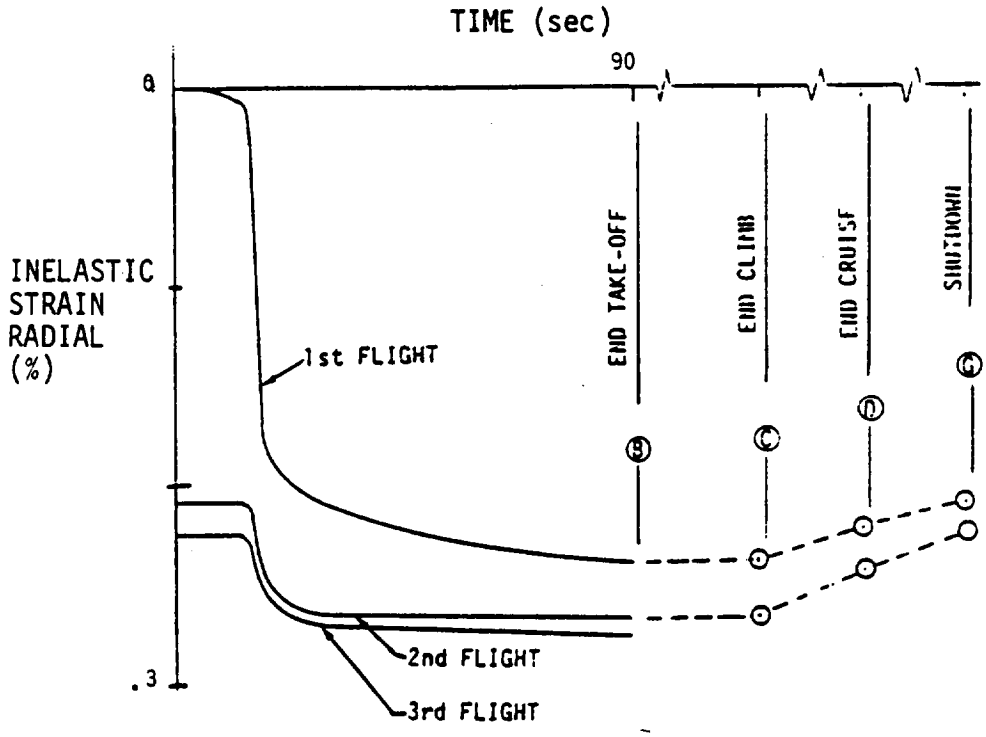

FIGURE 5.11 ACCUMULATION OF INELASTIC STRAIN AT LOCATION A DURING ALL THREE FLIGHTS.

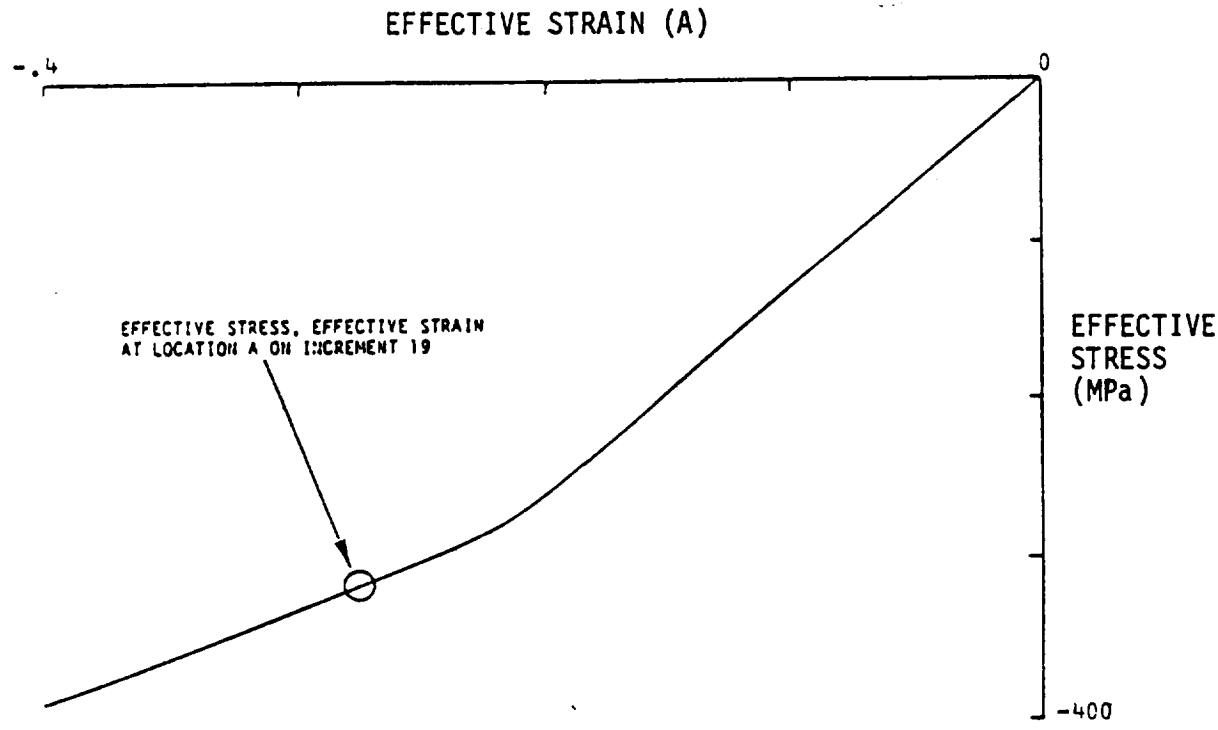

FIGURE 5.12 THE EFFECTIVE STRESS/EFFECTIVE STRAIN AT LOCATION A FOLLOWS EXPECTED MONOTONIC CURVE.

accumulated. This check was made for location A at the increment 19 which shows the first significant amount of inelastic strain. At increment 19, the inelastic strain is approximately 10% of the total mechanical strain. On the previous increment the inelastic strain was only 4% of the total strain. Figure 5.12 shows the monotonic stress-strain curve predicted by the material model (at a temperature and strain rate consistent with increment 19) along with the effective stress/effective strain calculated for that increment. Clearly, the foil analysis is in good agreement with the expected result.

The Walker model for B1900+Hf had been formulated to account for nonproportional loading. The results at point A were examined to determine the degree of proportionality in loading. In general, the stress-strain state at point A is triaxial. It was found that the directions of the principal stress, strain and inelastic strain relative to the geometric axes were invariant throughout the flight cycle. One of the principal directions was very nearly radial. The remaining principal directions were in a chordal plane, i.e. parallel to the engine centerline, but were different for stress, strain and inelastic strain. Even though the principal directions remained constant throughout the cycle, the relative magnitudes of the stress and strain components were not constant. The results at two points in the cycle can be considered proportional if all the component quantities at the two time points are different in the same proportion. A convenient measure of this is obtained by forming the scalar product of the stress (or strain) vectors at the two time points. That is,

$$\underset{\sim}{\sigma}_j \cdot \underset{\sim}{\sigma}_o \quad \text{for stress,}$$

$\underset{\sim}{\varepsilon}_j \cdot \underset{\sim}{\varepsilon}_o$ for strain,

where subsrcript o denotes the vector at a reference time point and subscript j denotes the vector at another time point of interest in the cycle. The reference time point is taken to be Increment 17 of the analysis. Very little inelasticity has occurred at point A up to Increment 17. Figure 5.13 shows the results for the first flight. Although not exactly proportional, the deviation from proportionality is not great in the Take-Off portion where the bulk of the inelasticity occurs. This is further indicated in Figure 5.14 in which the two largest principal strains are cross plotted. The third principal strain is nearly zero. Based on the loading at location A, it can be concluded that the example problem did not test the material model under severely nonproportional loading. However it should be remembered that in laboratory tests, the material inelastic response was altered very little by nonproportional loading.

5.1.3 Sensitivity to Step Size and Efficiency

A study was conducted to determine the sensitivity of the solution and material model behavior to step size. The results reported above, (Base Case), were obtained using 23 increments to describe the Take-Off portion between ground Idle and the end of Take-Off. In this study, this same period was described in 10 increments, (Case 2), ard in 6 increments, (Case 3). Only the first flight was studied. Table 5.3 compares the steps sizes between the three analyses and Figure 5.15 shows the resulting stress-strain response at location A. As indicated in Table 5.3 and in Figure 5.15, Case 3 failed to converge to a solution on increment 8. The convergence failure occurred at an element other than location A. Case 2 converged for all increments and

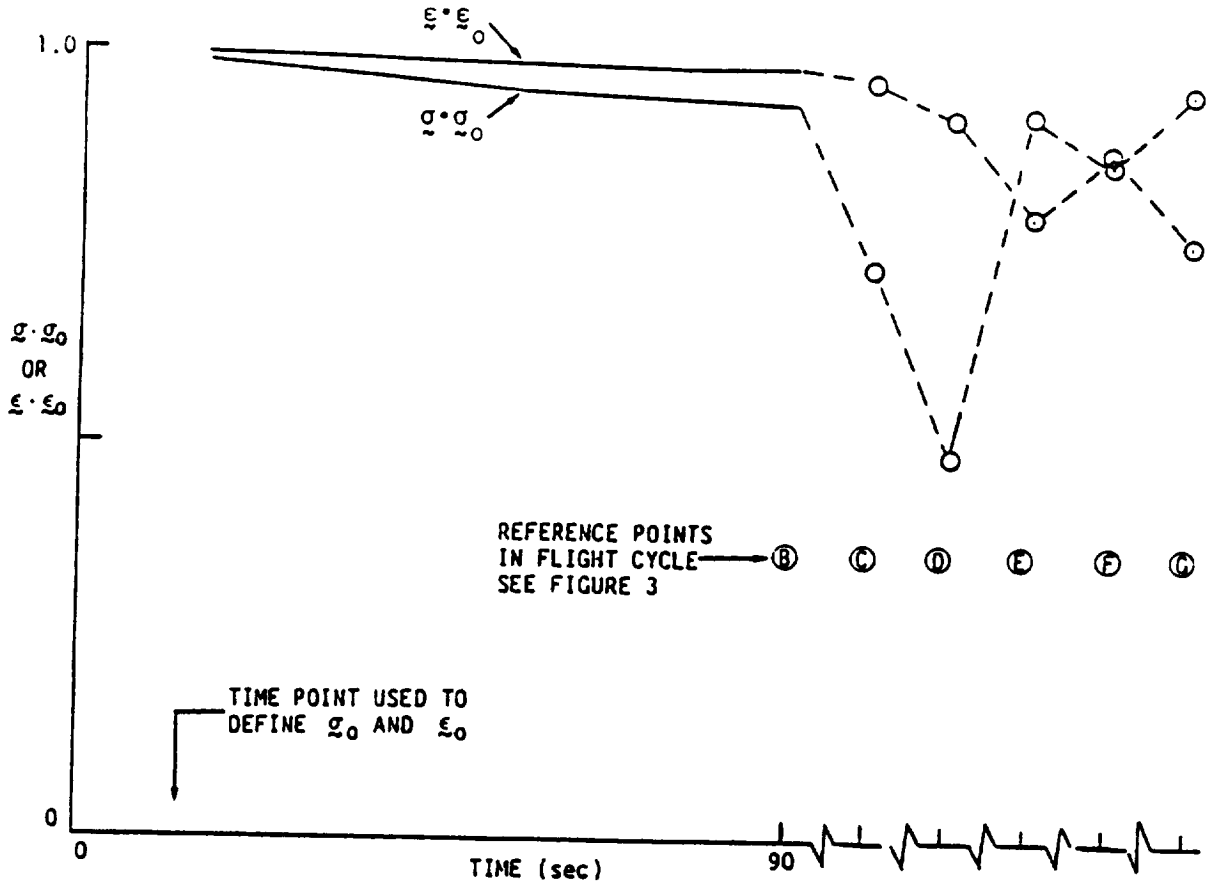

FIGURE 5.13 THE DEGREE OF NON-PROPORTIONALITY DURING THE FIRST FLIGHT AT LOCATION A.

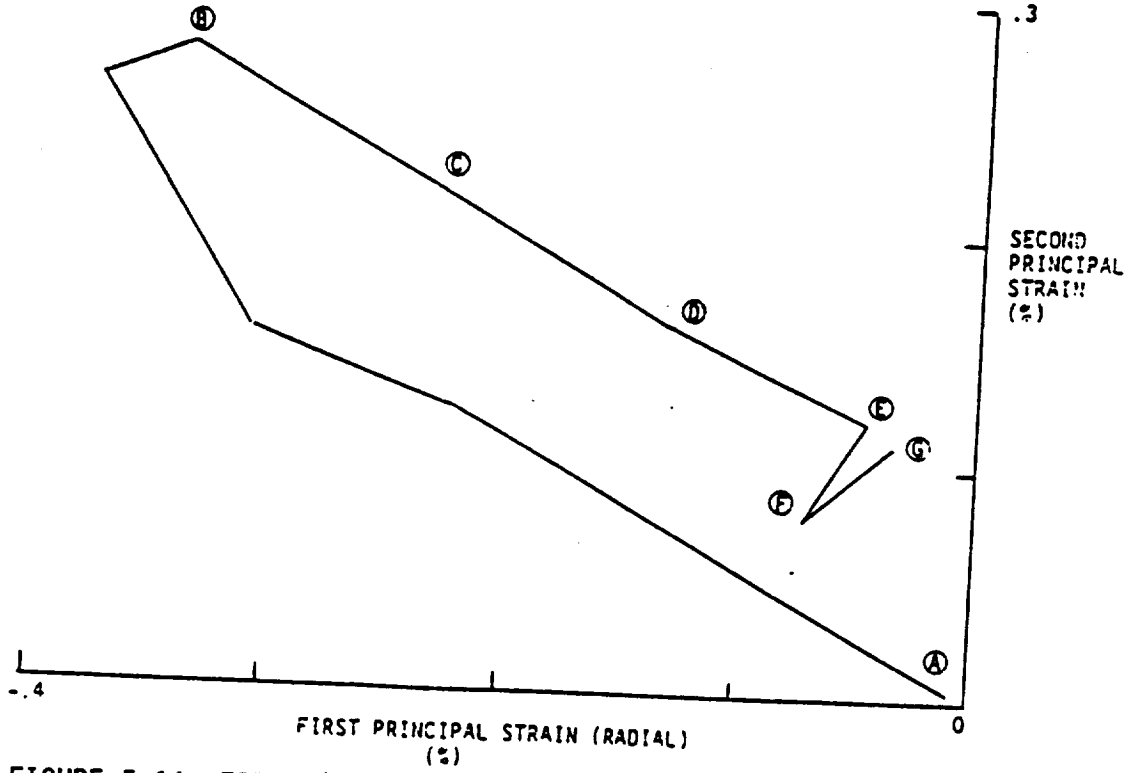

FIGURE 5.14 FIRST (RADIAL) AND SECOND PRINCIPAL STRAINS AT LOCATION A DURING THE FIRST FLIGHT.

TABLE 5.3 STEP SIZES USED IN SENSITIVITY STUDY

Time After Start of Take-Off (sec)	Base Case Incr.	T* (C)	RPM	Case 2 Incr.	T* (C)	RPM	Case 3 Incr.	T* (C)	RPM
0.00	3	0	5275	3	0	5275	3	0	5275
3.00	4	20	5317						
4.20	5	23	5447	4	43	5447			
5.15	6	38	5804						
6.15	7	54	6326	5	93	6326	4	136	6326
7.02	8	38	6430						
7.95	9	52	6489	6	90	6489			
8.88	10	42	6516						
9.00	11	21	6518	7	93	6518	5	183	6518
10.00	12	22	6540						
10.72	13	33	6625						
11.43	14	53	6770	8	128	6770			
12.00	15	41	6912						
12.53	16	48	7052	9	89	7052	6	217	7052
12.87	17	21	7091						
13.22	18	22	7132						
13.74	19	26	7188	10	68	7188			
14.52	20	35	7253						
15.69	21	49	7350						
16.00	22	12	7376	11	96	7376	7	164	7376
18.00	23	36	7365						
20.00	24	21	7363	12	56	7363	**8	56	7363
55.00	25	47	7360						
90.00	26	18	7360	13	66	7360			

* Largest temperature change from one increment to the next.
** Failed to converge

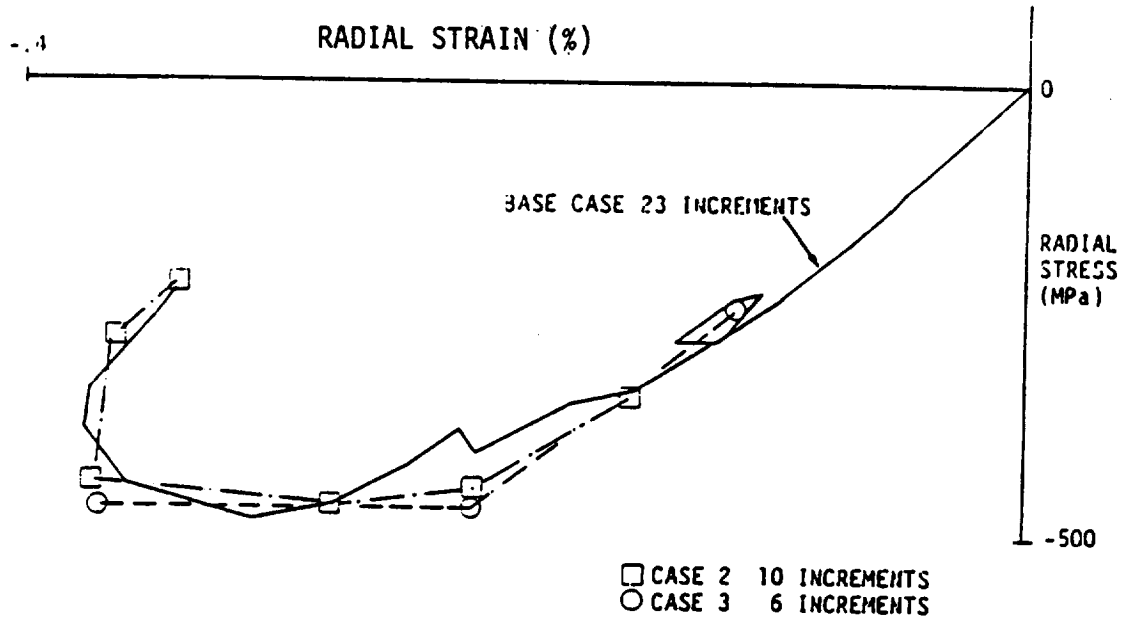

FIGURE 5.15 EFFECT OF STEP SIZE DURING TAKE-OFF OF FIRST FLIGHT AT LOCATION A.

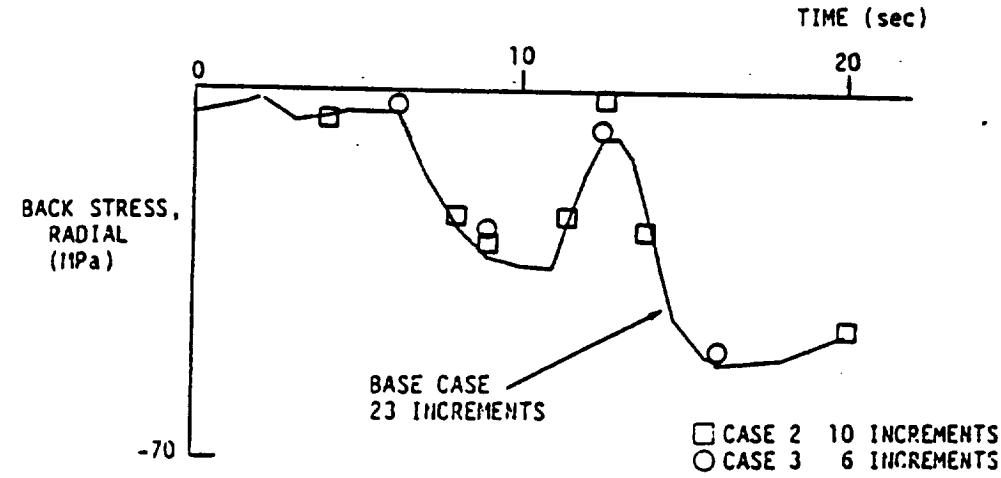

FIGURE 5.16 THE EFFECT OF STEP SIZE EVOLUTION OF THE BACK STRESS AT LOCATION A DURING TAKE-OFF IN THE FIRST FLIGHT.

produced results at the end of Take-Off which are in very good agreement with the Base Case. The stress and strain are within 2% of the Base Case. Figure 5.16 shows in more detail how the back stress in the radial direction at location A differs between the analyses.

A similar study was conducted during the Cruise portion of the flight to better understand possible causes of convergence failures. During Cruise, the mechanical and thermal loading is constant, so that only the size of the time step (and some small amount of structural load redistribution) controls the evolution of the constitutive equations. To understand the findings it is necessary to realize that during each load increment, the constitutive relations are integrated over several subincrements. It was discovered that very large time steps can lead to a situation in which very large changes in the back stress occur during the subincrementation loop even though the global stress and strain values changed only slightly. Table 5.4 shows this behavior for a very large (9000 second) time step. The present increment converged with no obvious difficulty but the next increment failed to converge due to the very large difference between the direct stress and the back stress resulting at the end of the present increment. This situation is made possible because no separate convergence check is made on the state variables during the subincrement loop; only the effective plastic strain increment is checked for convergence. While this does not pose a major problem in the code, it would be fruitful to develop appropriate convergence criteria for the state variables and automatic subincrementation so that larger time steps might then be possible.

It should also be noted that the improved efficiency integration techniques introduced by Cassenti [19] resulted in very fast solution times

TABLE 5.4 CHANGE IN STRESS, STRAIN AND BACK STRESS DURING LARGE SUBINCREMENT TIME STEP

Subincrement Number	Time Step (sec)	Stress (MPa)	Strain (%)	Back Stress (MPa)
Initial Values	-	-145.7	-.0993	-24.6
1	4500.	-143.9	-.0995	-69.4
2	4500.	-144.3	-.0997	-389.2

for the nonlinear analysis. Computing times for the nonlinear analysis were compared to computing times for a conventional elastic analysis at various times in the flight cycle. It was found that the matrix solution times were the same, indicating that the material model routines are very efficient. As noted previously, the efficiency measures developed by Cassenti [19], avoids matrix inversion on each increment. Instead, the stiffness matrix is assembled at a reference temperature only, and any change in the stiffness due to temperature dependent elastic properties is passed to the main MARC program as an incremental inelastic stress vector. The reference temperature stiffness matrix is assembled only at the start of the inelastic analysis and each time the inelastic analysis is restarted. The net effect is that an inelastic analysis involving several increments actually uses less computing time than an equal number of separate elastic analyses, because each separate elastic analysis requires the stiffness matrix to be assembled anew.

5.2 Evaluation of Integration Schemes at Pratt & Whitney Aircraft

Computational efficiency is a major concern in performing large nonlinear analyses like the one reported above. Therefore a study was conducted to determine the relative efficiencies and stability characteristics of the Euler foreword difference method as used in the Walker and Bodner-Partom formulations and the NONSS (Noniterative, Self-correcting Solution) method of Tanaka [21], as used with the Bodner-Partom model for one-element calculations at SwRI.

5.2.1 Background

Previously reported studies at PWA using the MARC non-linear finite element deck showed that Walker's theory using a self-adaptive Euler forward difference integration was approximately three times faster than the Bodner-Partom model using the same integration method. These results were at variance with another study conducted by P.K. Imbrie at Texas A & M, [22,23], which compared Walker's model with a simpler version of the Bodner-Partom model and showed about a 16 percent advantage for Walker's model. In examining the differences between these earlier studies and those done at Pratt & Whitney using the MARC finite element deck, three differences were identified:

- The Texas A&M study used the one dimensional form of the models. The same computing time ratios may not follow for the three dimensional form.
- The Pratt & Whitney study evaluated the nonisotropic version of Bodner-Partom model which includes the directional hardening terms. The Texas A&M study utilized the simpler isotropic version of the Bodner-Partom model.
- The Texas A&M study used a constant integration step size while the Pratt & Whitney study used a self adaptive (variable) integration step.

The present study was undertaken at PWA to determine which of these items contributed to the large differences in computational efficiency that have been observed and to evaluate the integration method developed by Tanaka, [21], referred to in this report as the NONSS method. The NONSS method solves a set of simultaneous equations involving partial differentials of the terms of the constitutive model to obtain the incremental values of the stresses and other evolutionary quantities. Thus a matrix inversion is performed at each integration step. The potential advantage for the NONSS method is thought to

be the ability to utilize larger time steps than for the Euler forward difference method. A comparison of the smallest stable time step size for the NONSS and the Euler methods was therefore performed.

The MARC code allows the user to implement very general constitutive relationships into the program by means of the user subroutine HYPELA. HYPELA returns an inelastic stress increment for each strain increment estimated from equilibrium solutions in MARC. After obtaining the inelastic stress for each integration point in the structure, MARC again solves the equilibrium relations and checks to see if the strain increments have changed. The sequence is repeated until the strains converge. In order to reduce computing costs it is desirable to minimize the number of load increments computed by the MARC code. On the other hand the size of the integration step must be made small to insure the integration stability of the stiff constitutive models. To reconcile these divergent requirements the MARC loading step is set as large as feasible and subsequently subdivided for detail integration within subroutine HYPELA. The means for doing this time step subdivision is the user initialized integer parameter, NSPLIT. Upon entering HYPELA, each time step is divided into NSPLIT subincrements. The value of NSPLIT after being initialized by the user is adjusted within HYPELA by maintaining the elastic plus plastic strain step within specified bounds.

As an aid in the development of the HYPELA subroutines for the Walker and the Bodner-Partom models, a MARC "look-alike" deck was written which has a single multiaxial element and a means for specifying a general load history. In addition, a simplified method for estimating the strain increment vector based on the plane stress element is utilized. This mini-MARC deck was used to perform most of the computing efficiency comparisons for the present study.

Three constitutive behavior routines have been evaluated extensively to determine their computing efficiency and stability characteristics. Two of these employed the Bodner-Partom constitutive model and one the Walker model. The Bodner-Partom model was integrated in one routine by the Euler forward difference method and in the other by the NONSS (Noniterative, Self-correcting Solution) method. The Walker model was integrated using the Euler forward difference method. Two approaches were used to evaluate these routines. The first approach was to compare execution times for each routine when solving a simple uniaxial loading case while varying the number of integration time steps used in the solutions. Stability limits were determined by finding step sizes for which the solution failed to converge. The second approach involved the use of a timer analysis which tracked the amount of computing time used by the various parts of each set of routines.

5.2.2 Results

The execution times for the load cases studied are summarized in Table 5.5. The times shown are for a single load history at 1093°C, a strain rate of 4×10^{-5} per second, a strain range of .6%, and an R-ratio of minus infinity. All computation times shown in Table 5.5 represent actual numerical computation time, the computer time spent for I/O and for accessing the clock were subtracted since the three routines differed in their respective I/O burdens. The convergence criterion used in each of the three routines was identical, namely the calculated out-of-plane stress for the uniaxial specimen was forced to be within a small tolerance of zero.

TABLE 5.5 A COMPARISON OF COMPUTING TIMES FOR 3 CONSTITUTIVE MODEL ROUTINES

CASE #	THEORY	METHOD	CYCLES	INCREMENTS	SUB-INCREMENTS	TIME
1.	Bodner-Partom	NONSS	2	80	2	failed
2.			2	80	3	failed
3.			2	80	4	3.50
4.			2	80	8	6.34
5.			2	320	1	3.53*
6.	Bodner-Partom	Euler (self-adaptive)	2	80	1	1.28
7.			2	80	3	1.62
8.			2	80	4	1.26
9.			2	80	8	1.26
10.			2	320	1	1.76
11.	Bodner-Partom	Euler (self adaptive, without directional hardening terms)	2	320	1	1.43
12.	Walker	Euler (self-adaptive)	2	80	1	0.45
13.			2	80	2	0.45
14.			2	80	8	0.45
15.			2	320	1	1.03**

* 0.78 to assemble matrix
1.15 to invert matrix
** 0.81 when adjusted for excess material properties calculations

The first 5 cases shown in Table 5.5 summarize the experience with the NONSS integration method. It can be seen that the method is in general slower than the other two routines studied (Bodner-Partom's model using Euler integration shown as cases 6 through 10 and Walker's model using Euler integration shown as cases 11 through 14). In addition it can be seen that there is a tendency to fail to converge for coarser time steps. One difference between the NONSS routine and the other two studied is the lack of a self adaptive time step (a self adaptive time scheme is used at SwRI). This is evident in the comparison of the computing times in cases 3 and 4 where the number of integration time subincrements was doubled resulting in an approximately doubled computing time. For the other two routines the number

of subincrements was set initially for each increment, but underwent an automatic readjustment internally (self-adaptive time steps). This self adaptive feature often results in the same overall computation time even though the initial subincrement value was high. Inclusion of a self adaptive time step with the NONSS method would likely have prevented the convergence failures which occurred in cases 1 and 2 without significant loss of efficiency.

The present study supports the conclusions reached by Kumar et al. [24] and by Imbrie, Haisler, and Allen [23] namely that the Euler forward difference or a minor modification of it is the most efficient method. Evidence of this for the NONSS and Euler methods is seen by comparing cases 5 and 9 in Table 5.5. For case number 9 the self adaptive time stepping was suppressed in order to get a direct comparison of the two methods.

An issue raised in the Second Annual Report for the HOST Constitutive Modeling Contract for Isotropic Materials questions why the Bodner-Partom model integrated by the Euler forward difference method should be so much slower than the Walker model. Additional work reported in a private communication by P. K. Imbrie, Department of Aerospace Engineering, Texas A&M University is summarized in Figure 5.17. These results show the Bodner-Partom model as only 1.16 slower than Walker's model for the same number of integration time steps. Three differences between P. K. Imbrie's results and those shown in Table 5.5 must be considered. First, the form of Bodner-Partom's model used by Imbrie contained only the isotropic hardening terms. The directional hardening terms were not included as they were for the results in Table 5.5. Second, Imbrie employed only a single degree of freedom in his calculations, whereas the results in Table 5.5 are based upon calculations for six stress components. The third difference between the two studies which is

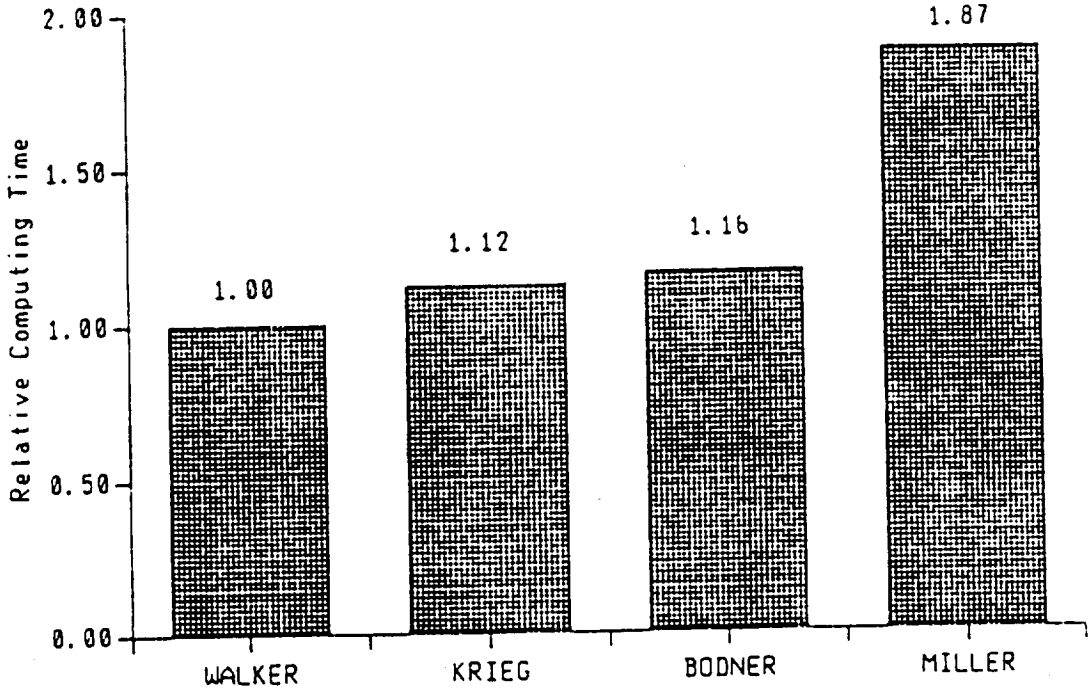

FIGURE 5.17 RESULTS OF TEXAS A&M STUDY (P.K. IMBRIE), STUDY PERFORMED USING ONE-DIMENSIONAL MODELS. Isotropic form of Bodner's model was used.

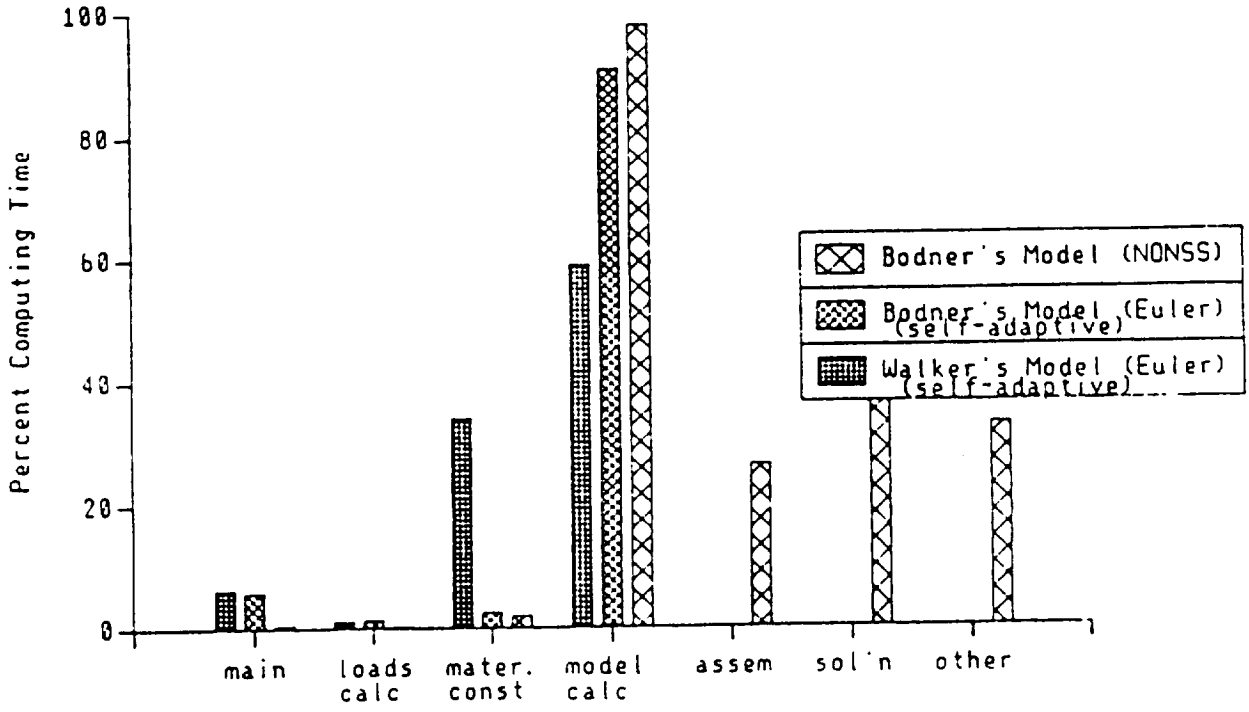

FIGURE 5.18 RESULTS OF TIMING STUDY, STUDY PERFORMED USING THREE-DIMENSIONAL MODELS. Non-isotropic form of Bodner's model was used.

significant for overall computing time and one which must be included for use with nonlinear finite element calculations is self adaptive time stepping. The Imbrie study used a fixed time step which was parametrically varied to explore calculation stability. Previous studies as well as the much of the results in Table 5.5 are based as already indicated a self adaptive integration time step. When this self adaptive feature is suppressed as in cases 9 and 14, the computation times for the Walker and Bodner-Partom's models become much closer. The difference becomes smaller still when the directional hardening calculations for Bodner-Partom's model are skipped. It was not feasible to make a direct comparison between a simple uniaxial calculation and that for the full tensorial formulation. It is presumed that much of the remaining difference between Imbrie's results and Table 5.5 is due to use of all tensorial components.

The cases 6 through 9 and 11 through 13 compare the response of Bodner-Partom and Walker's models to various initializations of the subincrement parameter. For Walker's model the self adaptive time step quickly finds the lowest level and consequently completes the integration in the same amount of computing time regardless of the initial value of the subincrement. For Bodner-Partom's model this is also true to some extent. However an examination of case number 6 shows that initializing the subincrement parameter at too small a value can actually increase the total integration time.

In addition to the studies to compare the computing efficiency for the three constitutive routines, a timer analysis of cases 5, 9, and 14 were conducted to determine which portions of the algorithms actually consumed the computing time. The results are shown in Figure 5.18. Two things of significance are evident from these results. The first is that a nearly 40%

of the computing time for the NONSS method is spent in matrix inversion and solution. Thus if the matrix were inverted analytically (rather than numerically) and the inverted matrix assembled directly, the NONSS method could be more competitive with the Euler forward difference method. The second item of significance shown in Figure 5.18 is that the routine containing the Walker model contains a serious inefficiency in the calculation of the material constants. Examination of the code suggests that a 20% increase in calculation speed could be realized by elimination of redundant calculations.

5.3 Evaluation of Integration Schemes at NASA Lewis Research Center

In the analytical methodologies developed in this program, the MARC nonlinear finite element computer code was incorporated with the Bodner-Partom and the Walker model. An explicit Euler method with a self-adaptive scheme was employed for integrating the viscoplastic equations. These computer subroutines were completed last year and was subsequently delivered to NASA program manager, Mr. Albert Kaufman.

NASA's experience of the computation requirements of the Bodner-Partom model in an inelastic blade analysis is somewhat different from that at PWA. For comparison purposes, the work at NASA Lewis Research Center is summarized in the next paragraph.

Using the MARC finite-element code equipped with subroutines containing the Bodner-Partom and Walker models, Kaufman et. al [25] recently performed analyses for the turbine blade problem described in Section 5.1. Slight modifications were also made to the code to improve numerical efficiency. The finite-element mesh and the mission analyzed were identical to those shown in Figs. 5.1 and 5.3. Figure 5.19 shows result of Kaufman et al

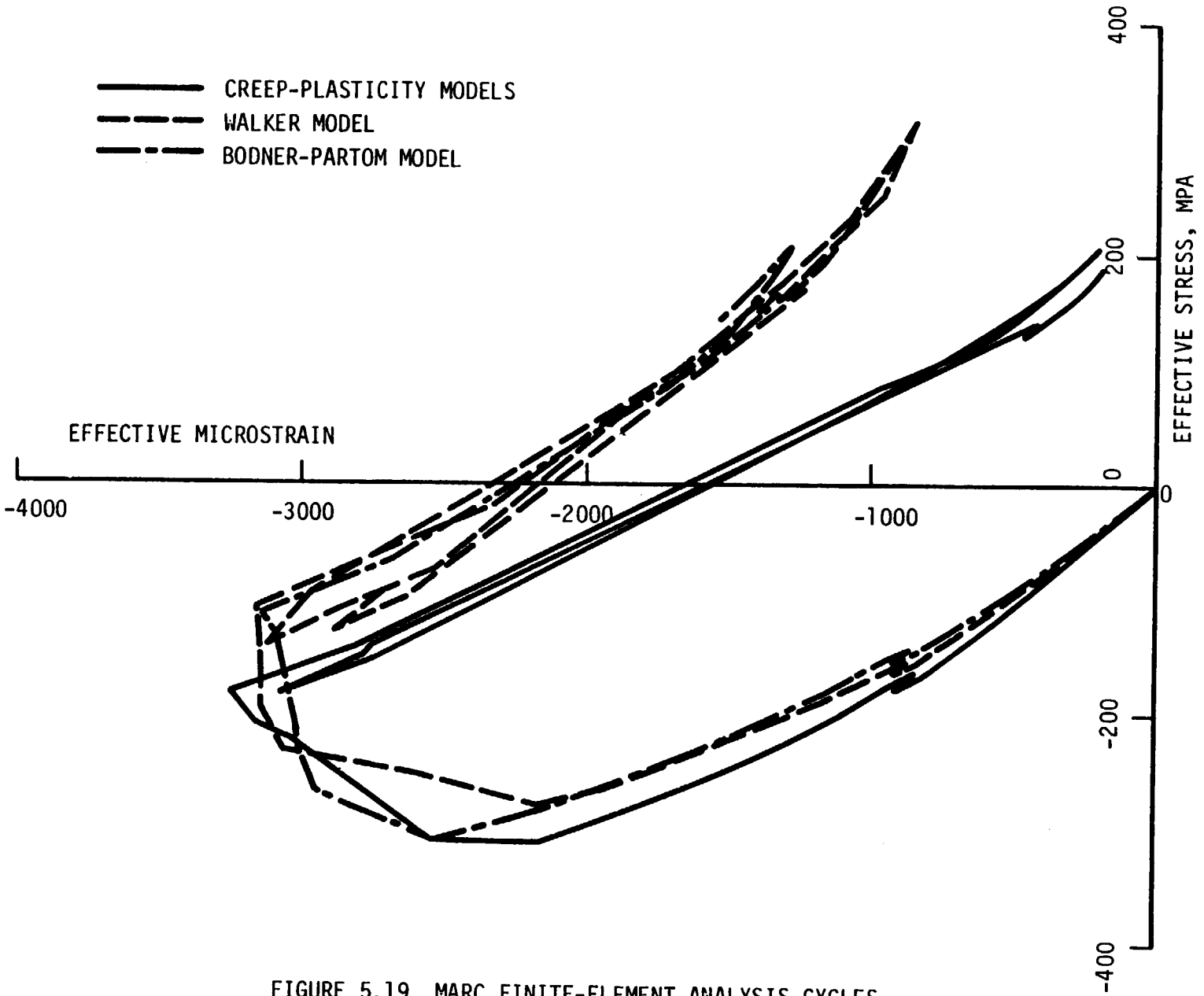

FIGURE 5.19 MARC FINITE-ELEMENT ANALYSIS CYCLES FOR P&W AIRFOIL CRITICAL LOCATION, FROM KAUFMAN ET. AL. [25].

for the effective stress and effective microstrain at the critical location of the PWA airfoil. Note that the Walker and the Bodner-Partom models give comparable results which are, however, substantially different from that obtained based on classical creep-plasticity models. Comparison of the CPU time requirements for these analyses on a Cray computer, shown in Table 5.6, indicates that there is essentially no difference between the CPU time requirement between the unified and the classical approaches. For the airfoil problem examined, the CPU time for the Bodner-Partom model is approximately 35% larger than that for the Walker model, as opposed to a difference 3 times in favor of the Walker model reported previously by PWA. More recent computational work at the NASA Lewis Research Center has eliminated some small numerical difficulties in the use of the Bodner-Partom model for thermomechanical cycling problems. With this modification, the Bodner-Partom model leads to completely smooth response characteristics with improved calculation efficiency. A rerun of the exercise of Figure 5.19 for a single cycle is shown in Figure 5.20. In this example, both unified models were essentially equivalent in CPU time.

5.4 Discussions

Both the Walker and the Bodner-Partom viscoplastic models have been successfully demonstrated in a finite-element analysis of a turbine airfoil under complex and realistic flight cycle loading. Demonstrated using the MARC Code, linear strain, and higher order three dimensional elements, the models were shown to be adaptable for use with regions requiring special structural modeling such as internal cooling features of an airfoil. In addition, the models were found to behave stably through the flight cycle, easily used and efficient. A sensitivity study indicates that large time/temperature/load

TABLE 5.6 TURBINE BLADE STRUCTRUAL ANALYSIS RESULTS OBTAINED BY KAUFMAN ET. AL [25]

ANALYTICAL METHOD	CPU Time sec	Strain Range, Microstrain	Mean Stress MPa	Predicted Cyclic Life*
Elastic	1793	2833	-189	69,100
Elastic-Plastic Creep	3820	3130	116	29,400
Unified (Bodner-Partom)	2458	2900	146	41,500
Unified (Walker)	2800	2850	90	44,800
Simplified (Kaufman)	82	2771	-5	50,700

*Based on effective stress-strain during 2nd cycle.

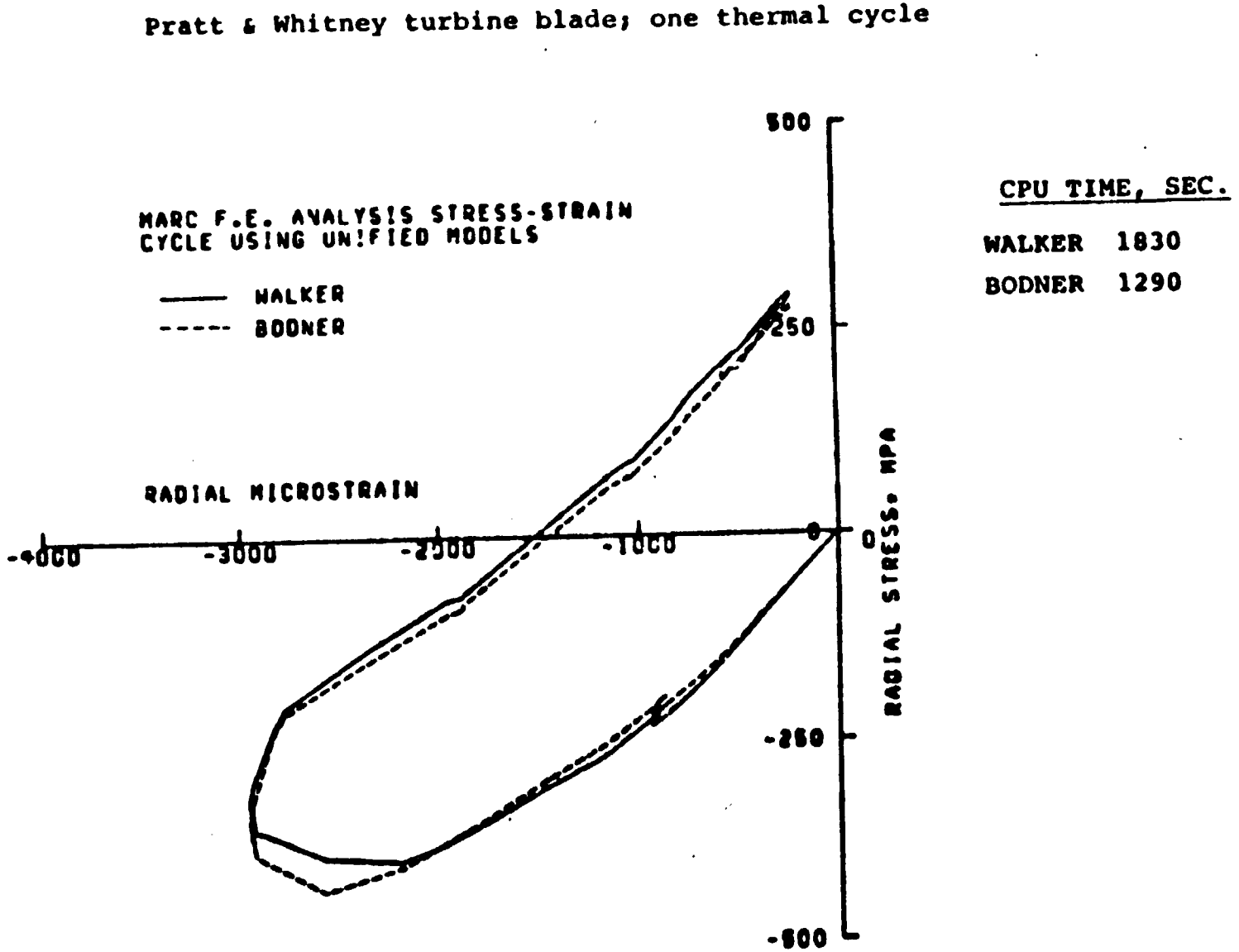

FIGURE 5.20 COMPARISON OF STRESS-STRAIN CYCLES AT THE CRITICAL LOCATION OF THE P&W AIRFOIL. The finite-element analyses were performed using the MARC Code with either the Bodner-Partom or the Walker model. Results are from Kaufman et. al. [25].

steps could be used. Compared to the classical creep-plasticity approach, the unified approach does not incur additional CPU time for the identical problem. Minor differences in the CPU time requirement between the Walker and the Bodner-Partom model occurred, but varied with the problem and programming details. Therefore, a direct comparison of the numerical efficiency of the two unified models is difficult. Most of the variations observed in CPU time was due to differences in programming technique. Whether a self-adaptive scheme is used and the type of problem analyzed also influence the relative CPU time requirement. Based on the airfoil analyses done at NASA Lewis Research Center, it appears that there is little difference in numerical efficiency between the unified models studied. Further, their numerical efficiency is at least equivalent to that obtained using more classical creep-plasticity constitutive models.

It is also interesting to note that the two unified models studied produced nearly equivalent results for a complex time-dependent, non-isothermal, three-dimensional structural problem even though they contain some quite different assumptions in their basic formulations (flow law and treatment of directional hardening, measure of hardening parameter, kinetic relation, etc.).

6.0 SUMMARY OF CURRENT RESULTS

The following tasks were completed during the past year:

- a test procedure was developed for assisting the generation of a data base for the Bodner-Partom model using on a smaller number of specimens;
- a systematic procedure was developed for determining the material constants in the Bodner-Partom model;
- the effects of grain size on the constitutive behavior of B1900+Hf was examined; no grain size effect was observed in the range of casting grain size (.8-2.5 mm) studied;
- a literature survey was conducted to assess the effects of thermal history on the constitutive behavior of metals; thermal history effects are expected to be present at temperature regimes where strain aging and change of microstructure are important;
- the use of a unified constitutive model for hot section component analyses was demonstrated by applying the Walker model and the MARC finite-element code for a B1900+Hf airfoil problem with a complex, realistic flight cycle;
- the efficiency of several numerical integrating schemes for the unified models was evaluated;
- test data including tensile, creep, cyclic and nonproportional tension/torsion loading were collected for the alternate material, Mar-M247; a set of material constants for the Bodner-Partom model were determined and correlations were made between model predictions and experimental results.

7.0 FUTURE WORK

During the second year of the optional program, the following work will be completed:

- Experimental test data will be obtained for B1900+Hf specimens with a ceramic coating. These results will be compared with B1900+Hf specimens without coating to assess the effects of coating on the constitutive behavior of the base material.

- Experimental test data will be obtained for B1900+Hf and Mar-M247 specimens under thermomechanical loading. These experiments will be devised to examine the effects of thermal history on the constitutive behavior of these nickel-base alloys. In particular, the issue concerning whether nonisothermal constitutive behavior can be predicted based on isothermal data will be examined.

- Metallographic evaluation of selected test specimens will be conducted to determine the influence of load and temperature history on the deformation structure of the B1900+Hf alloy. This information will be used to assist possible modification of the Bodner-Partom model to include the effects of microstructure changes.

- Possible modification of the Bodner-Partom model to include effects of strain aging, microstructural changes, and thermal history.

- At least one additional monotonic tensile test will be performed on the B1900+Hf material to assess the value of the strain rate sensitivity parameter obtained in the jump test.

8.0 REFERENCES

1. U. S. Lindholm, K. S. Chan, S. R. Bodner, R. M. Weber, K. P. Walker, and B. N. Cassenti, NASA CR-174718, May 1984.

2. U. S. Lindholm, K. S. Chan, S. R. Bodner, R. M. Weber, K. P. Walker, and B. N. Cassenti, NASA CR-174980, July 1985.

3. S. R. Bodner and Y. Partom, ASME J. of Applied Mechanics, Vol. 42, 1975, p. 385.

4. S. R. Bodner, "Evolution Equations for Anisotropic Hardening and Damage of Elastic-Viscoplastic Materials," Pro. Conference on Plasticity Today, Udine, Italy, 1983.

5. K. P. Walker, NASA Contract Report NASA CR 165533, 1981.

6. K. S. Chan, S. R. Bodner, and U. S. Lindholm, "Modeling to Hardening and Thermal Recovery in Metals", to be published, 1986.

7. G. Cailletaud and J. L. Chaboche, "Macroscopic Description of the Microsctructural Changs Induced by Varying Temperature," ICM3, Vol. 2, 1979.

8. D. N. Robinson, "Thermomechanical Deformation in the Presence of Metallurgical Changes," Prof. Second Symposium on Nonlinear Constitutive Relations for High Temperature Applications, NASA Lewis Research Center, Cleveland, Ohio, NASA Conf. Pub. 2369, Oct. 1984.

9. P. A. Bartolotta, "Thermomechanical Cyclic Hardening Behavior of Hastelloy-X," NASA Contractor Report 174999, 1985.

10. A. Philips, "Combined Stress Experiments in Plasticity and Viscoplasticity: the Effects of Temperature and Time," in Plasticity of Metals at Finite Strain: Theory, Experiment and Computation, E.H. Lee and R.L. Mallett Ed., Stanford University, 1981, p. 230.

11. K. S. Chan, U. S. Lindholm, S. R. Bodner, and K. P. Walker, "A Survey of Unified Constitutive Theories," Prof. Second Symposium on Nonlinear Constitutive Relations for High Temperature Applications, NASA Lewis Research Center, Cleveland, Ohio, NASA Conf. Pub. 2369, Oct. 1984.

12. D. N. Robinson and P. A. Bartolotta, "Viscoplastic Constitutive Relationships with Dependence on Thermomechanical History," NASA Contractor Report 174836, 1985.

13. J. D. Baird, "Dynamic Strain Aging," The Inhomogeneity of Plastic Deformation, ASM, Metals Park, Ohio, 1973, pp. 191-222.

14. C. G. Schmidt and A. K. Miller," The Effects of Solutes on the Strength and Strain Hardening Behavior of Alloys," Acta Metallurgica, Vol. 30, 1982, pp. 615-625.

15. A. Rosen and S. R. Bodner, "The Influence of Strain Rate and Strain Aging on the Flow Stress of Commercially Pure Aluminum," J. of the Mech. and Phys. of Solids, Vol. 15, 1967, pp. 47-62.

16. C. G. Schmidt and A. K. Miller, "A Unified Phenomenological Model for Non-Elastic Deformation of Type 316 Stainless Steel - Part I and Part II," Res. Mechanica, 1981, pp. 109-129, pp. 175-193.

17. A. K. Miller, ASME J. of Eng. Mat. & Tech., Vol. 96, 1976, p. 97.

18. K. P. Walker, "Constitutive Modeling of Engine Materials", Final Report FR-17911, AFML Contract F33615-81-C-5040, November 1983.

19. B. N. Cassenti, "Research and Development Program for Nonlinear Structural Modeling with Advanced Time-Temperature Dependent Constitutive Relationships, Vol. I - Theoretical Discussion", Final Report, NASA CR-168191, July 1983.

20. MARC General Purpose Finite Element Program, MARC Corporation, Palo Alto, Ca.

21. T. G. Tanaka, "A Unified Numerical Method for Integrating Stiff Time-Dependent Constitutive Equations for Elastic/Viscoplastic Deformation of Metals and Alloys," Dissertation, Stanford University, Department of Materials Science and Engineering, 1983.

22. P. K. Imbrie, Private Correspondence, Texas A & M University, September 19, 1985.

23. P. K. Imbrie, W. E. Haisler, D. H. Allen, "Evaluation of the Numerical Stability and Sensitivity to Material Parameter Variations for Several Unified Constitutive Models", Texas A & M University, May, 1985.

24. V. Kumar, M. Morjaria and S. Mukherjee, "Numerical Integration of Some Stiff Constitutive Models of Inelastic Deformation," Transaction of the ASME, Journal of Engineering Materials and Technology, Vol. 102, pp. 92-96, January, 1980.

25. A. Kaufman, J. F. Saltsman, G. R. Halford and M. Tong, "Evaluation of Structural Analysis Methods for Life Prediction," 3rd Symposium on Nonlinear Constitutive Relations for High Temperature Applications, Akron, Ohio, 1986.